Development of a Transportable Cold Atom Gradiometer.

by

Andrew Hinton

A thesis submitted to
The University of Birmingham
for the degree of
DOCTOR OF PHILOSOPHY

Ultracold Atoms Group
School of Physics and Astronomy
College of Engineering and Physical Sciences
The University of Birmingham

November 2016

Abstract

This work describes the technology developed for the transportable gravity gradiometer, "GGtop", constructed at the University of Birmingham. The device aims to simultaneously interrogate two physically separated, free-falling cold atom clouds using the technique of Raman interferometry to perform differential gravity measurements. Such a technique will suppress common-mode noise sources, such as vibrations, that otherwise limit classical gravimeters and cold atom interferometers based on single-cloud measurements. The technique is expected to improve speed and sensitivity for field measurements greatly.

Using a combination of commercially available components and novel designs, intended to enhance portability and robustness, allowed for demonstration of atomic interference with the apparatus via Ramsey's method of separated oscillatory fields. The achieved fringe contrast of $\sim 2\%$, defined as the difference in the number of atoms detected in the $|F = 2\rangle$, was limited by drifts stemming from some of the novel designs which prompted continued optimisation of the underpinning subsystems. To address performance issues parts of the experiment were redesigned with the goal of improving reliability at the expense of some portability. Using the retrofitted experiment, interference was once again achieved with fitted fringe spacing of 134.7 ± 2.0 μs in good agreement with the 133.9 μs defined by the experimental control. A factor of 10 improvement in contrast was found with the central fringe demonstrating 18% of the atoms detected in the $|F = 2\rangle$ state when normalised to the total 3D MOT number. The 3.71 ± 0.01 kHz fitted linewidth of the central fringe gives a frequency uncertainty of $5.43 \pm 0.01 \times 10^{-7}$. This result leaves the experiment in a good position to begin making measurements of gravity.

For my love, Tibby,

and my family.

Thank-you for your support.

ACKNOWLEDGEMENTS

This work was made possible by the incredible effort of several individuals in the atom interferometry team and the GGtop consortium. Our atom interferometry team has exploded in size in recent years and there are too many people for me to thank individually, not forgetting the remainder of the cold atoms group, but you know who you are and thank-you for the help and friendship you have provided over the years.

I am privileged to have worked with Doctors Tristan Valenzuela-Salazar, Michael Holynski and Yu-Hung Lien whose wisdom guided the experiment and who I could always rely on to help me whenever I had a problem. Thank-you to Alexander Niggebaum, Georgios Voulazeris and Lingxiao Zhu who have worked alongside me for construction and testing on a day-to-day basis. The achievements of this project would not have been possible without your contributions. A special thanks to Stephen Brookes and all of the workshop team for the expert manufacturing time they invested in this project. Finally, I am thankful to Professor Kai Bongs for the opportunity to study and be a part of this project.

Praise Helix.

CONTENTS

LIST OF FIGURES

LIST OF TABLES

CHAPTER 1

INTRODUCTION AND MOTIVATION

The work presented in this thesis is built on the pioneering work of Kasevich and Chu [1] almost 25 years ago. Many of the techniques and experimental designs are based around the idea of controlling or using the velocity of an ensemble of atoms by manipulation with light fields. Doing so allows one to study the effects of gravity by dropping atoms as a test mass and measuring how they fall with light acting as a precise ruler. Building a device capable of measuring gravity, or gravity gradients, opens many avenues of interesting research for fundamental science as well as providing a tool to assist with real world problems in underground surveillance.

To begin this thesis I will motivate the study of gravity. I will start with a brief introduction to the topic, detailing the reason for using cold atoms and the logic behind some of the design choices. The story of gravity throughout history will spark interest into study of gravity itself as both a fundamental topic and an applied one. Previous and current mainstream methods for measuring gravity will be discussed in relation to an atom interferometer, drawing conclusions about their limitations. In this, the difference between relative and absolute gravity sensors will be explained. Finally, more motivation for gravity sensing will be presented in the form of applications. At the heart of this experiment exists real-world usability which will be reflected in the designs and discussion of the experiment.

1.1 Foreword

The work presented in this thesis revolves around the gravity sensors developed at the University of Birmingham as part of the UK National Quantum Technology Hub in Sensors and Metrology. The author has personally been involved in the development of two gravity gradiometers, GGtop and the Gravity Imager however this work will focus on the technology developed towards primarily GGtop. The initial design and construction work was a collaborative effort by the Atom Interferometry team which will be presented in chapters 3 & 4. Areas where the author had the most involvement are discussed in chapters 5 - 7.

Gravity sensors based on cold atom technology are currently performing with world-leading sensitivity at several laboratories around the world - [2–4] to mention a few - but the size of the experiments makes them too cumbersome to be used for anything other than fundamental science. Recent advancements on cold atom sensors have been focused on improving the portability of the devices to realise useful sensors [5–9]. It is in this context that the gravity sensors presented here are concerned.

Portable gravity sensors based on classical technology are already used for field applications but they are constrained by mechanical effects. The goal of a cold atom sensor is to use atoms, a perfect test mass, and make use of their identical nature for recording gravitational potentials by dropping these well-controlled microscopic masses instead of macroscopic test masses. Extending this to gravity gradients allows one to obtain a differential measurement of gravity which simultaneously grants a large amount of common-mode noise rejection as well as a higher sensitivity to density changes.

What makes the work done here unique is the application driven approach to developing a gravity gradiometer. From the onset there has been a large collaboration with potential end users to establish requirements and build a working prototype. It became obvious from initial discussions that a normal laboratory experiment would not meet the criteria of a portable sensor and that there is a trade-off between how portable one makes a system and the sensitivity that system can reach. To make useful field measurements of the type shown in Fig. 1.1 it was required that the sensor developed be sensitive at a level of < 10 E [1], ideally 1 E. To realise a portable *and* sensitive sensor it was unavoidable that some new ideas would have to be trialled which could backfire. Examples of these "risky" trade-offs will be discussed briefly in the following and will be reflected in the designs of the experiment which are presented later.

[1] 1 E = 1/1,000,000,000 $1/s^2$

Figure 1.1: Underground mapping applications of a portable gravity sensor. *Image courtesy of the Mapping the Underworld project.*

The most sensitive experiments, like those mentioned above, are where the atoms can be in free-fall for the longest time possible. To realise long free-fall times necessitates vacuum systems of several metres for the atoms to traverse, placing an unavoidable limitation on the size of the experiment. Steps were taken to minimise the height of the experiment by using a launch sequence but this adds complexity to the laser control needed to manipulate the atoms. In laboratory experiments, light is manipulated with tables full of optical components. Whilst these can be made compact they are typically not robust against mechanical/thermal misalignment without special designs [10, 11]. This problem was addressed with a novel fibre-based solution which was known to have potential limitations but had the possibility to aid compactness and robustness greatly. It is the technical challenges in enhancing portability whilst aiming for high sensitivity which make up the majority of this work.

1.2 A History of Gravity

Our story begins in relatively modern history with Newton whose formulation of gravity based on the early work of Galileo, Brahe and Kepler proved once and for all that our Sun was the centre of the solar system and the Earth was in its orbit. He realised that there must exist some force between all objects with mass otherwise they wouldn't accelerate from rest. This force was named gravity.

Fast-forwarding a few hundred years to Eötvös and Newton's laws were starting to be accurately measured by use of the now famous torsion balance [12]. In fact Eötvös' seminal work on measuring gravity gradients is

the historical origin of the unit we now use to describe the change in gravitational acceleration as a function of distance. Around the same time, Einstein was realising that there were certain phenomena that could not be explained by Newtonian gravity and so the theory of general relativity was born in which he cited the work done by Eötvös.

Einstein's description of gravity as a curvature in space rather than a force which acts between two objects has yet to be disproven but the search for a grand unified theory of everything, including gravity, is still one physics' greatest mysteries.

1.3 Current Methods of Measuring Gravity and Comparison with Atom Interferometry

Nowadays there are several state of the art methods for measurement of gravity which can be categorised as relative or absolute sensors.

1.3.1 Relative Gravity Sensors

A relative gravity sensor measures g to some sensitivity with time-dependent accuracy. The measurements are based on the displacement of a mass, nominally supported with some restoring force, where any change from the calibrated zero position is used to infer changes in gravity. They are useful for drift insensitive applications or short term measurements as they tend to have high experimental drift over a period days. The two most commonly used examples of relative gravimeters are based either on superconductivity or spring systems.

- *Spring based gravimeters* measure the capacitance changes when a charged mass on a spring is displaced relative to two charged plates due to gravitational acceleration. These devices are commercially accessible and are relatively compact, portable and easy to operate but are much less sensitive than their rivals. Typical sensitivities achieved by commercial devices are in the region of 10 nms^{-2} [1] [13] over a few minutes of integration time with a repeatability of <50 nms^{-2}. Relative sensors such as these are heavily prone to drift (<20 μms^{-2}/day) and need to be recalibrated with an absolute gravity sensor.

[1] This thesis will use the unit ms^{-2} when referring to gravitational accelerations. Other texts may use the old-fashioned unit of Gal where 1 Gal = 1 $\text{cm}\cdot\text{s}^{-2}$.

- *Superconducting gravimeters* operate by suspending a diamagnetic superconducting sphere in an extremely stable magnetic field. The magnetic field itself is generated by a current source which changes based on the gravitational acceleration. The precise current required to exactly cancel the gravitational acceleration and keep the sphere suspended can be used to deduce its strength. Over short integration times these devices have recorded some of the highest sensitivities to g to date for a relative sensor, in the 10 pms^{-2} range [14], over a minute of integration. The cryogenic operating conditions of these devices reduce drifts typically associated with relative sensors to 400 nms^{-2}/yr. However, such devices are bulky, non-trivial to setup or operate (requiring cryogenics) making them undesirable for a portable system.

1.3.2 Absolute Gravity Sensors

An absolute gravity sensor measures g to some sensitivity with fixed accuracy. The measurements are based on recording how an object falls to measure acceleration due to gravity. Because these sensors are an absolute gauge of gravity they are immune to drifts and hence useful for applications that require zero/low drift. One example of a sensor is the commercial falling-mirror system based on the Michelson interferometer experiment [15] which can achieve accuracies of 20 nms^{-2}. Such systems are prone to mechanical vibration and wear making them impractical for portable sensors or for long term operation. These systems suffer heavily from a low repetition rate, limited by the time it takes to reset the cube in the chamber and for ground vibrations to dissipate. For a portable sensor mapping in real time this means the device is transparent to higher frequency signals.

1.3.3 Cold Atoms as Inertial Test Masses

The most accurate gravity sensors using classical methods are based in space where free-fall times are long and vibrations are low. The GOCE satellite which recently mapped the geoid of the Earth used six accelerometers in an orthogonal arrangement with its most accurate axis measuring ~ 10 pms^{-2} [16].

The best laboratory gravity sensors based on cold atoms achieve accuracies of 67 pms^{-2} [17], already competing with space-based classical systems. The key benefit offered by atom interferometers is that a cloud of atoms behaves like a point mass under freefall which has well understood and reproducible properties. One is essentially dropping a cloud of atoms into a laser beam and making use of Doppler theory to measure their acceleration. This, in conjunction with the scalability of the devices, means they will supersede their classical brethren. It is expected that atom interferometer accuracy will improve three orders of magnitude in space

	Gravity (g_z)	**Gravity gradient** (g_{zz})
Signal	$\frac{GMz}{(r^2+z^2)^{3/2}} \times 10^5$	$\frac{GM(r^2-2z^2)}{(r^2+z^2)^{5/2}} \times 10^9$
Peak signal (r=0)	$\frac{GM}{z^2} \times 10^5$	$\frac{2GM}{z^3} \times 10^9$
FWHM	$1.53z$	$\approx z$

Table 1.1: Comparison of gravity and gravity gradient signals. In this example: G is the gravitational constant, M is the mass of the object, r is the displacement from the gravitational mass in a plane perpendicular to the depth and z is the depth of the mass. FWHM fitted from Fig. 1.2

due to the extended free-fall time [18].

For field applications cold atoms sensors present benefits. Two commonly used classical devices are the absolute Micro-g LaCoste FG-5 sensor and the relative Scintrex CG-5 sensor. They provide complementary measurements to cover the weaknesses of the partner device; mainly the FG-5 is used as an absolute measure to calibrate the CG-5 while the CG-5 is used for long term measurement to minimise the mechanical wear on the FG-5. A sensor based on cold atom technology allows for a single device with long term operation and absolute sensitivity.

1.3.4 Gravity Gradients

Precise measurements of gravity are an interesting endeavour from the aspects of fundamental science and practical applications but they suffer from a major limitation in field conditions that can be more easily compensated in a laboratory. That limitation is Eintein's equivalence principle which states that gravitational and inertial acceleration are indistinguishable. This means that any vibration of the apparatus couples noise into the measurement and so sophisticated vibration cancellation systems are typically needed such as those developed in [8]. This added complexity and cost is undesirable for the portable system being developed in this report.

Presented here is a transportable gravity gradiometer where two atomic clouds are simultaneously interrogated such that vibration noise is common mode and rejected. Gravity gradient sensing has an additional benefit in that it is a differential measurement; making it more sensitive to changes in g due to density differences. A gravity gradiometer measures the spatial derivative of g. The spectral power density of the signal is therefore higher frequency and more localised to the source than a gravity signal. A comparison of gravity and gravity gradient signals for a 10 kg, point-source, object at a depth of 1 m (simulating an underground utility pipe) is shown in Tab. 1.1 and Fig 1.2.

One can see from the FWHM that the gradient signal is more localised to the source allowing for better

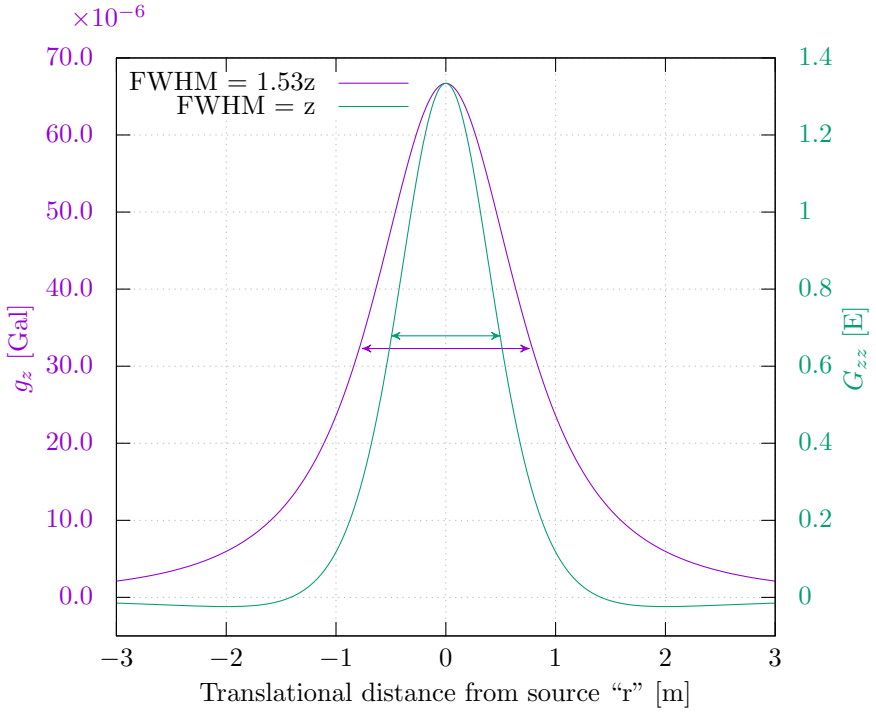

Figure 1.2: Comparison of gravity (purple) and gravity gradient (green) signals for a 10 kg object at a depth of 1 m from a topological scan in a perpendicular plane. (1 E = 1/1,000,000,000 $1/s^2$).

estimation of the position of the object. If the signal in Fig. 1.2 represents a typical application for our gradiometer then the theoretical signal response highlights the need for a 1 E sensor. It is also possible to conclude from this plot that a $\sim 7 \times 10^{-7}$ ms^{-2} (70×10^{-6} Gal) gravimeter would perform a similar task. Portable gravimeters at this resolution have been realised [9] but due to vibration noise mentioned above they must be averaged for long time periods before they can reach this performance. In this example the authors reached a resolution of 1.1×10^{-7} ms^{-2} after 200 s of averaging. A gradiometer therefore accelerates the data capturing process by removing the need to average over the vibration noise spectrum. This is obviously desirable for field measurements where one cannot afford to spend 200 s averaging data like in [9]. The gain in speed means that even if the gradiometer developed here fails to meet the sensitivity requirements by an order of magnitude it will still be useful for fast surveys of larger objects.

Recent proposals for an airborne superconducting gravity gradiometer (SGG) have sparked a great interest in the survey community. The authors of [19] claim they can reach a sensitivity of 1 E/$\sqrt{\text{Hz}}$, the same sensitivity as aimed for by this experiment but in a complicated airborne environment. This is an improvement over the current generation of portable atomic gravity gradiometers which reach a sensitivity of 7.2 E/$\sqrt{\text{Hz}}$ [20]. This accuracy is in large due to low temperatures offering a low noise and mechanically stable environment

Figure 1.3: Large sinkhole formed in residential area due to underground soil erosion. *Image courtesy of Hertfordshire Fire and Rescue Service 2015.*

in addition to technique of superconductivity for measurement being greatly insensitive to linear and angular accelerations applied to the instrument. The apparatus, requiring cryogenics and a rigid mounting platform, is unsuitable for portable use in confined spaces as a large vehicle is needed for transport.

1.4 Applications of Gravity Sensing

Gravity sensing as a field is well established and there are interesting applications for both fundamental science and real world geodesy.

In fundamental research, atom inteferometers are poised to start probing the weak equivalence principle (WEP) [21–23] and potential experiments for the detection of gravitational waves have been proposed [24–27] with increasing traction from the success of LIGO [28]. Physical quantities such as the Gravitational constant [29] and fine structure constant [30] are able to be measured with ever increasing precision. Sensors for studying rotation based on the Sagnac effect [31] or Coriolis effect [32] have been realised.

Experiments such as those listed above are aiming towards sensitivities far greater than those aimed at here. The distinction for this experiment is that some absolute sensitivity will be sacrificed in order to make a *useful* device. That is to say, a working prototype that can be used for field applications. We estimate that a sensitivity to gravity gradients of 1 E is sufficient for real world applications i.e. detecting something ~ 10 cm diameter at a depth of ~ 1 m which is reflected by the rough model in Fig. 1.2. Such a sensitivity would allow for mapping of underground pipework (Fig. 1.1) or large underground voids caused by soil erosion like those seen recently in England Fig. 1.3.

1.5 Thesis Overview

This work will start with a theoretical introduction to Raman atom interferometry to give a sufficient understanding on how an atom interferometer works which will give an insight to some design choices. The remainder of the thesis is broken down into two parts. In the first part (chapters 3 - 5) I will describe the work done on the experiment "GGtop" including the experimental assembly and preliminary results. The information presented in these chapters highlighted the limitations of the system and motivated the work done in part two (chapters 6 - 7). In these chapters I will talk about the development of certain technologies aimed at improving the portability and reliability of the experiment and future portable sensors. Finally I will close with some thoughts on the success of the project as a whole and some of the future goals.

CHAPTER 2

RAMAN ATOM INTERFEROMETRY

This chapter outlines the theory necessary to facilitate a proper understanding of an Atom Interferometer (AI). A detailed description of laser cooling is not included as it is covered extensively in other texts [33, 34]. Firstly, the matter-wave relation between light and atoms will be used to demonstrate the similarities between a traditional Mach-Zehnder interferometer and an AI. With this idea in mind, a more thorough examination of AIs will be had. The starting point for this will be the simple example of a two-level atom in a light field in order to first understand single photon transitions and Rabi oscillations. Using this two level approximation it is straightforward to move to a multi-level system with Raman transitions and explain the reasoning behind the choice of atomic species. The chapter will conclude with a summary of the potential phase contributions encountered by such an interferometer. Understanding where these phase contributions come from and their relative magnitudes is important when designing the experiment as some will need to be compensated to obtain a meaningful instrument sensitivity.

2.1 Realising a Mach-Zehnder Interferometer

There are several examples of optical interferometers that rely on similar operating principles. In these interferometers, a coherent light beam is split into two separate beams that travel through different optical paths before being recombined. The interference pattern observed after recombination is indicative of any phase shifts encountered by the two beams. To split and recombine light beams, macroscopic optical components such as beam splitters and mirrors are used in various combinations. The most analogous combination to this work is the Mach-Zehnder [35] arrangement which will be discussed in this section.

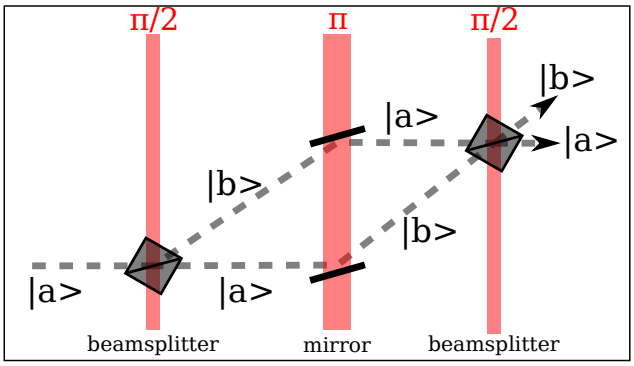

Figure 2.1: Typical interferometer scheme. A Mach-Zehnder interferometer for light made up of physical beam splitters and mirrors. Incident light is split and sent along two different paths before being recombined and the interference effect studied. In an atom interferometer light beams act as the beam splitters and mirrors for atomic energy states. An incident wavepacket prepared in some hyperfine state is separated via the superposition principle, sent along physically different paths before being recombined and interference examined.

A typical Mach-Zehnder interferometer is shown in Fig. 2.1. Light incident on a beamsplitter is separated and travels along two independent paths where it is reflected by a mirror before being recombined at a second beamsplitter and an interference pattern is observed. Providing the two optical paths are identical no phase shift will be observed. A phase shift, $\Delta\phi$, is introduced if the path length of one arm of the interferometer is modified in some way.

One can create the same effect by swapping the roles of matter and waves due to the wave-particle duality of light. Consider a two-level atom with energy levels $|a\rangle$ and $|b\rangle$ travelling in some direction in space and initially in eigenstate $|a\rangle$. If one applies a light pulse that couples these two energy levels such that there is a 50% probability of being in either state then the atomic wavefunction will be split into two parts with equal amplitudes. Part of the wavefunction will continue to travel in the initial direction whilst the other part will be given a momentum kick of $\hbar k$ along a different trajectory, causing the wavefunctions to separate. At some time later, application of a light pulse that transfers the wavefunction to the other state with 100% probability will cause an inversion of momenta. The wavepackets will hence start to converge. At the point

at which the two wavefunctions overlap spatially a final pulse is applied to recouple. The significance of $\pi/2$ and π pulses, used for splitting and reflection respectively, will be addressed in the following section. Assuming the paths are identical and there are no phase shifts, the final wavefunction will be in state $|a\rangle$. Phase shifts during the evolution in this scenario are highlighted by a population distibution after the final light pulse.

AIs offer several advantages over their light counterparts, the foremost being that atoms are being used to probe perturbations rather than photons and atoms are inherently more sensitive to environmental effects such as electric and magnetic fields. Of key importance for the field of atom interferometry, atoms have mass and so unlike photons can be used to directly measure perturbations in the gravitational field.

2.2 A two-level atom in a light field

In order to realise an interferometer a certain sequence of splitting and recombining wavepackets is required as highlighted in the previous section. For an AI, splitting or recombining a wavepacket is controlled by the Rabi frequency [36, 37]. This section will derive the conditions necessary for $\pi/2$ and π pulses following the work outlined in [1, 38].

Taking the two levels $|a\rangle$ and $|b\rangle$ from Fig. 2.1 one can write down the corresponding energy eigenvalues $\hbar\omega_a$ and $\hbar\omega_b$. Assume now that the two-level system interacts with a monochromatic light field of frequency ω_L such that the electric field (assuming a constant amplitude) is defined as:

$$\mathbf{E_L}(\mathbf{r}, t) = \mathbf{E_0} \cos[\mathbf{k_L} \cdot \mathbf{r} - \omega_L t + \phi_L] \tag{2.1}$$

where $\mathbf{r} = (x, y, z)$ and $\mathbf{k_L}$ are the atomic position and and light field vectors.

Using the dipole approximation [39], one can write the Hamiltonian for such a system as follows:

$$\mathcal{H} = \frac{\mathbf{p}^2}{2m} + \hbar\omega_a |a\rangle \langle a| + \hbar\omega_b |b\rangle \langle b| - \mathbf{d} \cdot \mathbf{E_L} \tag{2.2}$$

where $\mathbf{d}$ is the electric dipole moment operator. It has been assumed that for this Hamiltonian the energy eigenstates $|a\rangle$ and $|b\rangle$ are quantised and that the momenta are continuous.

One must now describe the time evolution of such a system by introducing two eigenstates corresponding to the energy of the atom initially in state $|a\rangle$ and the energy of the atom in state $|b\rangle$ following the absorption of a photon. During absorption or stimulated emission of the photon, it can be shown that the atomic

momentum changes by the momentum of the absorbed photon $\pm\hbar\mathbf{k_L}$. Hence one can write the two new eigenstates:

$$\begin{aligned} |1\rangle &= |a, \mathbf{p}\rangle & E_1 &= \hbar\omega_a + \frac{|\mathbf{p}|^2}{2m} = \hbar\omega_1 \\ |2\rangle &= |b, \mathbf{p} + \hbar\mathbf{k_L}\rangle & E_2 &= \hbar\omega_b + \frac{|\mathbf{p} + \hbar\mathbf{k_L}|^2}{2m} = \hbar\omega_2 \end{aligned} \tag{2.3}$$

where $\mathbf{p}$ is the original atomic momentum and $\mathbf{p}+\hbar\mathbf{k_L}$ is the original momentum plus the photon momentum. The new Hamiltonian for the system can be written as:

$$\mathcal{H} = \hbar\omega_1 |1\rangle \langle 1| + \hbar\omega_2 |2\rangle \langle 2| - \mathbf{d} \cdot \mathbf{E_L} \tag{2.4}$$

It will be useful later on to express ω_1 and ω_2 as a relative frequency, ω_0 such that:

$$\omega_0 = \omega_2 - \omega_1 = \omega_{ab} + \frac{\mathbf{p} \cdot \mathbf{k_L}}{m} + \frac{\hbar |\mathbf{k_L}|^2}{2m} \tag{2.5}$$

where one has $\omega_{ab} = \omega_b - \omega_a$, a Doppler term and a recoil term. With this one can write an expression for the Doppler shift:

$$\delta = \omega_L - \omega_0 = \omega_L - \left(\omega_{ab} + \frac{\mathbf{p} \cdot \mathbf{k_L}}{m} + \frac{\hbar |\mathbf{k_L}|^2}{2m} \right) \tag{2.6}$$

Returning to the discussion of the time evolution of the eigenstates, recall that any quantum state evolves according to the time dependent Schrödinger equation:

$$\mathcal{H} |\Psi(t)\rangle = i\hbar \frac{d}{dt} |\Psi(t)\rangle \tag{2.7}$$

Using the two eigenstates defined previously one arrives at an equation for the time evolution for the system which is a linear superposition of the two eigenstates:

$$|\Psi(t)\rangle = a_1(t) |1\rangle + a_2(t) |2\rangle \tag{2.8}$$

with a_1 and a_2 being the probability amplitudes of detecting the atom in that state at time t. From Eq. 2.7, rewrite the probability amplitudes as:

$$a_1(t) = c_1(t) e^{-i\omega_1 t} \quad a_2(t) = c_2(t) e^{-i\omega_2 t} \tag{2.9}$$

and hence the time evolution of the atomic wavefunction becomes:

$$|\Psi(t)\rangle = c_1(t)e^{-i\omega_1 t} + c_2(t)e^{-i\omega_2 t} \tag{2.10}$$

At this point one can employ the rotating wave approximation, in which rapidly oscillating terms are neglected, [40, 41] to obtain differential equations for the coefficients $c_i(t)$:

$$i\dot{c}_1(t) = \frac{\Omega}{2}e^{i\delta t}e^{-i\phi_L}c_2(t) \tag{2.11}$$

$$i\dot{c}_2(t) = \frac{\Omega^*}{2}e^{-i\delta t}e^{-i\phi_L}c_1(t) \tag{2.12}$$

In the approximation, a coefficient Ω is introduced which will hence be referred to as the Rabi frequency and can be defined as:

$$\Omega = -\frac{\langle a|\,\mathbf{d}\cdot\mathbf{E_0}\,|b\rangle}{\hbar} \tag{2.13}$$

There is a slight caveat here as this definition is strictly only valid when the Rabi frequency is resonant between the two energy levels. When detuned from resonance, the Rabi frequency is adjusted:

$$\Omega' = \sqrt{\Omega^2 + \delta^2} \tag{2.14}$$

From this one can write exact solutions for the c_i coefficients:

$$c_1(t) = e^{i\frac{\delta}{2}t}\left[c_1(0)\left[\cos\left(\frac{\Omega' t}{2}\right) - i\frac{\delta}{\Omega'}\sin\left(\frac{\Omega' t}{2}\right)\right] + c_2(0)e^{-i\phi_L}\left[-i\frac{\Omega}{\Omega'}\sin\left(\frac{\Omega' t}{2}\right)\right]\right] \tag{2.15a}$$

$$c_2(t) = e^{-i\frac{\delta}{2}t}\left[c_1(0)e^{i\phi_L}\left[-i\frac{\Omega}{\Omega'}\sin\left(\frac{\Omega' t}{2}\right)\right] + c_2(0)\left[\cos\left(\frac{\Omega' t}{2}\right) + i\frac{\delta}{\Omega'}\sin\left(\frac{\Omega' t}{2}\right)\right]\right] \tag{2.15b}$$

The key result here is that the probability of finding the atom in either of the atomic states as a function of interaction time with the light field oscillates periodically at frequency Ω'. If the frequency is on resonance (i.e. $\delta = 0$) then the previous equations simplify and $\Omega' = \Omega$. The probability of finding the atom in either state $|1\rangle$ or $|2\rangle$ is then:

$$P_1(\tau) = \frac{1+\cos\Omega\tau}{2} \quad P_2(\tau) = \frac{1-\cos\Omega\tau}{2} \tag{2.16}$$

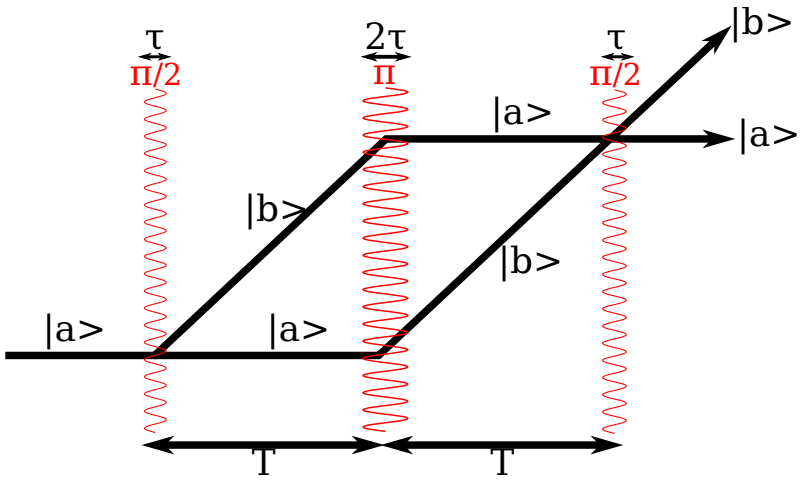

Figure 2.2: Kasevich-Chu interferometer scheme. The first $\pi/2$ pulse at point p acts a beamsplitter putting the wavepacket in an equal superposition of the two hyperfine states. The hyperfine state $|b\rangle$ absorbs the photon momentum and physically separates from state $|a\rangle$. The second π pulse at q/r acts as a mirror, exchanging the momentum states of the wavepackets. The final $\pi/2$ pulse at s causes the wavepackets to interfere.

where τ is the interaction time and is was assumed that the atom started in state $|1\rangle$. In such a regime, the wavefunction describing the evolution of the wavepacket becomes:

$$|\psi(\tau)\rangle = \cos\left(\frac{\Omega\tau}{2}\right)|1\rangle + e^{-i\frac{\pi}{2}}e^{i\phi_L}\sin\left(\frac{\Omega\tau}{2}\right)|2\rangle \tag{2.17}$$

Eq. 2.16 allows one to explain the origin of the terms $\pi/2$ and π pulse which are instrumental to the interferometer scheme employed in this work. When $\tau = \pi/\Omega$ then $P_1 = 0$ and $P_2 = 1$ i.e. all of the atoms initially in state $|1\rangle$ have been transferred to state $|2\rangle$. This is known as a π pulse because $\tau \propto \pi$. When $\tau = \pi/2\Omega$ then $P_1 = 1/2$ and $P_2 = 1/2$ for which we can say the atom is in a linear superposition of states $|1\rangle$ and $|2\rangle$ and has an equal probability of being in either. For this reason it is given the name $\pi/2$ pulse. The two types of pulse derived above are crucial building blocks required to understand an AI. Shown in Fig. 2.2 is the type of scheme employed in this experiment as used in many other experiments [38, 42, 43]. One can clearly see the similarity to a Mach-Zehnder interferometer.

For this example, the atomic wavefunction is initially in state $|1\rangle$. At time $t = 0$, a $\pi/2$ pulse is applied to the wavefunction which couples the two states and creates two wavefunctions which evolve independently along different paths; $|1\rangle = |g_1, \vec{p}\rangle$ and $|2\rangle = \left|g_2, \vec{p} + \hbar\vec{k}_{\text{eff}}\right\rangle$, where $|g_1\rangle$ and $|g_2\rangle$ are the hyperfine ground states, $\vec{p}$ is the atom's momentum and $\vec{k}_{\text{eff}}$ is the effective wavevector of the light. After some free evolution time T, a π pulse is applied. The effect of this pulse is to invert the current states and momentum of the wavefunctions. After another time T, the final $\pi/2$ pulse of this sequence is applied. Once again this couples

the two states and they recombine causing interference. The evolution time T is an important factor in determining the accuracy of such an interferometer sequence as a measurement of gravity scales with T^2 which will be discussed in a later section.

Up until now the discussion has been focussed on using a two-level atom with a single photon transition but in reality this is just an approximation. In a real system this two-level example won't always hold true as atomic spectra are made more complex by fine and hyperfine structure. For the approximation to hold true, one requires that the excited state has a longer lifetime than the time it takes for the interferometry sequence to complete so that spontaneous emission of photons can be mitigated and one can treat the system as if it only has two levels. For this reason a dipole forbidden transition between two hyperfine levels of an atomic groundstate is chosen.

^{87}Rb is the chosen atomic source for this experiment and has a hyperfine groundstate splitting of 6.8 GHz. This source is a common choice in most cold atom labs due to the convenient energy splitting between the groundstate and first excited state of approximately 780 nm, a commonly used wavelength in many consumer products making it easy to obtain good quality lasers. The hyperfine splitting of the groundstate falls in the microwave range so theoretically one could use microwaves to drive the transitions much like in atomic-fountain clocks [44]. The major difference between the clock and interferometer experiments is that in an interferometer it is desirable to have a large momentum transfer to physically separate the two wavepackets such that they truly experience different local perturbations. The momentum transfer from microwaves is insufficient to satisfy this criterion but this is not true of the photon momentum transfer from light. However, given that the hyperfine ground state splitting of ^{87}Rb is 6.8 GHz and that optical frequencies are in the THz region one can see that it is impossible to drive a transition between the ground states with a single photon. Instead a 2-photon transition with counter-propagating light beams whose frequency difference is equal to that of the hyperfine splitting of the ground state is used. This type of interaction has an additional benefit of double optical momentum transfer and will henceforth be referred to as a Raman transition. The mathematics for such a transition share many similarities with the previously discussed two level approximation.

2.3 Multi-level atoms and two-photon Raman transitions

Two laser beams with frequencies ω_{R1} and ω_{R2} will drive a coherent Raman transition between levels $|1\rangle$ and $|2\rangle$ if the atom is stationary with respect to both beams when:

$$\hbar(\omega_{R1} - \omega_{R2}) = \mathbf{E_2} - \mathbf{E_1} \tag{2.18}$$

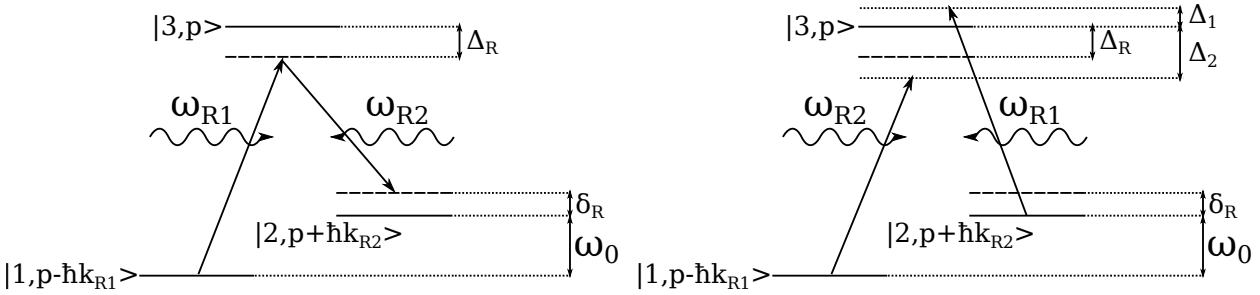

Figure 2.3: Two-photon Raman transition coupling the two hyperfine ground states $|1\rangle$ and $|2\rangle$ with a small, variable detuning δ_R. The detuning, Δ_R is the absolute detuning from a normal transition to the excited level. The two figures illustrate that there are four possible absorptions (neglecting hyperfine splitting) that can take place and this has an effect on the Rabi frequency of the system.

as illustrated by Fig. 2.3. For a large enough detuning, Δ_R, from the intermediate state, $|3\rangle$, single photon excitation becomes negligible and one can assume no population is transferred to the intermediate state. In this case, the two light fields, E_1 and E_2, are counterpropagating and their time evolution can be written as:

$$\begin{aligned} \mathbf{E_{R1}}(x,t) &= \mathbf{E_{R1,0}}\cos[\mathbf{k_{R1}}\cdot x - \omega_{R1}t + \phi_{R1}] \\ \mathbf{E_{R2}}(x,t) &= \mathbf{E_{R2,0}}\cos[\mathbf{k_{R2}}\cdot x - \omega_{R2}t + \phi_{R2}] \end{aligned} \tag{2.19}$$

The absorption of a photon from $\mathbf{E_{R1}}$ with wavevector $\mathbf{k_{R1}}$ and stimulated emission of a photon in the opposite direction caused by $\mathbf{E_{R2}}$ with wavevector $\mathbf{k_{R2}}$ ($\mathbf{k_{R1}} \approx \mathbf{k_{R2}}$) gives the atom two momentum recoil kicks and the states $|1\rangle$ and $|2\rangle$ are coupled.

For a truthful analysis of the Raman transition one must take into account that there are four transitions that can take place due to the Doppler shift induced by the velocity of the atoms. The first two of these transitions are similar and correspond to if an atom in $|1\rangle$ absorbs a photon from $\mathbf{E_{R1}}$ or if an atom in $|2\rangle$ absorbs a photon from $\mathbf{E_{R2}}$. The other two transitions are related to the Doppler shift which allows an atom in $|1\rangle$ to absorb a photon from $\mathbf{E_{R2}}$ and vice versa.

The derivation for a two-photon Raman transition follows very closely that outlined in the previous section; the specific case of a velocity selective transition will be discussed here following the work of [45].

Consider the time evolution of the system shown in Fig. 2.3. The wavefunction can be written as:

$$|\Psi_p(t)\rangle = c_1(p,t)\,|1, p-\hbar k_{R1}\rangle + c_2(p,t)\,|2, p+\hbar k_{R2}\rangle + c_3(p,t)\,|3,p\rangle \tag{2.20}$$

One can define a Hamiltonian for this system of the form $H = H_A + H_{int}$ where the atomic Hamiltonian is:

$$H_A = \frac{p^2}{2M} + \hbar\omega_{31} |3\rangle \langle 3| + \hbar\omega_{21} |2\rangle \langle 2| \tag{2.21}$$

and the interaction Hamiltonian is:

$$H_{int} = -\mathbf{d} \cdot \mathbf{E}(x,t) \tag{2.22}$$

Here $\mathbf{d}$ is the electric dipole operator and $\mathbf{E}(x,t)$ is the total field from the counterpropagating electric fields in Eq. 2.19.

Defining the Rabi frequencies

$$\Omega_n = -\frac{\langle n| \mathbf{d} \cdot \mathbf{E} |3\rangle}{2\hbar}, \quad n = 1, 2 \tag{2.23}$$

allows one to write the Hamiltonian as:

$$H = \begin{pmatrix} \frac{(p-\hbar k_{R1})^2}{2M} & 0 & \hbar\Omega_1 e^{i\omega_{R1}t} \\ 0 & \frac{(p+\hbar k_{R2})^2}{2M} + \hbar\omega_{21} & \hbar\Omega_2 e^{i\omega_{R2}t} \\ \hbar\Omega_1^* e^{-i\omega_{R1}t} & \hbar\Omega_2^* e^{-i\omega_{R2}t} & \frac{p^2}{2M} + \hbar\omega_{31} \end{pmatrix} \tag{2.24}$$

From the Hamiltonian the quantity B_i can be defined:

$$B_1(p,t) = c_1(p,t)\exp\left[i\frac{(p-\hbar k_{R1})^2}{2M\hbar}t\right] \tag{2.25a}$$

$$B_2(p,t) = c_2(p,t)\exp\left[i\left[\frac{(p+\hbar k_{R2})^2}{2M\hbar} + \omega_{21}\right]t\right] \tag{2.25b}$$

$$B_3(p,t) = c_3(p,t)\exp\left[i\left[\frac{p^2}{2M\hbar} + \omega_{31}\right]t\right] \tag{2.25c}$$

which lead to the rate equations:

$$\frac{dB_1}{dt} = -i\Omega_1 e^{-i\Delta_R t} B_3 \tag{2.26a}$$

$$\frac{dB_2}{dt} = -i\Omega_2 e^{-i(\Delta_R+\delta_R)t} B_3 \tag{2.26b}$$

$$\frac{dB_3}{dt} = -i\Omega_1^* e^{i\Delta_R t} B_1 - i\Omega_2^* e^{i(\Delta_R+\delta_R)t} B_2 \tag{2.26c}$$

Making the assumption that $\Delta_R \gg \Omega_1, \Omega_2, \delta_R$ allows these three rate equations to be reduced to just two, mimicking the two-level atom picture. The effective rate equations are:

$$\frac{dB_1}{dt} = i\frac{|\Omega_1|^2}{\Delta_R}B_1 + i\frac{\Omega_1\Omega_2^*}{\Delta_R}B_2 e^{i\delta_R t} \tag{2.27a}$$

$$\frac{dB_2}{dt} = i\frac{\Omega_1^*\Omega_2}{\Delta_R}B_1 e^{-i\delta_R t} + i\frac{|\Omega_2|^2}{\Delta_R}B_2 \tag{2.27b}$$

The key difference here is that the system involves two photons and one can introduce the effective quantities to highlight the similarity with the equations from the previous section:

$$\begin{aligned}
&\omega_{\text{eff}} = \omega_{R1} - \omega_{R2} \\
&\mathbf{k}_{\text{eff}} = \mathbf{k_{R1}} - \mathbf{k_{R2}} = \frac{\mathbf{k_{R1}}}{|\mathbf{k_{R1}}|}(|\mathbf{k_{R1}}| + |\mathbf{k_{R2}}|) \\
&\phi_{\text{eff}} = \phi_{R1} - \phi_{R2} \\
&\Omega_{\text{eff}} = \frac{\Omega_1\Omega_2}{2\Delta_R} \\
&\Omega_{\text{eff}}^{'} = \sqrt{\Omega_{\text{eff}}^2 + (\delta_R - \delta^{AC})^2}
\end{aligned} \tag{2.28}$$

where the quantity δ^{AC} has been introduced to describe the ac Stark shift induced by the atom-light interaction. This can be experimentally made equal to zero with careful intensity balancing of the two electric fields. In our experiment, the Raman light frequencies for the counter-propagating two-photon transition are generated by phase-modulating the light to generate frequency sidebands and then retroreflecting the light from a controllable mirror. Interference between these multiple frequencies complicates the effective Rabi frequency, Ω_{eff}, as there are several resonant possibilities depending on the atom Doppler velocity along with adverse contributions from Doppler insensitive processes and standing wave diffraction [46].

The idea of multiple frequencies being resonant was mentioned earlier in this section so here it will just be stated that the Doppler shift, $2kv$, must be greater than the Rabi frequency so that only one combination of ω_1 and ω_2 drives the transition. When this condition is satisfied the Doppler insensitive and standing wave diffraction processes become negligible.

The way we generate frequency sidebands we can assume we're in a weak modulation regime such that there are three main frequency components: $\omega - \omega_m$, ω, and $\omega + \omega_m$ where ω_m is the modulation frequency. The Raman transition can be driven by both combinations of ω and one of the other frequency components and these two driving fields will interfere. The effective Rabi frequency is hence [1]:

$$\Omega_{\text{eff}} = \frac{\Omega_+^*\Omega_c}{2\Delta_+}e^{k_m l} + \frac{\Omega_c^*\Omega_-}{2\Delta_c}e^{-k_m l} \tag{2.29}$$

where l is the distance between the atoms and the retroreflection mirror, $\Omega_\pm$ and Ω_c are the sideband and

Internal State	Momentum Change	Phase Change
$\|a\rangle \to \|a\rangle$	$\|\mathbf{p}\rangle \to \|\mathbf{p}\rangle$	$\phi^{\rm ac}_{\rm avg} - \frac{1}{2}\phi^{ac}_{\rm diff}$
$\|a\rangle \to \|b\rangle$	$\|\mathbf{p}\rangle \to \|\mathbf{p} + \hbar\mathbf{k}_{\rm eff}\rangle$	$\phi^{\rm ac}_{\rm avg} + (\mathbf{k}_{\rm eff} z_i - \omega_{\rm eff} t_i - \phi_{\rm eff}) + \pi/2$
$\|b\rangle \to \|a\rangle$	$\|\mathbf{p} + \hbar\mathbf{k}_{\rm eff}\rangle \to \|\mathbf{p}\rangle$	$\phi^{\rm ac}_{\rm avg} - (\mathbf{k}_{\rm eff} z_i - \omega_{\rm eff} t_i - \phi_{\rm eff}) + \pi/2$
$\|b\rangle \to \|b\rangle$	$\|\mathbf{p} + \hbar\mathbf{k}_{\rm eff}\rangle \to \|\mathbf{p} + \hbar\mathbf{k}_{\rm eff}\rangle$	$\phi^{\rm ac}_{\rm avg} + \frac{1}{2}\phi^{\rm ac}_{\rm diff}$

Table 2.1: Momenta and phase changes of atoms in Raman pulse [2]. The effective quantities are those described in Eq. 2.28 at space-time point (z_i, t_i). The phase factors $\phi^{\rm ac}_{\rm avg}$ and $\phi^{\rm ac}_{\rm diff}$ arise from ac Stark shifts [47].

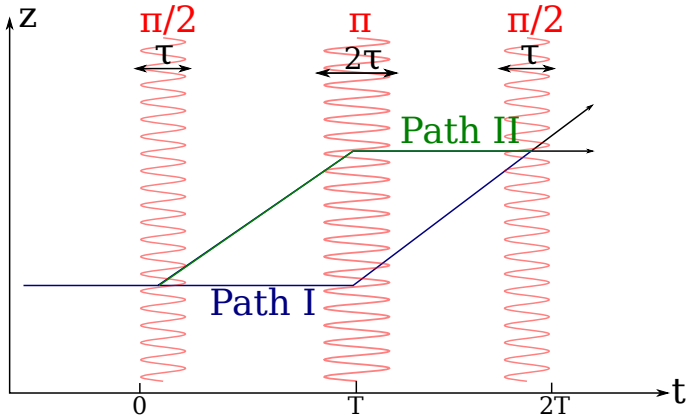

Figure 2.4: Pulse sequence used for a Mach-Zehnder-like atom interferometer. The first $\pi/2$ pulse of duration τ defines the start of the pulse sequence. After an evolution time $T - 2\tau$ a second pulse of duration 2τ is applied. Finally, after another evolution period of $T - 2\tau$ a third pulse finishes the sequence. During this time the atomic wavepackets travel along physically different paths; *path* 1 and *path* 2.

carrier one-photon Rabi frequencies, and Δ_+ and Δ_c are the detunings from the $|F = 1\rangle \to |F' = i\rangle$ transition for the upper sideband and carrier respectively.

It is possible to show that for a pulse of length τ, the momentum and phase of the atoms change as in Tab. 2.1.

The phase term, $\phi_{\rm eff}$, may have several unwanted contributions in the form of experimental noise which will be discussed in more detail in later sections. Here it is prudent to highlight the fact that in a Mach-Zehnder type interferometer, there are two possible paths that the atomic wavepacket can follow (Fig. 2.4) and the total phase will depend on both paths.

Using Tab. 2.2, one can express the total phase difference accumulated during a full sequence as:

$$\Delta\phi = \phi_{II} - \phi_I = \phi^0_{\rm eff} - 2\phi^T_{\rm eff} + \phi^{2T}_{\rm eff} \tag{2.30}$$

where Path I corresponds to $|a\rangle \to |a\rangle \to |b\rangle \to |a\rangle$ and Path II $|a\rangle \to |b\rangle \to |a\rangle \to |a\rangle$. It is interesting to

note that the AC Stark dependence of the Rabi frequency disappears in Eq. 2.30. This is only true if the interaction time between the light and the atoms is the same for all pulses and will be shown in later sections that a phase shift is accumulated when this is not the case.

Thus the total phase measured by the interferometer depends on the phase difference experienced by the atoms along the different paths. The exact form of the phase shifts that may be encountered are examined in later sections where it will be made clear that for a sensitive measurement of gravity there are several other phase shifts that must first be well controlled.

2.4 Rabi Flopping and Ramsey Interferometry

Rabi Flopping

Returning to Eq. 2.15, let's assume that there is some frequency detuning from resonance and that the atoms are initially prepared in state $|F=1\rangle$ such that $c_2(0)=0$. From this, the probability for an atom to be in states $|F=1\rangle$ and $|F=2\rangle$ oscillates in time according to:

$$P_{|1\rangle}(t) = \left(\frac{\Omega_{\text{eff}}}{\Omega'_{\text{eff}}}\right)^2 \frac{1+\cos\left(\Omega'_{\text{eff}}t\right)}{2} \tag{2.31a}$$

$$P_{|2\rangle}(t) = \left(\frac{\Omega_{\text{eff}}}{\Omega'_{\text{eff}}}\right)^2 \frac{1-\cos\left(\Omega'_{\text{eff}}t\right)}{2} \tag{2.31b}$$

where Ω and Ω' have been replaced by Ω_{eff} and Ω'_{eff} in accordance with Eq. 2.28 for a two-photon transition. The above shows that the excitation probability has a dependence on the frequency detuning from the two-photon resonance, δ_R, encompassed by Ω'_{eff} and on the intermediate level detuning, Δ_R. The effect of two-photon detuning for a fixed intensity is illustrated in Fig. 2.5. One can see that the detuning has two major effects on the Rabi flopping; it simultaneously decreases the contrast of the oscillation whilst increasing the frequency. It is critical that two-photon resonance is satisfied for $\pi/2$ and π pulses to perform optimally. The effect of detuning, Δ_R, is to change the frequency of the Rabi flopping but not the amplitude providing $\delta_R = 0$. This is because the amplitude term in Eq. 2.31 then becomes $\Omega_{\text{eff}}/\Omega'_{\text{eff}} = 1$.

Using Eqs. 2.13 and 2.31, to obtain an experimentally reasonable Rabi frequency of ~ 30 kHz (π time 10 μ s) for a detuning of 2 GHz requires an intensity of 36 mW/cm^2 (see Appendix. A.3). Detuning further is beneficial as it affords a reduced amount of spontaneous emission from incorrect levels but this requires more intensity. In addition, it is beneficial to have a flat intensity profile on the length scale of the atom cloud diameter (i.e. a large diameter beam) to avoid intensity related phase shifts. This places requirements on the minimum power of laser light.

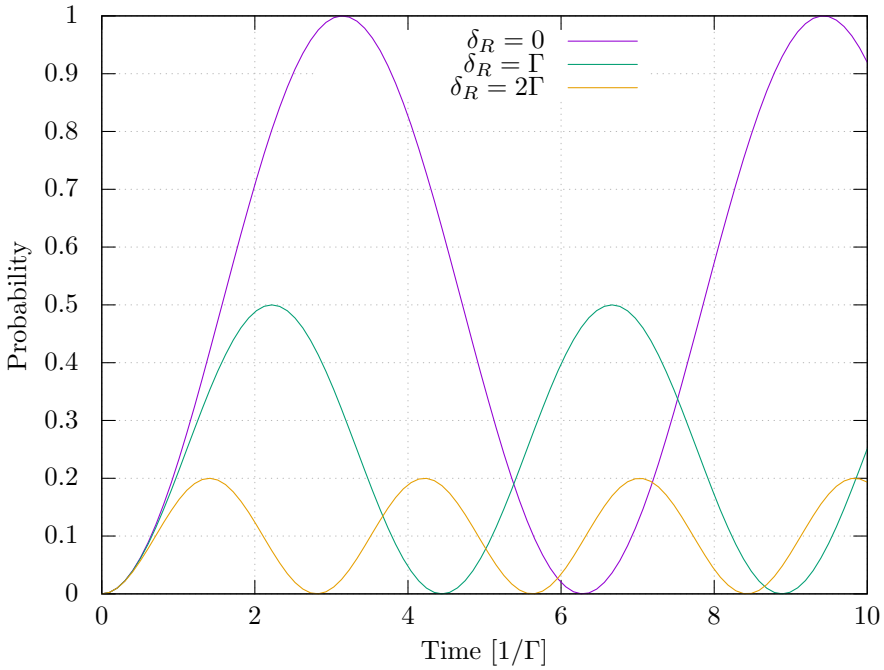

Figure 2.5: Probability for the atom to be in the excited state for different values of two-photon detuning for a fixed intensity. Increased detuning increases the Rabi frequency, Ω_{eff}, whilst decreasing the probability amplitude. $\Omega_{\text{eff}} = \Gamma$ where Γ is the natural linewidth.

The dependence of Rabi flopping on intensity highlights a potential problem in the experiment. A fluctuation in intensity of 10% leads to a change in π time of a similar level. This will result in imperfect state transfer at each of the three laser pulses in the interferometry sequence and will show as noise. The same is true for detuning and hence robust frequency control of the Raman laser is needed.

Ramsey Interferometry

The previous discussion was centered around the interaction between an atom and a single pulse of radiation. Now the case for an interaction with two separate pulses of radiation will be considered as in Ramsey's method of separated oscillatory fields [48]. For a scenario where a $\pi/2$ pulse is applied at time $t = 0$ for a duration τ and a second $\pi/2$ pulse is applied a time $t = T$ for the same duration τ, integration of Eq. 2.12 for the initial conditions $t = 0$, $c_1 = 1$ and $c_2 = 0$ yields [41]:

$$c_2(t) = \frac{\Omega_{\text{eff}}^*}{2}\left(\frac{1 - e^{-i\delta_R\tau}}{\delta_R} + e^{-i\delta_R T}\frac{1 - e^{-i\delta_R\tau}}{\delta_R}\right) \tag{2.32}$$

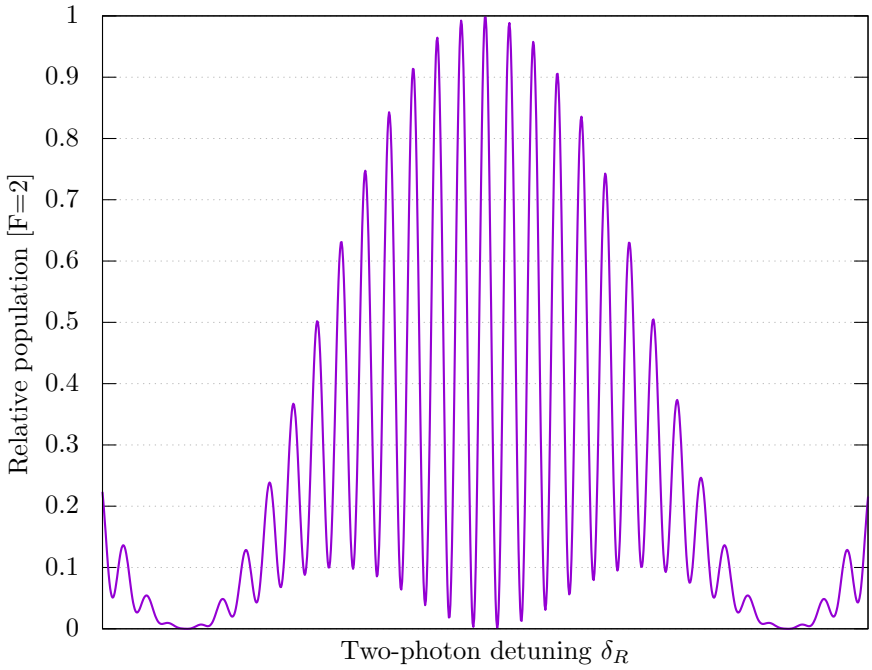

Figure 2.6: Theoretical Ramsey interference fringes from a $\pi/2 - t - \pi/2$ light pulse sequence.

where $\delta_R = \omega_{R1} - (\omega_{R2} + \omega_0)$ and the $\omega_{R1} + (\omega_{R2} + \omega_0)$ terms have been neglected as per the rotating wave approximation. This expression can be broken down into two parts. The first term is simply the amplitude from interacting with the first light pulse whilst the second is the same probability amplitude multiplied by a phase factor due to the free evolution time before the second light pulse. The addition of the phase factor introduces interference when the probability amplitude of an atom being in the excited state is evaluated:

$$P_{|F=2\rangle}(\delta_R) = \left|\frac{\Omega_{\text{eff}}\tau}{2}\right|^2 \left[\frac{\sin(\delta_R\tau/2)}{\delta_R\tau/2}\right]^2 \cos^2\left(\frac{\delta_R T}{2}\right) \tag{2.33}$$

The fringes generated by such an interference effect are known as Ramsey fringes and are of great importance for optical frequency standards [49]. In this report Ramsey fringes will be used as a precursor to gravity measurements in order to study the interference effect from atom wavepacket interactions. The interference fringes generated by a Ramsey sequence offer rich physics for studying various experimental systematics such as laser power and frequency stability without worrying about Doppler sensitive effects. In fact the extension to measuring gravity can be achieved by two Ramsey-interferometry sequences in series in a velocity selective configuration which is commonly known as the "Ramsey-Bordé" interferometer [50].

Fig. 2.6 shows the interference pattern one would expect to see from a Ramsey sequence. The spacing

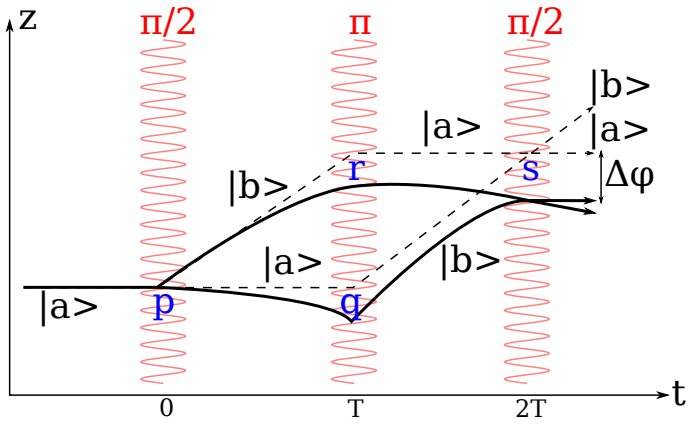

Figure 2.7: Kasevich-Chu interferometer scheme under the effect of phase perturbations. In the ideal case shown in previous figures the path lengths were the same and phase shift was zero. Under the effect of perturbations the path lengths change and a phase shift is measurable.

between fringes is governed by the separation between the $\pi/2$ pulses whilst the envelope is controlled by the length of the pulse. The ratio between the envelope and fringe spacing along with the contrast of the fringes provide useful tools for assessing the performance of the interferometer.

2.5 Interferometer Phase Contributions

In an ideal interferometer scenario, no phase shifts (or at least equal phase shifts) will be encountered during the free evolution of the two wavepackets and when the final $\pi/2$ pulse is applied the wavefunction will return to its original state. This is just mathematical hyperbole and there are many external factors which will introduce phase shifts. It is this fact that is critical in order to make measurements of gravity.

Illustrated by Fig. 2.7, physically separated wavepackets will experience different local forces and hence a phase shift will be observed at the output. One can show that the probability of an atom, initially prepared in state $|1\rangle$, ending up in state $|2\rangle$ follows:

$$P_{|F=2\rangle} = \frac{1}{2}(1 + \cos\Delta\phi_{\text{total}}) \tag{2.34}$$

Using state sensitive detection one can measure the number of atoms in the $|2\rangle$ state and from this calculate a value of gravity from $\Delta\phi_{\text{total}}$. This relies on other phase noise sources being suppressed or well understood. Specifics on the different types of phase shift one might expect in an AI will now be discussed. To start, an overview of the total phase shift encountered at the output of the interferometer is presented.

This can be summarised as a sum of 3 main contributions (Eq. 2.35). Note that these are not tangible quantities which can be separately measured but they help structure the discussion.

$$\Delta\phi_{\text{total}} = \Delta\phi_{\text{laser}} + \Delta\phi_{\text{evolution}} + \Delta\phi_{\text{variable}} \tag{2.35}$$

2.5.1 Phase shift due to interaction with light field

The first term, $\Delta\phi_{\text{laser}}$, is intuitive and corresponds to the phase imprinted on to the atomic wavefunction every time it interacts with the light field. For every atom-laser interaction there is an atomic state change with an associated phase of $\phi_i = \mathbf{k}_{\text{eff}} z_i - \omega_{\text{eff}} t_i$ for position z_i at time t_i. The sign of this phase depends on the initial state of the atom. The components contributing to this phase shift can be found from a Feynman path integral approach for the two possible paths of the interferometer in Fig. 2.7. The phase shift over the region $t = 0 \rightarrow t = 2T$ can be summarised as:

$$\Delta\phi_{\text{laser}} = \phi(p, 0) - \phi(q, T) - \phi(r, T) + \phi(s, 2T) \tag{2.36}$$

This problem can be modelled as a two-level atom crossing a travelling laser wave [51]. We will use the picture of an atom starting at z_0, t_0, interacting at z_1, t_1 and measuring the final wavefunction at z_2, t_2. The solution of this single-interaction model requires careful integration of Lagrangian mechanics which are unnecessary to repeat for this discussion. For simplicity, the final wavefunction is given by:

$$\begin{aligned} \psi_{|b\rangle}(z_2, t_2) = &\exp\{iS_{cl}(z_2 t_2, z_1 t_1)/\hbar\} \\ &\times U_{|b\rangle|a\rangle} \exp\{i(\mathbf{k}_{\text{eff}} z_1 - \omega_{\text{eff}} t_1 - \phi)\} \\ &\times \exp\{iS_{cl}(z_1 t_1, z_0 t_0)/\hbar\} \psi_{|a\rangle}(z_0, t_0) \end{aligned} \tag{2.37}$$

where S_{cl} is the classical action along a path, $\psi_{|a\rangle}(z_0, t_0)$ is the initial wavefunction prepared in state $|a\rangle$ at (z_0, t_0) and $U_{|b\rangle|a\rangle}$ is the transition amplitude from state $|b\rangle$ to $|a\rangle$.

One can repeat the method of Eq. 2.37 for our three pulse sequence to find the final wavefunction by using the appropriate multiplying factor (middle term in Eq. 2.37). Along the path "pqs" the contribution from the laser interactions is:

$$\begin{aligned}\psi^{(pqs)}_{|b\rangle}(z_s, 2T) = &\exp\{iS_{cl}(z_s 2T, z_q T)/\hbar\} \\ &\times U^{(3)}_{|b\rangle|b\rangle} U^{(2)}_{|b\rangle|a\rangle} \exp\left\{i\left[\mathbf{k}_{\text{eff}}\left(z_q - \frac{1}{2}gT^2\right) - \omega_{\text{eff}}T - \phi_{II}\right]\right\} U^{(1)}_{|a\rangle|a\rangle} \\ &\times \exp\{iS_{cl}(z_q T, z_p 0)/\hbar\}\psi_{|a\rangle}(z_p, 0)\end{aligned} \tag{2.38}$$

where $U^{(n)}$ are the transition amplitude matrices at times $t = 0$, T and $2T$, and ϕ_n are the phases at these times. For path "prs" one has:

$$\begin{aligned}\psi^{(prs)}_{|b\rangle}(z_s, 2T) = &\exp\{iS_{cl}(z_s 2T, z_r T)/\hbar\} \\ &\times U^{(3)}_{|b\rangle|a\rangle} \exp\left\{i\left[\mathbf{k}_{\text{eff}}\left(z_r - 2gT^2\right) - 2\omega_{\text{eff}}T - \phi_{III}\right]\right\} \\ &\times U^{(2)}_{|a\rangle|b\rangle} \exp\left\{-i\left[\mathbf{k}_{\text{eff}}\left(z_s - \frac{1}{2}gT^2\right) - \omega_{\text{eff}}T - \phi_{II}\right]\right\} \\ &\times U^{(1)}_{|b\rangle|a\rangle} \exp\left\{i\left[\mathbf{k}_{\text{eff}} z_p - \omega_{\text{eff}} \times 0 - \phi_I\right]\right\} \\ &\times \exp\{iS_{cl}(z_r T, z_p 0)/\hbar\}\psi_{|a\rangle}(z_p, 0)\end{aligned} \tag{2.39}$$

Knowledge of the final wavefunctions from the two paths allows one to write [51]:

$$\Delta\phi_{\text{laser}} = \mathbf{k}_{\text{eff}} gT^2 + \phi_I - 2\phi_{II} + \phi_{III} = \mathbf{k}_{\text{eff}} gT^2 + \Delta\phi_{\text{offset}} \tag{2.40}$$

Ignoring the assumption of a short light pulse and including its finite interaction time, τ, one can finally write:

$$\Delta\phi_{\text{laser}} = \mathbf{k}_{\text{eff}} gT(T + 2\tau) + \Delta\phi_{\text{offset}} \tag{2.41}$$

In principle, this gives a relation for evaluating gravity by sweeping $\Delta\phi_{\text{offset}}$, commonly achieved by varying the phase of the final light pulse, and keeping everything else fixed. However, any noise on $\Delta\phi_{\text{laser}}$ couples directly into the measurement of g and there are several noise sources that have an influence. Phase noise from fluctuations in the interferometry laser as well as static noise introduced by imperfections in the wavefront due to optics will be discussed in the following.

Laser phase noise analysis with the sensitivity function

This section follows the discussion outlined by Cheinet et al. For a more detailed analysis, see [52].

As highlighted in the previous section, a rigorous understanding of the phase imprinted onto the atoms during an interferometry sequence is critical to extract a sensitive measurement. Fluctuations in the phase of the interferometry laser directly influence the phase on the atoms so it is beneficial to understand this effect.

A useful tool that enables one to do such a thing is the so-called Sensitivity Function (SF). The application of the SF to a three-pulse Mach-Zehnder (Kasevich-Chu) interferometer will be discussed here as this is the most relevant to experiment.

Starting with a phase ϕ for the interferometry laser (hereafter referred to as the Raman laser), assume a small perturbation of $\delta\phi$ occurs at a time t which leads to a change in the transition probability $\delta P(\delta\phi, t)$ (see Eq. 2.16).

In the case where the Raman pulses are not infinitesimally short (i.e. $\tau_{\text{Raman}} \approx 1/\Omega_{\text{Rabi}}$), the SF will depend on how the atomic state evolves during the interaction with the pulse. It is therefore necessary to make some assumptions. To start, assume that the laser wavefront is a pure plane wave (i.e. not Gaussian) such that the atomic motion is then quantised with respect to the light. The next assumption is that the Rabi frequency is constant and that the resonance condition is satisfied. This couples the two states of the atom as described in Sec. 2.2.

Defining a basis as in Eq. 2.8, $|\Psi(t)\rangle = c_a(t)\,|a\rangle + c_b(t)\,|b\rangle$, and choosing the initial state to be $|a\rangle$, the transition probability is $P = |C_b(t_f)|^2$ where $t_f = t_i + 2T + 4\tau_R$ and τ_R is the duration of a $\pi/2$ pulse. Therefore $C_a \to C_b$ can be described by:

$$\begin{pmatrix} C_a(t_f) \\ C_b(t_f) \end{pmatrix} = M \begin{pmatrix} C_a(t_i) \\ C_b(t_i) \end{pmatrix} \tag{2.42}$$

where the evolution matrix, M is:

$$M_p(t_0, t, \Omega_R, \phi) = \begin{pmatrix} e^{-i\omega_a(t-t_0)} \cos\left(\frac{\Omega_R}{2}(t-t_0)\right) & -ie^{-\omega_a(t-t_0)} e^{i(\omega_L t_0 + \phi)} \sin\left(\frac{\Omega_R}{2}(t-t_0)\right) \\ -ie^{-\omega_b(t-t_0)} e^{-i(\omega_L t_0+\phi)} \sin\left(\frac{\Omega_R}{2}(t-t_0)\right) & e^{-i\omega_b(t-t_0)} \cos\left(\frac{\Omega_R}{2}(t-t_0)\right) \end{pmatrix} \tag{2.43}$$

The constants of interest here are the Rabi frequency, Ω_R, and the effective frequency $\omega_L = \omega_2 - \omega_1$. With $\Omega_R = 0$ one obtains the free evolution matrix hence the full evolution of the system is described by taking the product of multiple matrices.

Choosing $t = 0$ to be in the middle of the second Raman pulse, one has $t_i = -(T + 2\tau_R)$ and $t_f = T + 2\tau_r$. The sensitivity function, $g(t)$ (for $t > 0$), can finally be written as:

$$g(t) = \begin{cases} \sin(\Omega_R t), & 0 < t < \tau_R \\ 1, & \tau_R < t < T + \tau_R \\ -\sin(\Omega_R(T-t)), & T + \tau_R < t < T + 2\tau_R \end{cases} \tag{2.44}$$

With an expression for the SF in hand, the next logical step is to apply this to the case of the AI. In the three-pulse interferometry scheme there are three times that the Raman laser interacts with the atoms and hence three different phase imprints: ϕ_1, ϕ_2 and ϕ_3. Recalling Eq. 2.40 one can see that $\phi(p,0) = \phi_1$, $-(\phi(q,T) + \phi(r,T)) = -2\phi_2$ and $\phi(s,2T) = \phi_3$. Hence the total interferometric phase is $\Phi = \phi_1 - 2\phi_2 + \phi_3$. Phase noise $\phi(t)$ of the Raman laser leads to fluctuations on the total phase:

$$\delta\Phi = \int_{-\infty}^{\infty} g(t)\,\mathrm{d}\phi \tag{2.45}$$

To calculate the response of Φ one can apply a sinusoidal modulation of the form $\phi(t) = A_0\cos(\omega_0(t)+\psi)$. From this it is possible to show that $\delta\Phi = A_0\omega_0 Im(G(\omega_0))\cos(\psi)$, where G is the Fourier transform of the SF. Therefore;

$$G(\omega) = \int_{-\infty}^{\infty} \mathrm{e}^{-i\omega t} g(t)\mathrm{d}t \tag{2.46}$$

The rms value of the interferometer phase is $\delta\Phi^{rms} = |A_0\omega_0 G(\omega_0)|$ when the modulation phase, ϕ is averaged over a random distribution. The transfer function is therefore $H(\omega) = \omega G(\omega)$. From this one can write down the rms standard deviation of the phase noise as:

$$(\sigma_\Phi^{rms})^2 = \int_0^{\infty} |H(\omega)|^2 S_\phi(\omega)\mathrm{d}\omega \tag{2.47}$$

where $S_\phi(\omega)$ is the power spectral density of the Raman phase.

Calculating the Fourier transform of the sensitivity function reveals:

$$G(\omega) = \frac{4i\Omega R}{\omega^2 - \Omega_R^2}\sin\left(\frac{\omega(T+2\tau_R)}{2}\right)\left(\cos\left(\omega(T+2\tau_R)^2\right) + \frac{\Omega_R}{\omega}\sin\left(\frac{\omega T}{2}\right)\right) \tag{2.48}$$

Linking the sensitivity of the interferometer to the sensitivity function requires one final step. The sensitivity of the interferometer is characterised by the Allan variance of the phase fluctuations, $\sigma_\Phi^2(\tau)$:

$$\sigma_\Phi^2(\tau) = \frac{1}{2}\left\langle(\delta\bar{\Phi}_{k+1} - \delta\bar{\Phi})k)^2\right\rangle = \frac{1}{2}\lim_{n\to\infty}\left\{\frac{1}{n}\sum_{k=1}^{n}(\delta\bar{\Phi}_{k+1} - \delta\bar{\Phi}_k)^2\right\} \tag{2.49}$$

where $\delta\bar{\Phi}_k$ is the average value of $\delta\Phi$ over the interval $[t_k, t_{k+1}]$ of duration τ.

If the interferometer is operated at a rate $f_c = 1/T_c$ and τ is a multiple of T_c (i.e. $\tau = mT_c$) then one can write $t_k = -T_c/2 + kmT_c$ and:

$$\begin{aligned}\delta\bar{\Phi}_k &= \frac{1}{m}\sum_{i=1}^{m}\delta\Phi_i \\ &= \frac{1}{m}\sum_{i=1}^{m}\int_{t_k+(i-1)T_c}^{t_k+iT_c} g(t-t_k-(i-1)T_c-T_c/2)\frac{\mathrm{d}\phi}{\mathrm{d}t}\mathrm{d}t \\ &= \frac{1}{m}\int_{t_k}^{t_{k+1}} g_k(t)\frac{\mathrm{d}\phi}{\mathrm{d}t}\mathrm{d}t\end{aligned} \tag{2.50}$$

The difference between successive values is:

$$\delta\bar{\Phi}_{k+1} - \delta\bar{\Phi}_k = \frac{1}{m}\int_{-\infty}^{\infty}(g_{k+1}(t)-g_k(t))\frac{\mathrm{d}\phi}{\mathrm{d}t}\mathrm{d}t \tag{2.51}$$

Hence the Allan variance can be written as:

$$\sigma_\Phi^2(\tau) = \frac{1}{2}\frac{1}{m^2}\int_0^\infty |G_m(\omega)|^2\,\omega^2 S_\phi(\omega)\mathrm{d}\omega \tag{2.52}$$

and

$$|G_m(\omega)|^2 = 4\frac{\sin^4(\omega m T_c/2)}{\sin^2(\omega T_c/2}\,|G(\omega)|^2 \tag{2.53}$$

For large averaging times:

$$\sigma_\Phi^2(\tau) = \frac{1}{\tau}\sum_{n=1}^{\infty}|H(2\pi n f_c)|^2\,S_\phi(2\pi n f_c) \tag{2.54}$$

Eq. 2.54 is an important result. One can apply this to the laser phase noise, assuming white Raman phase noise, and arrive at:

$$\boxed{\sigma_\Phi^2(\tau) = \left(\frac{\pi}{2}\right)^2\frac{S_\phi^0}{\tau}\frac{T_c}{\tau_R}} \tag{2.55}$$

Which shows that the sensitivity of the interferometer depends also on the duration of the interrogation pulses. The message to take from this section is that it is necessary to have robust phase control of the two frequencies needed for the Raman transition and, for a large sensitivity, one should used the longest pulse lengths feasible. However, there is a tradeoff as longer pulse lengths reduce the number of useful atoms due to the velocity selective nature of the Raman beams and one must optimise pulse length with respect to experimental parameters.

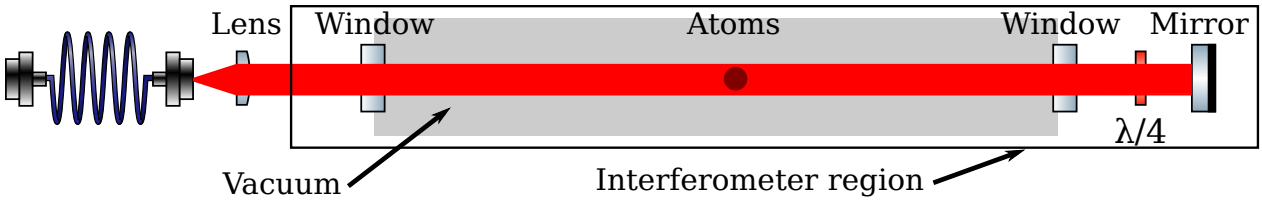

Figure 2.8: Optical elements in the beam path of the atom interferometer. Divergent light exiting a fibre passes through a lens to create a parallel beam. The light passes through a window into vacuum, through the atoms and through another window out of vacuum where it is retroreflected. In the standing wave picture the first window is common to both beams whilst the second window, waveplate and mirror are unique to only the second beam.

Phase noise due to wavefront aberrations

At the level of precision an AI can achieve, distortions to the wavefront of the Raman beams caused by optical elements have a sizeable effect. However, these distortions are static and in principle one can use a theoretical understanding to compensate for this particular noise source. Based on the theory outlined in [53], the uncertainty in a gravimeter can be reduced to less than $3 \times 10^{-10} g$.

It has already been shown in Eq. 2.30 that the total phase accumulated depends on the phase of the Raman beams at the time of the three pulses. Up until now it was assumed that the three Raman pulses were plane waves so all atoms experienced the same phase shift, independent of their position with respect to the wavefront of the beam. For any arbitrary wavefront, the phase shift of an atom will depend on its position with respect to the beam.

$$\Delta\phi_n = \phi(\vec{r_n}(t_1)) - 2\phi(\vec{r_n}(t_2)) + \phi(\vec{r_n}(t_3)) \tag{2.56}$$

where the subscript n denotes the n^{th} atom and t_i are the times of the Raman pulses.

It is clear that the phase shift is not the same for all atoms within the ensemble. Based on this fact one can predict that the error in phase will depend on the initial atomic density distribution, the expansion during free evolution and whether or not the detection scheme is spatially sensitive.

Of course, due to the nature of the experiment involving counter-propagating beams, any aberrations that are common to both beams will cancel but those related to only one beam will remain.

In an experiment like this the light in the interferometer region passes through a window, the atoms, a window, a quarter waveplate, is reflected by a mirror and passes through the same optics on the return journey. Of these elements only the first window is common to both atom-laser interactions and can be ignored. The retroreflected beam has additional phase shifts from passing through the second window and waveplate twice as well as contributions from the mirror. The effective wavefront error can be expressed as:

$$\delta\phi_{\text{eff}} = 2 \cdot \delta\phi_{\text{window}} + 2 \cdot \phi_{\lambda/4} + \delta\phi_{\text{mirror}} \tag{2.57}$$

The exact phase shift caused by each element can be extracted from measurement [54] and fed into Eq. 2.57 to calculate the total shift.

2.5.2 Phase shift due to free evolution

The next term, $\Delta\phi_{\text{evolution}}$, encompasses the phase shifts that happen to the two individual wavepackets from their internal evolution along the different paths as in Fig. 2.7. The exact solution to the path integrals can be solved with Lagrangians. The results of [51] are used here to demonstrate what happens to the two arms of the interferometer in a gravitational potential. The ideas can be extended to other potentials in a similar manner and a total phase contribution established. Introducing z as the vertical position of the atoms and set $z_p = 0, t_p = 0$. The expressions one arrives at are then:

$$z_q = -\frac{1}{2}gT^2 \tag{2.58}$$

the displacement due to uniform gravity,

$$z_r = -\frac{1}{2}gT^2 + \frac{\hbar\mathbf{k}_{\text{eff}}}{m}T \tag{2.59}$$

the displacement due to uniform gravity and photon momentum,

$$z_s = -2gT^2 + \frac{\hbar\mathbf{k}_{\text{eff}}}{m}T \tag{2.60}$$

In addition, using the equation for phase evolution between two spacetime points as derived in [55]

$$\Delta\phi_{a\to b} = \frac{S_{cl}(z_b t_b, z_a t_a)}{\hbar} \tag{2.61}$$

to write down the total phase for free evolution, where S_{cl} is the action along a classical path:

$$\begin{aligned}
\Delta\phi_{\text{evolution}} &= (\Delta_{p\to q} + \Delta_{q\to s}) - (\Delta_{p\to r} + \Delta_{r\to s}) \\
&= \frac{m}{\hbar T}\left[z_q^2 - z_r^2 - z_q z_p - z_s z_q + z_r z_p + z_s z_r - z_q g T^2 + z_r g T^2\right] \\
&= 0
\end{aligned}$$

For a uniform gravity potential, the contribution to free evolution phase is zero and the important quantity is the phase due to interaction with the lasers. In fact one may assume that any uniform potential acting on both wavepackets will have no effect on the output of the interferometer as both wavepackets should be affected in the same manner.

2.5.3 Phase shift from non-uniform fields

The last term of the three, $\Delta\phi_{\text{variable}}$, is concerned with the phase shifts that occur due to non-uniform fields during free-evolution. It is an inevitable fact that some non-uniform potentials will be present during the free evolution period of the interferometer and these will contribute phase terms which alter the interference pattern. Magnetic fields, electric fields and even gravity are all examples of non-uniform potentials that may contribute. The exact influence that these potentials will have is unique to the type of potential and will be discussed in a little more detail in the following section.

2.6 Individual Phase Contributions

To the interested, [3–5, 38] compile detailed and useful lists for these contributions for a similar experimental design. They are repeated here to provide an understanding of the noise sources which must be considered.

2.6.1 Inertial Phase Shifts

Whilst every effort is made to control external influences on the experiment, it is likely that there will be some effect and so it is crucial that these are understood. The application of any external force to the atomic ensemble via environmental fluctuations will induce an acceleration. As a consequence of this, the ensemble will move relative to the laser wavefronts of the Raman interferometry beams. This in turn will be interpreted as a phase shift caused by the imperfect flatness of the Raman wavefront and sensitivity to gravity will be lost.

Uniform gravity

It has already been mentioned that in a uniform gravitational potential, the contribution to free-evolution phase shift is zero. There is a subtlety to this however as one must take into account that as the atom is moving in the gravitational potential and hence being accelerated, its velocity is changing. In the case that the atomic ensemble and Raman beams are parallel, a Doppler shift will occur due to the relative motion of the atoms with respect to the laser beams. This means that resonance will be lost very quickly as the atoms

accelerate and so the Raman beam frequency must be ramped to compensate. In fact it is this ramping that exactly cancels the acceleration caused by gravity that is used to determine the value of gravity and was already derived in Eq. 2.40.

$$\Delta\phi_{\text{laser}} = \mathbf{k}_{\text{eff}} g T^2 \tag{2.62}$$

Taking a chirp rate, α, and unwanted sources of phase shift, ϕ_L, one can rewrite the above equation as [43]:

$$\Delta\phi = (\mathbf{k}_{\text{eff}} g - 2\pi\alpha)T^2 + \phi_L \Rightarrow g = 2\pi\alpha_0/\mathbf{k}_{\text{eff}} \tag{2.63}$$

where α_0 denotes $\Delta\phi = 0$ and has been chosen to include ϕ_L.

Gravity gradient

This inertial shift is more apparent in gravimeters in which a single atom cloud is used for measurements where it appears as a noise source. In this experiment two atom clouds will be physically separated on the order of centimetres, both interrogated by the same lasers so the gradient itself can be accurately probed. The resultant phase shift for this case is then:

$$\Delta\phi_{\text{grad}} = \mathbf{k}_{\text{eff}} \gamma \Delta h T^2 \tag{2.64}$$

where γ is a gradient ($\sim 3 \times 10^{-6}$ s^{-2} on Earth). For this experiment with $\Delta h \approx 50$ cm and $T \approx 300$ ms this gives a phase shift on the order of $10^{-7}g$.

Earth Rotation

Coriolis forces can alter the measured phase due to the alignment of the Raman beams fluctuating and the horizontal velocity distribution of the atoms. If the alignment of the Raman beams with respect to the atomic clouds is not constant for every pulse in the sequence then some horizontally varying phase shifts will be imparted to the atoms. By controlling the angle of the Raman beams with an adjustable mirror one can either cancel the Coriolis effect by keeping the effective wavevector seen by the atoms constant or measure the effect of rotations [32].

The rotation of the Earth displaces the position of the atoms with respect to the beams which induces a phase shift according to:

$$\Delta\phi_{rot} = 2\mathbf{k}_{\text{eff}} \cdot (\mathbf{\Omega} \wedge \mathbf{v})\, T^2 \tag{2.65}$$

where $\mathbf{\Omega}$ is the rotation rate of the Earth and $\mathbf{v}$ is the the atom's velocity.

For a gravimeter, this corresponds to a gravity offset given by [56]:

$$\Delta g = 2\mathbf{\Omega} \cdot (\mathbf{v} \wedge \hat{\mathbf{v}}_{\text{rec}}) \tag{2.66}$$

with $\hat{\mathbf{v}}_{\text{rec}}$ as the normal vector of the photon recoil. For $\mathbf{\Omega} \approx 73$ μrad/s and the latitude in Birmingham ($52.48°$) this gives a gravity offset of $\Delta g \approx 90$ μrad/s$\cdot$v$_{\text{EW}}$. From this relation and work done in [4, 38, 56] it is expected that this shift will be in the region of mrad ($\Delta g \approx 100$ nm/s^2) for each mm/s of horizontal velocity on the atoms. A gravity gradient accuracy of 1 Eötvös requires 50 pg accuracy for a single gravity measurement [1]. This requires that v$_{\text{EW}} < 6$ μm/s and hence a requirement on the verticality of the atom launch < 1.6 μrad without Coriolis compensation.

Tilt Alignment

For the case of a gradiometer with simultaneous interrogation of two clouds the first order phase shift from Coriolis can be expressed as [4]:

$$\Delta\phi = -2\mathbf{\Omega}\mathbf{k}_{\text{eff}} T^2 (v_1 - v_2) \cos\alpha_l \sin\theta \tag{2.67}$$

where v_1 and v_2 are the velocities of the two clouds and α_l is the latitude angle mentioned previously. Theoretical parameters for this experiment of $v_1 = 3.7$ m/s, $v_2 = 1.7$ m/s and $T = 150$ ms give $\Delta\phi \approx -64\theta$ under the small angle approximation. If the fractional change in phase is equivalent to the fractional change in gravity gradient and tilt alignment appears as a $\cos(\theta)$ multiplication then one has $\cos(\theta) = 1 - 1 \times 10^{-9} \Rightarrow \theta \approx 44$ μrad. Therefore for a gradiometer the tilt must be aligned to < 2.8 mrad.

Electric and Magnetic Fields

Homogeneous electric fields can probe matter neutrality because charge imbalances cause an acceleration proportional to qE/m. Other experiments aim to determine if there is a charge imbalance between protons and electrons [57] and rely on the fact that inhomogeneous electric fields cause a phase shift due to energy level splitting. A field will shift the ground state energy by:

[1] 0.5 m separation between clouds so 1 E $\rightarrow 5 \times 10^{-10}$ ms^{-1} = 50 pg

$$\Delta E = -2\pi\epsilon_0\alpha\ E^2 \tag{2.68}$$

causing an acceleration:

$$\mathbf{a} = \frac{4\pi\epsilon_0\alpha E}{m}\frac{dE_z}{dz}\frac{\mathbf{z}}{|\mathbf{z}|} \tag{2.69}$$

and hence a phase shift.

Magnetic fields cause phase shifts both inertially and in terms of frequency (due to the Zeeman effect). In the inertial case, the dipole moment of an atom in a magnetic field causes an acceleration according to:

$$\mathbf{a} = \frac{1}{m}\nabla\left(\mu\cdot\mathbf{B}\right) = \frac{1}{m}m_F\mu_B g_F\frac{dB_z}{dz}\frac{\mathbf{z}}{|\mathbf{z}|} \tag{2.70}$$

if a bias magnetic field is applied along the z axis. In the event that this field is perfectly uniform, a similar phase shift to that of gravitational fields will be observed. If the applied field has spatial variations in z then this will cause an acceleration for atoms in accordance with their m_F number. To mitigate this, one can prepare atoms in the $m_F = 0$ state as this is the least magnetically sensitive. Comparison with the $m_F = 1$ shows a difference of several orders of magnitude ($\approx\ 6\times10^{-9}g$ versus $\approx\ 3\times10^{-5}g$).

2.6.2 Frequency Phase Shifts

When the atoms first interact with the Raman light pulse it induces an electric dipole with proper frequency ω_0. As the atoms evolve in the free time between Raman pulses, this dipole will oscillate. The effect of this frequency oscillation with other field oscillations is that phase shifts may be accumulated in the case that the frequencies of the two are not matched for the entirety of the interferometer sequence. Some potential field oscillations that may interact with the electric dipole oscillation are discussed below.

Zeeman shift

The Zeeman effect was mentioned briefly in the previous section as a potential cause of phase shifts due to the interaction of atoms and external magnetic fields. In the presence of a magnetic field, the degeneracy of the energy levels in the atom is removed and the m_F number starts to play a very important role. There is a shift applied to the energy sublevels of the atom which depends on both the strength of the magnetic field and the m_F number. For $m_F = 0$ the shift is zero to first order but second order effects will occur. Therefore, if there is a change of magnetic field between Raman pulses there will be an energy shift applied to the sublevels which will alter the atomic resonance. Assuming the frequency of the Raman pulses remains

the same then there will be a phase shift induced due to this frequency difference:

$$\Delta\phi_{z,II} = 2\pi \int_{T}^{2T} a_{z,II} \left|\mathbf{B}(t)\right|^2 \mathrm{d}t \tag{2.71}$$

As an example, a 100 mG magnetic field perturbing the atoms for 10 ms would induce a phase shift of 361 mrad [38].

It has been discussed that there are two different ways in which magnetic fields can have an adverse effect on AI sensitivity. For this reason it is essential that they are well controlled during the interferometry sequence. This means preparing the atoms in the $m_F = 0$ state to make them least susceptible to magnetic fields but there are other steps that must be taken to sufficiently weaken the effect. One option is to use a passive system to attenuate external magnetic fields. This would involve several layers of high permeability magnetic shielding, most commonly made from MuMetal [58] or Metglas [59].

AC Stark shift

In the two-photon Raman scheme used in this experiment there exists an excitation to a virtual sub-level which has some detuning Δ_R from the true excited state that is much greater than both the two-photon detuning δ_R and the linewidth of the virtual level. This detuning is chosen in order to make spontaneous emission negligible and allows one to treat the system like a two-level transition. However, a light beam detuned from resonance induces an opposite shift on the energy levels of the transition.
The ac Stark shift for a particular level is calculated from the Rabi frequency of the transition [20]:

$$\Omega_i^{AC} = \sum_{k,j} \frac{|\Omega_{kji}|^2}{4\Delta_{kji}} \tag{2.72}$$

where $i = 1, 2$ are the ground states, $j = 0, 1, 2, 3$ are the four excited states and $k = 1, 2$ are the two laser beams. To cancel this shift in our interferometer, we require that $\Omega_1^{AC} = \Omega_2^{AC}$ which enforces a particular ratio of I_2/I_1 for a fixed single-photon detuning, Δ_R, which must be experimentally measured.

DC Stark shift

In a similar manner to Zeeman shifts, an electric field can also induce a phase shift by changing the differential energy splitting of the hyperfine levels. If the field is static and uniform and present throughout the entire interferometry sequence then the effect cancels. However, if the field is only present for part of the sequence

(say the latter half) then one gets a phase shift given by:

$$\Delta\phi_{DC} = 2\pi \int_{T}^{2T} a_{DC} \left|\mathbf{E}(t)\right|^2 \mathrm{d}t \tag{2.73}$$

This shift is in the region of mrad and hence much less impactful than other contributions but care must still be taken in the event it becomes the dominant shift once others are cancelled.

Summary of Phase Shifts

Summarised here are the potential phase shifts encountered in a gravity gradiometer, ranking them in order of their relative size for a laboratory-based experiment.

Type of Shift	**Size (rad)**
Gravity	7×10^6
Gravity gradient	$\approx$ 1
Zeeman effect	$\approx$ 0.1
Rotations	$\approx$ 0.068 per mm/s
Magnetic gradient	0.002
DC Stark	0.001

Table 2.2: Rough estimation of phase shifts encountered in a gravity gradiometer based on similar experiments. [3,38]

Apparent from this table is that gravity gradient effects are a similar order of magnitude as rotational and magnetic phase shifts. This highlights the importance of cancelling both horizontal momentum and stray magnetic fields in the region of the interferometer.

Portability Considerations

The phase shifts mentioned above are assuming the experiment is placed inside a relatively well controlled laboratory. Magnetic field and Coriolis rotation phase shifts are location dependent but the process for compensation is identical when operated in the field. However, there are additional phase considerations for which one must account such as environmental factors and tilt.

In the United Kingdom outdoor temperature can vary as much as ± 10 °C[1] over the course of a day. For optical components this can result in misalignment or polarisation drifts. With fibre optic components such

[1] Personal experience...

as beamsplitters this can have an appreciable change (a few %) in the splitting ratio. Whilst these effects are a slow drift they will introduce noise through changes in beam balance for trapping and Raman interrogation.

There is a subtlety to Coriolis compensation that needs to be addressed for field operation. Standard experimentation assumes that the experiment is well levelled coarsely and there is a controllable mirror on a piezo that fine adjusts the angle to correct for Coriolis. In the field it is difficult to optimise coarse levelling in real time and to fix the tilt of the experiment with respect to true north. The result is that the effective wavevector from the two Raman beams will not always be corrected by the mirror and phase noise will be introduced.

CHAPTER 3

EXPERIMENTAL APPARATUS

This chapter focuses on the design and construction of the experiment "GGtop"; a transportable gravity gradiometer for field applications. This experiment was the first investigation into building a gradiometer in Birmingham and some design choices were not completely optimal. These will be reflected in chapter 4.

Presented first is an overview of the experiment, describing the apparatus in its current state. With this in mind, the focus will shift to select areas with which the author has had more interaction. These areas include the light distribution system required to create the trapping and detection beams, the detection system itself and the Raman lasers for the interrogation pulses. There will also be a discussion on the proposed magnetic shielding for the experiment as this will have a heavy influence on future measurements as outlined in section 2.6.1. All information presented here is accurate at the time of writing this thesis.

3.1 Experiment Overview

Design Considerations

The experiment is designed as a gravity gradiometer where interferometry on two atom clouds is performed at spatially different positions. From Sec. 1.3.4 we are aiming to realise a sensitivity of 1 E to detect typical underground utility infrastructure of approximate size 10 cm diameter and mass of a few kg. This requirement is fulfilled by having two 10^{-9} ms^{-2} gravimeters separated by a metre and scales inversely with their separation via:

$$\gamma = \frac{g_2 - g_1}{\Delta z} \tag{3.1}$$

Assuming all external noise sources are suppressed to the point where the experiment is shot noise limited [60] (an unrealistic but helpful picture), the sensitivity of the device will scale only with the number of atoms interacting in the interferometer as [61]:

$$\Delta g = \Delta\phi/(\mathbf{k}_{\text{eff}}T^2)t^{1/2} = (1/\sqrt{N})/(\mathbf{k}_{\text{eff}}T^2)t^{1/2} \tag{3.2}$$

where N are the number of atoms and t is the integration time. To maximise the sensitivity it is therefore imperative to have as many atoms interacting as possible but there is a tradeoff which will now be discussed.

For an atom interferometer operating with two-photon Raman transitions as in this experiment there is a loss of atoms due to spontaneous emission when there is a direct excitation to the excited state rather than a temporary excitation to the intermediate state. The fraction of atoms lost in this way scales as $1/\Delta_R$ (recall Δ_R is the detuning of the intermediate state from the excited levels) and so it is prudent to increase Δ_R to mitigate atom loss.

Increasing Δ_R cannot continue without limit however, as Ω_{eff} also scales as $1/\Delta_R$ and hence intensity must be increased to prevent $\tau_\pi = \pi\Omega_{\text{eff}}^{-1}$ from becoming too large and prohibitively velocity selective. It is beneficial to maintain high Rabi frequencies as for longer pulses the velocity selection of atoms becomes increasingly narrow, selecting only the coldest atoms:

$$v_z = \frac{\Delta\omega}{k_{\text{eff}}} \quad \text{where} \quad \Delta\omega \approx 1/\tau_\pi \tag{3.3}$$

Typical experiments with similar functionality to this one aim for a $\tau_\pi \lesssim 100$ μs [17, 38] giving $v_z \sim 3.9$ mm/s.

Assuming a molasses cooled sample of 10^9 atoms at 2 μK (like that achieved by [62]) and that spontaneous emission losses are negligible from large detuning, selecting the velocity class above reduces the total number of atoms to $\sim 2.2 \times 10^8$. Following Eq. 3.2 for a free-evolution time of 100 ms gives a sensitivity of $\Delta g = 4.16 \times 10^{-10} \mathrm{ms}^{-2}/\sqrt{\mathrm{Hz}}$. This result suggests that the required gradient sensitivity could equally be achieved with ~ 0.5 m separation and places a requirement on the number and temperature of the atoms mentioned previously.

It must be stressed that this is an optimistic lower limit. In reality there are many noise sources, such as those discussed in Sec. 2.6, which will limit the experimental performance. It is our job to minimise these sources of noise wherever possible to reach the sensitivity described here.

To achieve gradiometry we will be launching two atom clouds along the vertical direction via the method of juggling outlined in [38] and illustrated in Fig. 3.1. Essentially, the first cloud is launched for some time while a second cloud is loaded. After the second cloud has been launched, the first cloud is quickly recaptured for cooling and is then launched once more so that both clouds are in flight with similar atom numbers and temperatures. The choice of method here is such that the two atom clouds make simultaneous parabolic flights with higher atom number than would be achievable by loading and launching two clouds in quick succession. Both clouds can subsequently be interrogated by the same Raman laser pulses to give common mode noise rejection (see Fig. 3.1). For high data rates it is necessary that both clouds can be prepared relatively quickly and there is a maximum time for which the second cloud can be loaded based on the time of flight of the first cloud in the juggle.

Tab. 3.1 outlines the planned experimental sequence for the gradiometer. What it highlights are some key parameters with regards to experiment design.

- To realise the gradiometer juggling scheme we need to be able to load a second cloud whilst the first is in free flight. If only 500 ms are available to load the second cloud (limited by the launch height of the first cloud being juggled) then high loading rates are needed. For the large atom numbers of 10^9 required to achieve the designed sensitivity, atom loading rates of $> 10^9$ (ideally 10^{10}) atoms/s are required. Loading from a vapour cell is undesirable as the high vapour pressure needed to load rapidly would increase background collisions in the interferometer and destroy coherence. The most acceptable solution for a high-flux atom source is from a 2D MOT with a differential pumping stage which pre-cools atoms and allows for rapid loading into the 3D MOT whilst maintaining low pressure in the 3D MOT region. This also allows for a controllable method for rapidly turning off the atom source. A 2D MOT is preferable over alternative pre-cooling devices such as Zeeman slowers as they

can be made much more compact which is important for the portability of the experiment.

- To launch atoms there must be a method of imparting vertical velocity to the atoms either by frequency control to detune the trapping beams by an amount roughly equivalent to the desired launch velocity or by creating a standing wave moving lattice with a vertical beam. This experiment will use the method of detuning the 3D MOT trapping beams to create a moving molasses which accelerates the atom cloud as this method is more technologically mature. Acousto-optic modulators (AOMs) will be used to realise frequency detuning of the trapping light as they are more efficient, in terms of light intensity, for small frequency shifts when compared to sinusoidally driven electro-optic modulators (EOMs). It is beneficial to preserve light intensity wherever possible to mitigate the need for laser amplifiers which would reduce portability. To reach launch heights of < 1 m requires that we can detune the trapping beams on the order of 5 MHz which is easily achievable with a single pass AOM possessing a bandwidth $\sim 10\%$ of its central frequency.

- State preparation and velocity selection require precise manipulation of atomic states through a combination of microwave and light fields. Following preparation and selection we must retain a good atom number on the order of 10^8 to achieve a good sensitivity. Microwave state transfer for preparation is an efficient ($\sim 100\%$) process providing the frequency driving the microwave transition is robustly frequency stabilised. The stability of the microwave signal is doubly important as it will act as the frequency difference between the two Raman lasers in the velocity selection and interferometry sequence. This will require unavoidable bulky electronics so intelligent packaging should be used to minimise the impact on portability.

- For Raman interrogation a flat wavefront is desirable for the entire atom cloud to see a uniform intensity even as the cloud expands and this can approximately be achieved by using a large diameter beam to mitigate the Gaussian falloff of intensity with radius. To achieve a reasonable intensity with a large diameter beam places a constraint on the minimum laser power as the intensity scales quadratically with this quantity. Recalling the argument for Δ_R and spontaneous emission discussed earlier in this section enforces that as Δ_R is increased the laser intensity must increase to keep the Rabi frequency experimentally reasonable. We will take the design approach of a large Raman beam to ensure we have a flat wavefront and we will use a large detuning such that we can be confident we're not limited by spontaneous emission. Both of these design choices need high laser intensity which requires that some portability will be sacrificed to accommodate a large laser amplifier.

Experimental Sequence

The experimental sequence has several important steps which are featured in Tab. 3.1. Here the steps will be discussed more thoroughly to paint a picture of what is happening at each step.

1. Based on the previous design parameters, the first atom cloud is loaded for 500 ms to achieve 10^9 atoms. We want to load as many atoms here as possible so that more can be recaptured later in the juggling scheme. For this reason it is possible to extend this initial loading period if necessary.

2. In order to launch the first cloud and recapture it with good efficiency we require that it is cold to minimise thermal expansion greater than the scale of the capture region. For this reason the first cloud undergoes a period of molasses cooling prior to launching to reach low μK temperatures.

3. Immediately after the molasses cooling period the first cloud is launched. The velocity given to the launch is enough that the flight time allows for a sufficient number of atoms to be loaded in the second cloud.

4. Once the first cloud has cleared the MOT region the second cloud can begin to load. The time which this cloud can load is limited by the flight time of the first cloud which is, in turn, limited by the height of the experiment.

5. An identical molasses cooling stage is applied to cloud 2 to reduce the temperature and minimise thermal expansion for its ballistic flight.

6. The second cloud is launched shortly before the first cloud reaches the capture region with a velocity sufficient to apex near the very top of the apparatus in order to achieve maximum separation of the clouds and maximum gradient sensitivity.

7. After a short flight time the second cloud reaches a region of the experiment where preparation and selection can occur. Here a sequence of microwave and light fields are applied to the atoms to prepare them exclusively in the $|F = 1, m_F = 0\rangle$ state to make them minimally sensitive to magnetic fields. A narrow velocity slice of the atoms is selected by a short pulse of the Raman light to minimise loss of coherence from dispersion of hotter atoms during the interferometry sequence. The exact velocity class selected is something to be experimentally optimised based on available Raman intensity and detuning and the desired number of atoms needed to reach a sensitivity level.

8. The first cloud is recaptured for a short time to refresh the number of atoms and re-cool them. This is an efficient process as the cloud has not expanded much compared to its initial size.

9. Another molasses sequence is performed on the cloud to once again reach low temperatures before launching.

10. The first cloud is again launched but this time with a lower velocity to apex at lower height than the second cloud which is still in free-flight. The height to which this cloud is launched is a parameter which will have to be experimentally optimised as there is a trade-off between the separation of the clouds and the evolution time between Raman pulses which both scale with the height of this cloud.

11. After a small flight time the first cloud undergoes state preparation and velocity selection in an identical manner to the second cloud.

12. This step highlights only the π pulse because it is the most significant with regards to symmetry. This pulse should coincide with both clouds reaching their apex but not too close to the apex where Doppler effect from the clouds becomes minimal. The $\pi/2$ pulses occur a symmetric spacing either side of this central pulse with the largest possible separation as sensitivity scales with T^2.

13. Detection of the clouds occurs sequentially with cloud 1 reaching the detection region first. The detection sequence consists of state sensitive detection with static light sheets to measure the relative population in the $|F = 1\rangle$ and $|F = 2\rangle$ states. This gives a measure of the phase shift encountered in the interferometer normalised to the total number of atoms.

14. A short time later, cloud 2 reaches the detection zone and an identical detection sequence is used to probe the phase shift. A gradient signal can then be deduced from the two gravity measurements and their separation at the π pulse.

Preliminary Study with Ramsey Interferometry

The information presented above details how a gravity gradient measurement will be made. Before we make gravity measurements there is a useful step that can be taken to study various experimental systematics by performing a velocity insensitive interferometry sequence. This was outlined in Sec. 2.4 and will be presented in Chapter. 4.

A Ramsey interferometry sequence can be done immediately following molasses cooling of a cloud or at any point following a launch to assess how the system is behaving. Removing the Doppler effect as a noise source allows for characterisation of the stability of various components in the experiment; in particular the timing sequence reproducibility along with the laser short and long term frequency and intensity drifts.

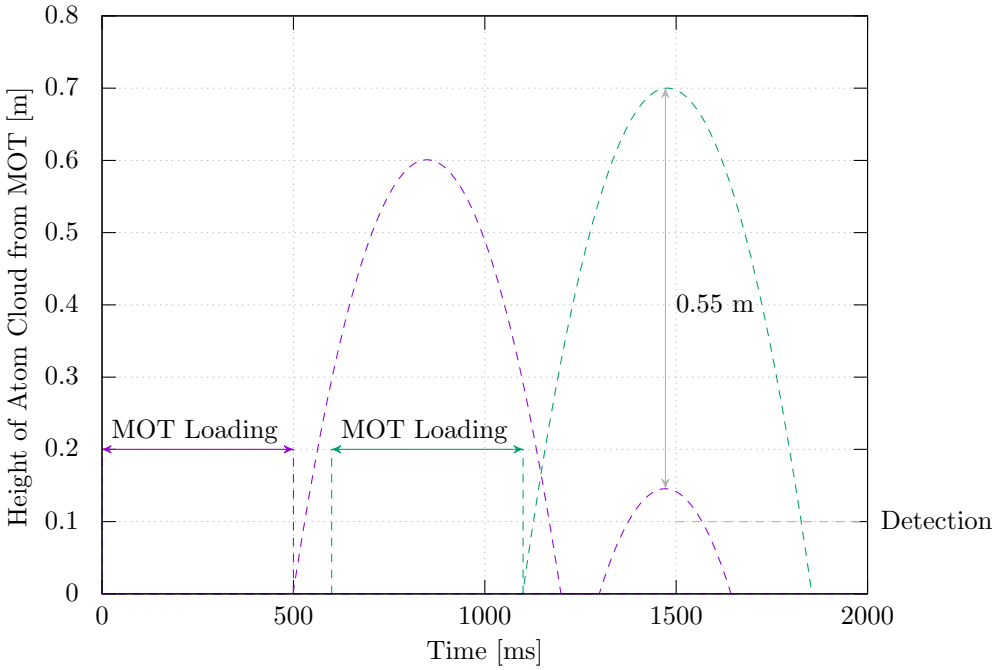

Figure 3.1: Parabolic flight of two atom clouds under the juggling scheme. The first cloud is loaded in the MOT for 500 ms before being launched at 3.4 m/s for a flight time of 700 ms. A second cloud is loaded at 600 ms for 500 ms before being launched at 3.7 m/s for a flight time of 755 ms. The first cloud is recaptured at 1300 ms for 100 ms before being relaunched at 1.7 m/s such that the apexes occur at the same time. A free evolution time, T, between Raman pulses of 100 ms is achievable. Free evolution time can be increased by decreasing the separation between apexes and an experimental optimum must be found. Exact timings will need to be experimentally optimised.

The Experiment

Fig. 3.2 shows the fully assembled experiment. Focusing on the vacuum components, moving from the left to right of the image there is; 2D MOT chamber connected to a small ion pump (Gamma Vacuum), 3D MOT chamber connected to the vertical interferometry region and a Non-Evaporable Getter (NEG) (SAES Group). To the right of the vacuum system is the housing for the lasers (New Focus Vortex 6900) and spectroscopy module. At the base of the experiment sits the fibre-optic system used to distribute light to the necessary parts of the experiment. The experiment is comprised of just two modules: a science package of size $1200 \times 50 \times 1500$ mm^3 and 19-inch electronics rack of height 2000 mm.

3.2 Vacuum System

One can separate the vacuum assembly into five main components: rubidium source, 2D chamber, 3D chamber, interrogation region and vacuum pumps.

The rubidium source consists of a glass ampoule filled with 1 gram of material. Once vacuum had been

Step	Stage	Start (ms)	Length (ms)	Information
1	Load cloud 1	0	500	10^9 atoms
2	Molasses cloud 1	490	10	Temperature ≈ 1 μK
3	Launch cloud 1	500	700	Velocity 3.4 m/s
4	Load cloud 2	600	500	10^9 atoms
5	Molasses cloud 2	1090	10	Temperature ≈ 1 μK
6	Launch cloud 2	1100	755	Velocity 3.7 m/s
7	Preparation and selection	1150	20	$\|F = 1\rangle$, $m_F = 0$ and $\Delta v_z \approx 4$ mm/s
8	Recapture cloud 1	1200	100	10^9 atoms
9	Molasses cloud 1	1290	10	Temperature ≈ 1 μK
10	Launch cloud 1	1300	345	Velocity 1.7 m/s
11	Preparation and selection	1350	20	$\|F = 1\rangle$, $m_F = 0$ and $\Delta v_z \approx 4$ mm/s
12	Interrogation (π pulse)	1470	10	Detuning > 2 GHz and Power > 500 mW
13	Detection cloud 1	1600	2	Light sheet - fluorescence
14	Detection cloud 2	1800	2	Light sheet - fluorescence

Table 3.1: Design goals: specified timings and parameters for gradiometry sequence consisting of two clouds with a juggling scheme. Exact timings will need to be experimentally optimised.

established this ampoule was broken inside a bellow and rubidium flux to the remainder of the vacuum is controlled through a valve. The bellows containing the rubidium is connected via the valve to the 2D chamber which has five indium-sealed windows for optical access. 2D and 3D chambers are connected by a CF16 nipple with a carbon inset to collimate the atom flux from 2D to 3D. From the 3D chamber are connections to the interrogation region and the valve used for rough pumping. There are a total of 7 indium-sealed windows on the 3D chamber with the lower Raman window at a slight angle to minimise light reflection from normal incidence. The interrogation region consists of two cubes, each with four large, indium-sealed windows and connected together by a 50 cm tube.

Pumping in the vacuum system is achieved with a small ion pump as well as a NEG in order to achieve and maintain low pressures. The small ion pump connected to the 2D chamber has a 2 l/s pumping rate (Gamma Vacuum) and was selected in order to minimise the overall size and weight of the system. The NEG on the opposite side of the experiment (SAES NEXTorr D100-5) has a pumping rate of 100 l/s. Again this particular NEG was selected due to the small size, weight and magnetic field it generates as compared to others in its class. The combination of pumping speed between the ion pump and NEG provides a differential pumping region across our chamber. This aids the flux of rubidium towards the 3D MOT by allowing a high vapour pressure 2D MOT whilst maintaining a low background pressure 3D MOT to minimise collisions during the measurement sequence.

At the low pressures achieved by these pumps ($\sim 10^{-11}$ mbar) the atoms are in a free flow regime. That is to say, the mean free path of the atoms is larger than the size of the vacuum chamber. Under such a regime

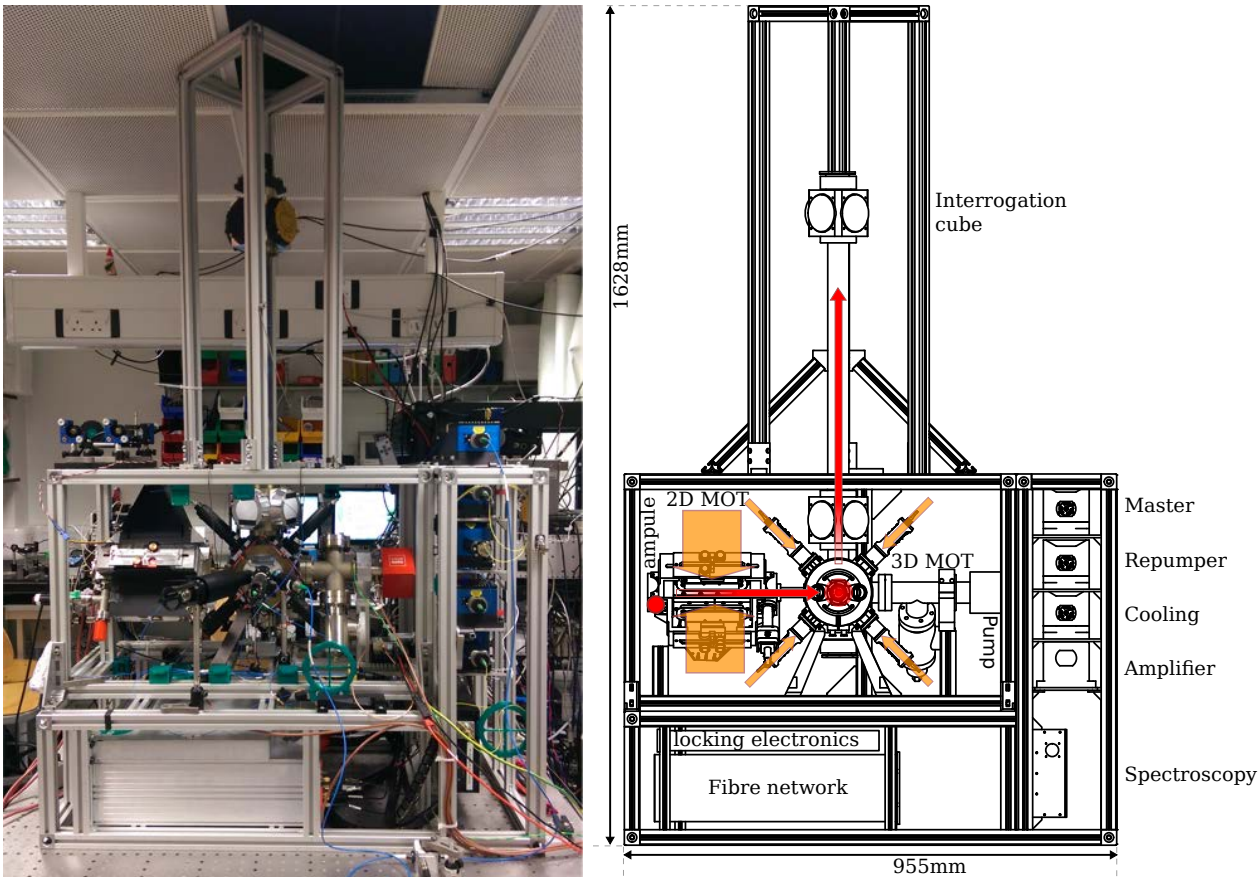

Figure 3.2: Sketch of physics package showing the full vacuum system, optomechanics and light source mounted on the same unit. The total size is $955 \times 500 \times 1628$ mm^3.

the atoms can only move in straight lines as there are no collisions to divert their path. This means that the atoms preferentially pass from the 2D chamber to the 3D chamber as there is a direct line-of-sight between the two. Between the two trap chambers is a narrow nipple with a carbon tube inset. This collimates the atom "beam" further to increase the likelihood of the atoms being trapped by the 3D chamber.

3.3 Lasers for Atom Trapping

3.3.1 Optical Components

As this experiment aimed to push more towards application than fundamental science, it was decided to use readily available commercial lasers to provide light needed for atom trapping. The system involves three, fibre-coupled New Focus Vortex 6900 lasers - hereafter referred to as master, cooler and repumper and a New Focus TA 7600 tapered amplifier to amplify the cooler.

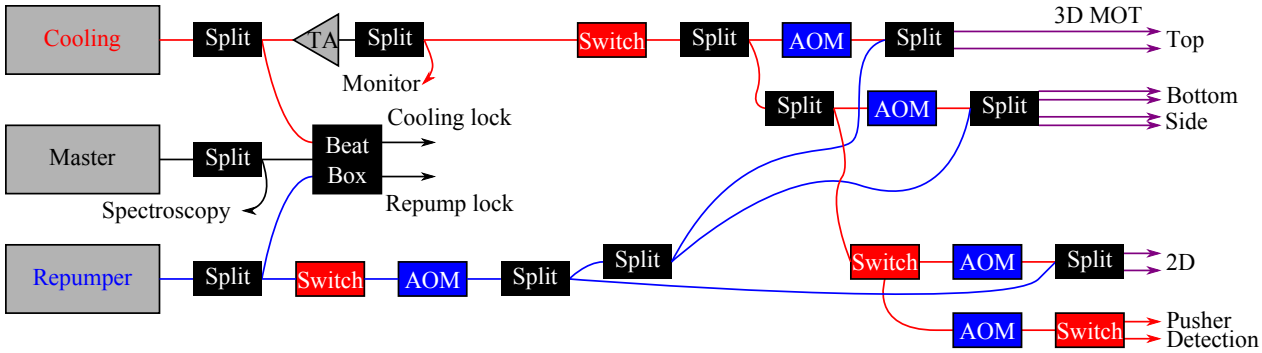

Figure 3.3: Fibre network used to control and distribute light to various parts of experiment and provide locking. Switches are used for redirecting or slow but complete extinction of light. AOMs are used for frequency shifting, fine frequency control and rapid attenuation of intensity.

Fig. 3.3 gives an outline of the fibre components used to distribute light from the lasers to the experiment. More detail on this system will be given in a later chapter but it will be summarised here. To start, light from the master laser is split equally. Part of the light is directed towards a spectroscopy module where frequency-modulation (FM) spectroscopy is performed [63]. Using the error signal produced from the spectroscopy setup, the master laser is locked to the ^{85}Rb D_2 line. The other part of the master laser enters the "beat box" where it is evanescently coupled to $\sim 1\%$ of both the cooler and repumper. The two fibres exiting the beat box contain a beat between master & cooler and a beat between master & repumper respectively. The electronics to analyse these beat signals will be discussed in the following section.

The majority of cooler and repumper light ($\sim 99\%$) is fibre coupled into the bulk of the fibre distribution network. Here fibre splitters are used to obtain the desired ratios in laser powers for every exiting beam and to mix the repumper and cooler before being passed to the MOT. Fibre AOMs are used for fine frequency control (for atom launch specified in Tab. 3.1) and fast attenuation of light by zeroing the RF driving power. Fibre switches are used for complete extinction of light.

The entire fibre network fits inside a 3U 19-inch rack box with outputs heading to the relevant MOT telescopes as illustrated in Fig. 3.4. Such a system enhances the portability of the experiment considerably.

3.3.2 Electronic Components

The beat signals of master & cooler and master & repumper are passed to offset locking electronics such that the cooler and repumper can be locked at defined frequencies away from the master frequency which is locked to an absolute reference. This allows for the cooler and repumper to be tuned independent of each other and the absolute frequency.

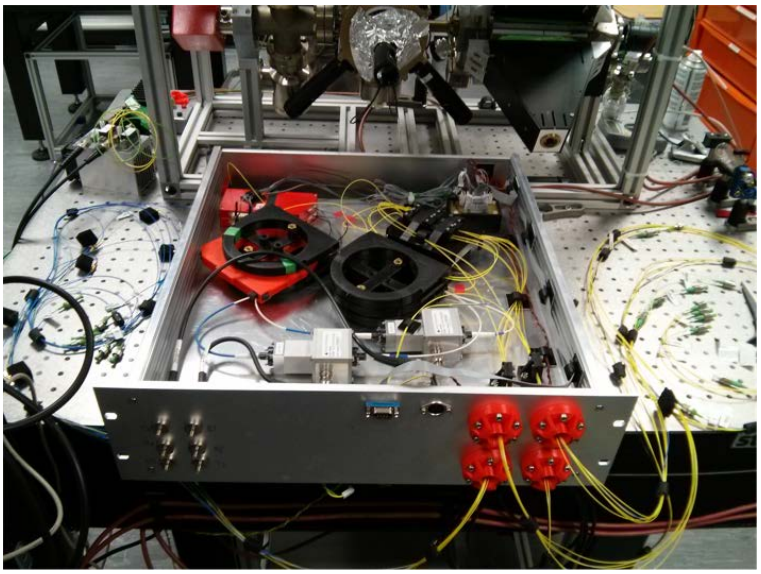

Figure 3.4: Packaged fibre network. The fibre network outlined in Fig. 3.3 fits completely in this 3U height 19-inch rack box. The front panel has inputs for AOM RF signals as well as TTL signals to drive the fibre switches.

Fig. 3.5 shows the electronics used to provide the offset locks for cooler and repumper. The beat signals of both are detected on fast photodiodes and mixed with a stable oscillator frequency of the desired offset. Passing the mixed signal through a comparator circuit - a comparator plus bandpass filter which returns a positive signal when below the cutoff frequency and negative signal when above - leads to an error signal that can be used for locking. Once locked, the tunability of the oscillators allow the locked frequencies to be moved by several hundred MHz with a resolution of 0.1 MHz for fine tuning.

3.4 2D MOT

The purpose of having a 2D MOT as well as 3D MOT is to achieve much higher loading rates of atoms into the 3D MOT than is typically obtainable with loading from a background gas of atoms. This is made possible by using the 2D MOT to pre-cool the atoms in two dimensions and create a stream of atoms moving sufficiently slowly towards the trapping region of the 3D MOT that they are captured easily. A fast capture rate is essential for the juggling scheme intended for measuring gravity gradients. The design of 2D MOT used here was inspired by the work done in [64, 65].

A single piece of titanium was machined to make the main body of the 2D MOT chamber. The windows of the 2D MOT are indium sealed which has the double benefit of improving optical access and allowing the coils to be mounted as close as possible to the chamber. Mounting the coils close allows the overall size and

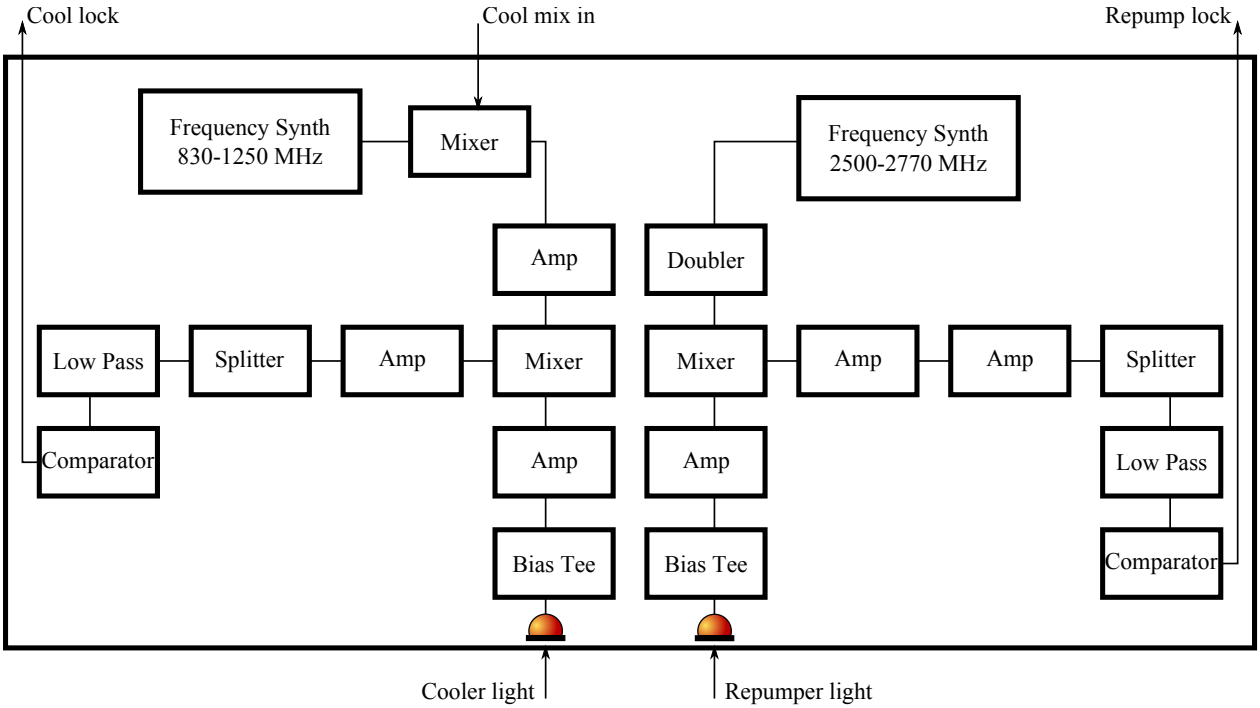

Figure 3.5: Electronics used for locking the Cooling and Repumper lasers. Cooling and Repump light which has been beaten against the Master is input into the electronics where it is mixed with a reference oscillator and an error signal produced. The cooling and repumping error signals are offset from the master reference by ~ 1.2 GHz and 5.5 GHz respectively.

required current needed to achieve the necessary field gradient to be reduced.

To create the magnetic potential we use four sets of coils, each with 45 loops of 1 mm copper wire. Simulations suggest that this should give a magnetic field gradient of 17 Gauss/cm at the centre of the trap for a current of 1 A. On opposite sides of the chamber the coils have currents flowing in opposite directions, as shown in Fig. 3.6 to create a zero in magnetic field at the centre of the chamber for that axis.

By connecting the 4 coils to 3 different power supplies one can fully control the magnetic field gradient in any direction. This allows for the magnetic centre to be optimised and effectively allows one to "steer" the atoms towards the 3D MOT.

Two fibre-coupled telescopes are used supply light to the 2D MOT. Each telescope contains a negative cylindrical lens, effective focal length -3.9 mm at 5.5 mm from the fibre input and the second a spherical lens of effective focal length 150 mm at 118 mm from the first lens. This combination of lenses produces a collimated, elliptical beam of light which is retroreflected on the other side of the chamber by an adjustable mirror. A more compact method was suggested in [66] but it was elected not to use this setup on the basis that it required more optical components which may have introduced additional complications.

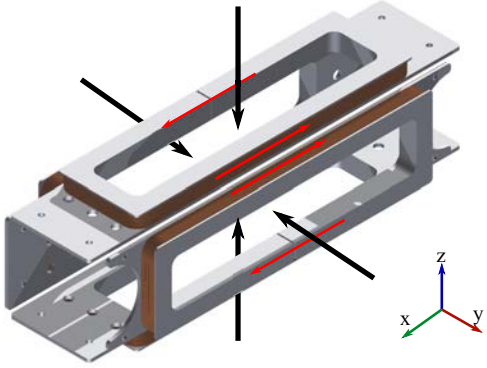

Figure 3.6: Magnetic trapping from 2D MOT coils. Black arrows show the direction of restriction resulting in a "cigar" shaped trap with atoms free to move along the x-axis. Red arrows show the direction of current flow, the direction is reversed for the opposite coil in the pair.

A pushing beam is not currently mounted onto the 2D MOT chamber as the aim was to rely on the angle of the telescopes imparting some horizontal momentum to the atoms and push them towards the 3D MOT. Alternatively there is a window situated at the end of the 2D MOT chamber which allows for a pushing beam towards the 3D MOT. Shown in Fig. 3.7 is a render of the assembled 2D MOT subsystem.

Using the information outlined in Appendix. B.2 the flux of atoms flowing out of the 2D MOT depends on background pressure, size of the trapping region, light field detuning and intensity, and magnetic gradient.

Background pressure presents a trade-off optimisation where a higher pressure results in a higher loading rate into the trap but also a decrease in atomic flux due to collisional loss. As the loading is from a vapour cell there is very limited control over this parameter through a valve. One could envision a temperature control system on the the rubidium bellow to moderate the rubidium pressure in the trapping region. The size of the trapping region has a similar optimisation - radially larger trapping beams increase the capture velocity and more atoms can be captured for a fixed detuning and magnetic gradient. This will not necessarily increase the flux towards the 3D MOT if the trapping diameter is much bigger than the hole to the 3D MOT. Longitudinally larger trapping beams allows for hotter atoms to be sufficiently cooled by increasing the length over which cooling can operate and thus increasing the flux. However, making the trap too long has negative implications as it results in the atoms cooled furthest from the 3D MOT being lost to collisions. Higher intensity trap beams for a fixed detuning and magnetic gradient should result in more efficient cooling and hence an increase in flux.

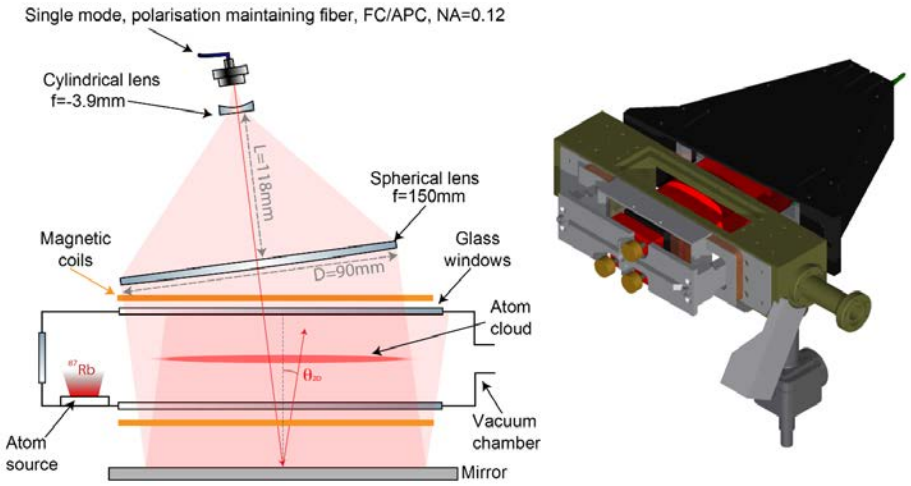

Figure 3.7: 2D MOT utilising large, retroreflected elliptical beams to pre-cool Rubidium atoms in two dimensions. A small angle of $\sim 4^\circ$ is imparted to the telescope such that the light has a small parallel momentum component to the direction of atom flux. Rubidium source is an ampoule.

3.5 3D MOT

The windows on the 3D MOT are again indium sealed. There is one special window mounted at the base of the 3D MOT chamber specifically for Raman light. This window is thicker than average (20 mm) to minimise vacuum deformation and optically flat ($\lambda/20$ specified) to mitigate wavefront distortion. To minimise reflections this window is sealed at a slight angle from normal incidence.

To deliver light to the atoms there are six telescopes positioned in orthogonal axes around the chamber. The telescopes contain lenses for collimating the light out of a fibre to a beam with diameter 20 mm as well as a polariser and quarter waveplate for controlling the polarisation. A six beam setup was chosen over a three-beam retroreflection system as there is a requirement for the atoms to be launched upwards. This is simplified if one has individual control over the upward and downward propagating MOT beams. Fig. 3.8 shows the 3D MOT subsystem when assembled.

Pre-cooled atoms from the 2D MOT are trapped in the 3D MOT chamber. To trap atoms in this region a pair of coils in anti-Helmholtz configuration are used, creating a quadrupole field with the zero-point at the centre of the chamber. The coils were chosen to be compact and close to the chamber so as to keep the size and weight of the experiment to a minimum and to reduce the amount of heat dissipated by the coils. Each coil has 357 loops of copper wire and allows for $\sim$ 10 Gauss/cm field gradient near the centre of the trap when supplied with 1 A current.

Based on typical detunings of $\delta = 2\Gamma$ and the magnetic field gradient mentioned above, a capture velocity

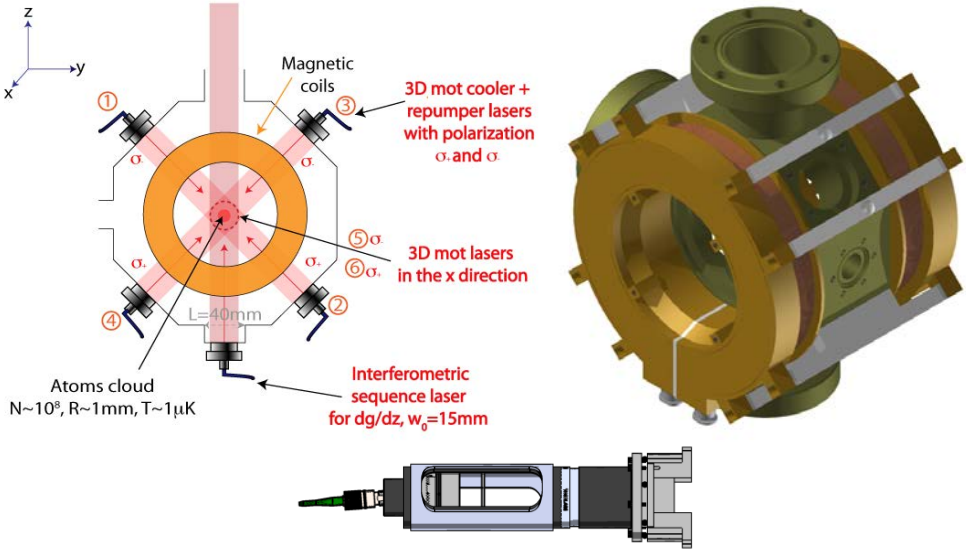

Figure 3.8: Top: 3D MOT consisting of anti-Helmholtz coil pair and 6-beam cross for atomic cooling and trapping. Bottom: telescope designed to collimate and circularly polarise light exiting the fibre into a beam of 20 mm diameter.

can be estimated as $v_c \approx 10$ ms^{-1} (Appendix. B.1). From [67], the mean velocity of atoms from a 2D MOT is on the order of 30 ms^{-1} and so one might expect only a fraction of the atoms will be captured by the 3D MOT.

3.6 Interferometry Region and Interrogation Cubes

This section of the experiment is where launched atoms perform their parabolic flight. Once the atoms have been trapped and cooled in the 3D MOT to $\sim$ few μK, they are launched upwards by altering the frequency difference between the upward and downward propagating trapping beams. The total height of the two cubes and tube is 70 cm, with the cubes being 10 cm each and the tube being 50 cm. Hence the time for the atoms to make a parabolic flight and return to the trap is in the region of 800 ms.

The interrogation cubes have windows on four sides and will serve multiple purposes at different points of the experiment. Firstly the windows can be used for detection of the clouds following the interferometry sequence. This requires a telescope and imaging device to be mounted on the side of the cube and laser light injection mounted on the opposite or perpendicular side depending on whether absorption or fluorescence detection is preferred. The second function of these windows will present itself once a second experimental setup exists. Once this is realised the windows can be used to interrogate both experiments simultaneously with a single Raman laser in the horizontal direction, performing a gravity gradient survey in the x/y-

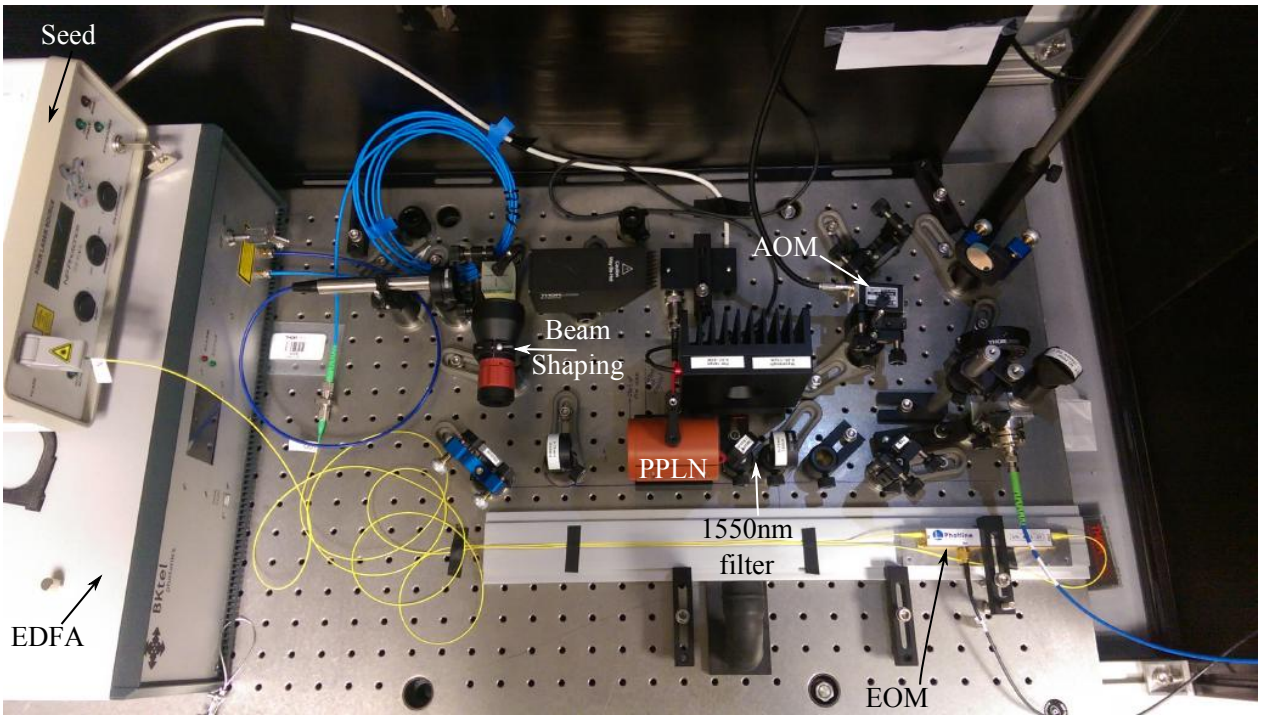

Figure 3.9: 1560 nm laser system consisting of seed, EOM, EDFA, PPLN, AOM and fibre coupler. Light from the seed laser is modulated by an EOM driven by a stable 6.834 GHz microwave source to generate the second frequency needed for Raman transitions. The modulated light is amplified up to a maximum of 20 W before undergoing second-harmonic generation. The frequency doubled light passes through an AOM which is used as a fast shutter before being coupled into a fibre and delivered to the experiment.

direction.

The window situated at the top of the upper cube is a specially thick, optically flat window mounted at a small angle identical to the one in the 3D MOT region. Both of these windows were chosen with the intent to minimise wavefront distortion on the Raman laser beam used to interrogate the atoms. Work done by [62] highlighted that once most experimental systematics are well controlled, wavefront distortion can start to limit sensitivity. The worst contributor to the distortion is the window which is double-passed by the Raman light. We intended to test the difference between locating the retroreflection mirror above and below the experiment and for this reason we have high quality windows at both the top and bottom of the vacuum system.

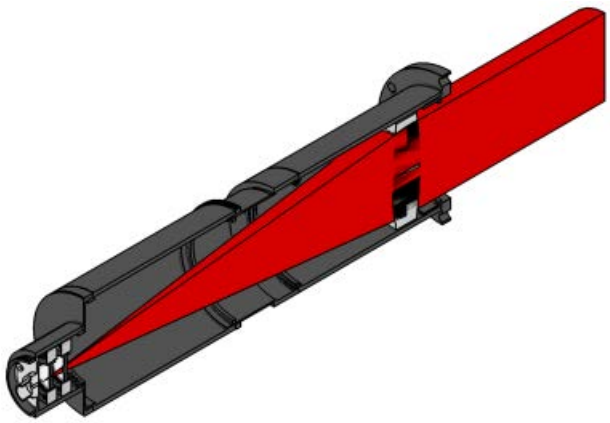

Figure 3.10: Telescope for delivering Raman light to atoms. A bulkhead fibre adapter allows the light from the fibre to freely expand through a polariser and quarter waveplate used to fix the polarisation. A 200 mm plano-concave lens is placed at its focal distance from the fibre to create a parallel beam. A minimum number of components was used to minimise wavefront distortions.

3.7 Raman Laser

3.7.1 Optical Components

Fig. 3.9 shows the laser system used to generate Raman light for interrogating atoms in this interferometer. An NP Photonics 1560 nm laser is used as the seed with 20 mW output power. It has a narrow linewidth $\lesssim$ 1 kHz to minimise the phase difference accumulated during retroreflection delay [5]. The output of the seed is phase modulated by a 10 GHz Photline EOM which is driven by a stable 6.834 GHz microwave source (Fig. 3.11) to generate frequency sidebands - removing the need for complicated phase lock loops which are usually used to address the problems in Sec. 2.5.1. The light intensity is amplified up to 20 W using a BKtel EDFA. The amplified field is passed through a 40 mm PPLN crystal temperature stabilised to $\sim$ 180 °C and gives $\sim$ 25% power conversion efficiency from 1560 nm to 780 nm. A free space AOM is included before fibre coupling optics as a fast shutter. Finally, a fibre transports the light from the optical bench to experiment where it is polarised and collimated by the telescope shown in Fig. 3.10. It is possible to deliver over 1 W of 780 nm light to the atoms using this setup but more could be achieved with greater care in alignment. The benefit of having large power is that the Raman beam can be made large in diameter whilst maintaining high intensity. This allows one to have a flat intensity profile over the whole atom cloud, reducing noise from intensity related Rabi frequencies.

The telescope consists of a polariser aligned to the fibre key to correct for and minimise any polarisation fluctuations in the fibre, a quarter waveplate (optional) aligned to the polariser to generate circularly polarised light for velocity insensitive interferometry and a 200 mm focal length lens to give a collimated beam with 20

mm waist. The number of optical components is kept to a minimum in order to reduce wavefront distortions as per Sec. 2.5.1. All windows and mirrors in the Raman beam path (see Fig. 2.8) are specified to $\lambda/20$ surface flatness and are made from extra thick glass to minimise vacuum bending. The retroreflection mirror mounted on a tip-tilt stage at the base of the 3D MOT has a similar specification.

High optical power affords one the luxury of increasing the Raman single-photon detuning further from resonance to reduce the effect of spontaneous emission. At the highest recorded intensity of 132 mW/cm^2 we can detune by several GHz (from theory of App. A.3).

For velocity sensitive gravity measurements, a $lin\perp lin$ polarisation configuration is used as $\sigma^+\sigma^-$ drives dipole allowed transitions, where, for angular momentum to be conserved, $\Delta m_F = 0$ for the Raman transition regardless of the quantisation axis, but the different coupling strengths lead to different light shifts for different m_F [68]. With $lin\perp lin$, which can be thought of as superpositions of σ^+ and σ^-, the two $\Delta m_F = 0$ components add constructively and the m_F dependence of the light shift disappears.

Due to the light shift, the Raman coupling strength depends on the intensity at the atom's position in the laser beam. This type of inhomogeneity leads to systematic errors. One avoids part of this by removing the m_F dependence of the light shift.

3.7.2 Electronic Components

During the interferometer sequence, the frequency difference of the Raman beam components must be continuously ramped to compensate for the Doppler shift induced on the atoms by gravitational acceleration such that the 6.834 GHz frequency difference is kept constant.

The scheme for generating the different Raman frequencies in this experiment involves using an EOM to generate a sideband at 6.834 GHz from the carrier rather than using two phase-locked lasers. This means that only one ramp on the microwave signal driving the EOM is necessary. A stable microwave oscillator developed by SYRTE for the iSense project [69] is used here and is shown in Fig. 3.11. Any fluctuations in the frequency difference directly couple into phase noise as discussed in Sec. 2.5.1.

The input oscillator mentioned in Fig.3.11 is a Novatech DDS8p which has a range of 100 Hz to 120 MHz in steps of 1 μHz by using 48 digital bits and phase control with 14 digital bits. Changes to frequency or phase take on the order of 600 ns.

As the maximum output of 120 MHz is less than the 166 MHz needed to mix down from the 7 GHz provided by the oscillator, it is required to mix one of the stable 100 MHz outputs of the microwave reference with ~ 66 MHz from the DDS. The two signals are combined on a Minicircuits ZX05-1L-S+ frequency mixer

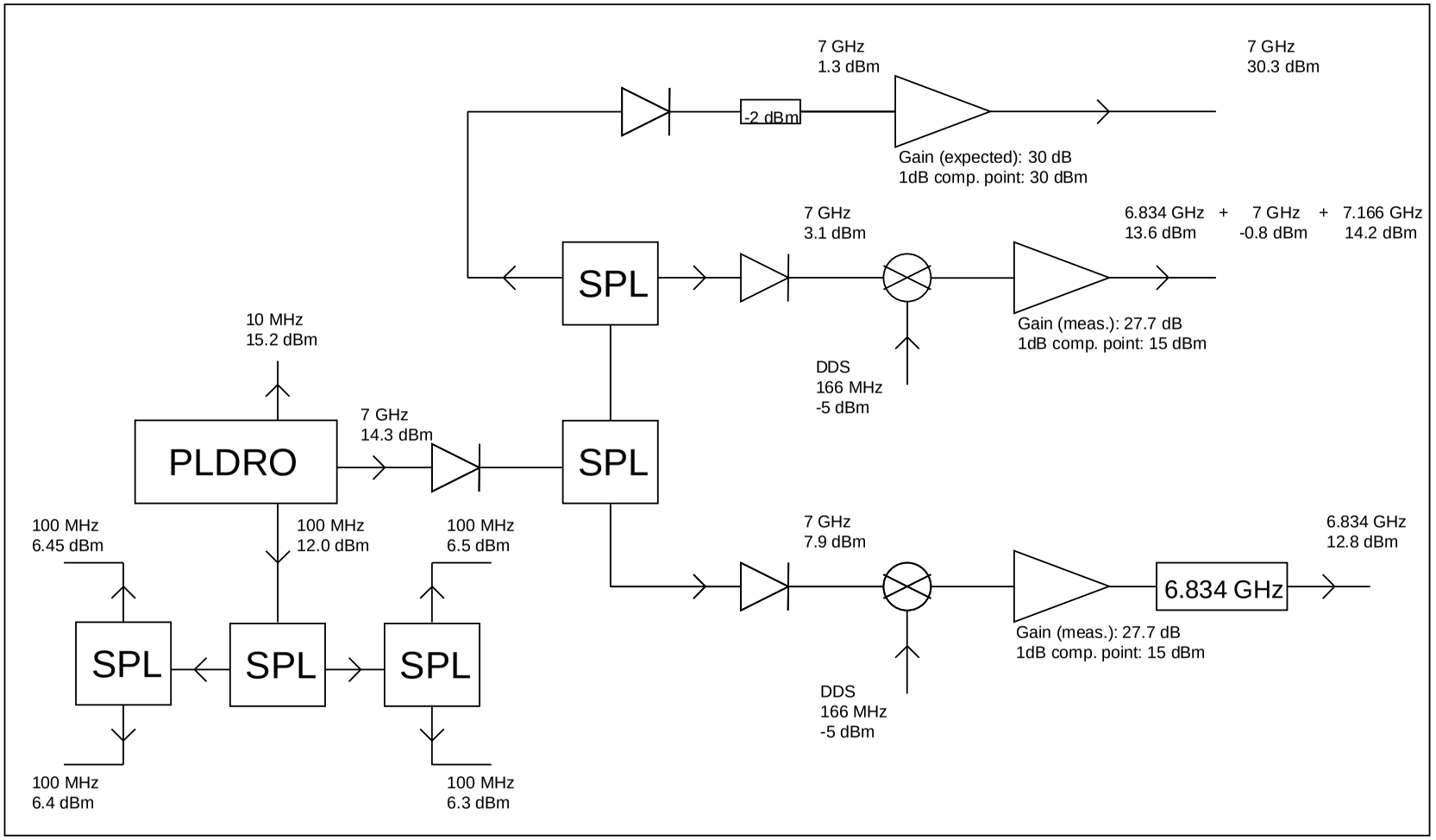

Figure 3.11: Microwave reference chain for generation of 6.834 GHz Raman sidebands. A controllable input oscillator of ∼166 MHz is mixed with the stable 7 GHz oscillator and a bandpass filter is used so that only the difference frequency is output.

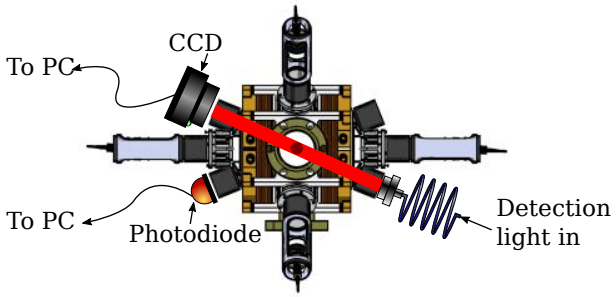

Figure 3.12: Top-down view of the 3D MOT chamber and detection components. A collimated fibre input creates a 10 mm diameter beam to illuminate the atoms which can be simultaneously detected via fluorescence with a photodiode and absorption with a CCD camera.

and filtered through a VHF-145+ high-pass to remove the difference component. The frequency ramp is realised using digital output channels of the control FPGA directly connected to the digital frequency pins of the DDS.

Phase between the DDS and microwave oscillator must be controlled using the DDS to ensure proper mixing. Any phase noise on the signal will result in fluctuating microwave power driving the EOM and hence a different carrier/sideband ratio. This will introduce phase noise on the atoms during the Raman sequence. Again the phase of the DDS is controlled using digital output pins from the control FPGA. In addition to controlling the phase stability, it is also necessary to be able to change the phase for the last $\pi/2$ pulse in the Raman sequence in order to scan interference fringes.

3.8 Detection System

MOT Detection

For initial measurements of MOT, molasses, Rabi and Ramsey fringes the detection was done inside the 3D MOT chamber. Telescopes and cameras were placed around the 3D MOT for absorption and fluorescence imaging as shown in Fig. 3.12

A collimated beam of waist 10 mm tuned to atomic resonance illuminates the atoms. A 35 mm focal length lens collects light onto the photodiode (Thorlabs DET36A) with a fractional solid angle of 0.033. An adjustable lens system infront of the CCD camera (Imaging Source DMK42BUC03) is used to image the entire cloud onto the 8 mm chip. This allows us to calibrate atom number as a function of photocurrent which is useful for rapid diagnostics.

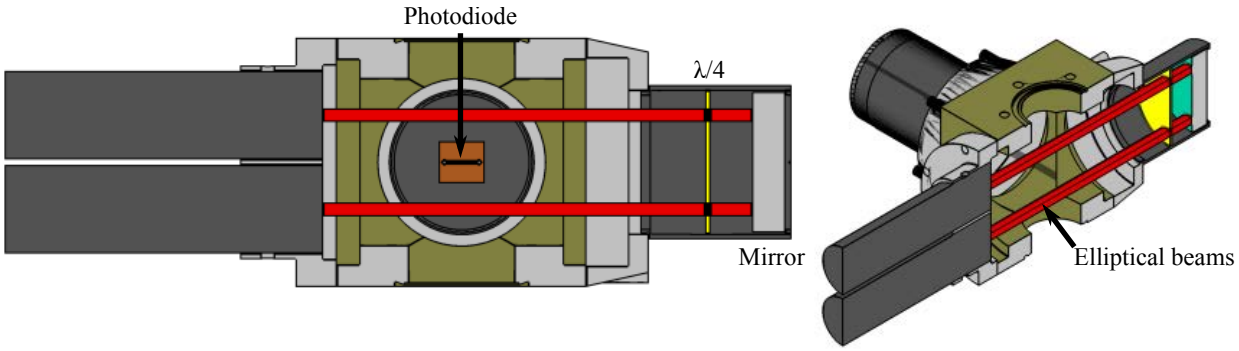

Figure 3.13: Light sheets for fluorescence detection of atomic states following interrogation with Raman beams. The first sheet the atoms encounter contains light resonant with the detection frequency and is partially retroreflected such that atoms in the $|F = 2\rangle$ are detected and then pushed out of the detection region. The remaining $|F = 1\rangle$ fall to the totally reflected second light sheet where they are repumped and detected. Light from the atoms is collected by 50.8 mm lens and focused onto a photodiode.

Cube Detection

At the time of writing this thesis the detection system for launched atoms is still being iterated. The first implementation is based on the setup of [38, 67] using two "rectangular" light sheets and fluorescence detection.

The working principle here is that the first beam the atoms encounter as they fall downwards is tuned to the cycling $|F = 2\rangle \rightarrow |F = 3\rangle$ (cooling without detuning) transition so that atoms in the $|F = 2\rangle$ state following Raman interrogation are detected. Only the top half of this beam is retroreflected which causes the $|F = 2\rangle$ atoms to be pushed away once they have been detected. The remaining atoms in the $|F = 1\rangle$ state pass to the second beam which contains both the cycling frequency and repump frequency light. Repumping light transfers the $|F = 1\rangle$ atoms to $|F = 2\rangle$ whilst the cycling again detects $|F = 2\rangle$. The entire beam is retroreflected to not push away any atoms and ensure all are detected. One then has a measure of the number of atoms in $|F = 2\rangle$ and $|F = 1\rangle$.

This detection scheme is not without problems which prompts new designs to be considered. The first problem arises due to imperfect blowaway in the first detection beam. Another issue is that there is a finite probability of atoms in the first detection beam de-exciting to $|F = 1\rangle$ and being detected by the second beam. Additionally, due to the nature of fluorescence detection there is no spatial information about the cloud and the detection itself is sensitive to intensity noise. Finally, the two states are detected at different times which can introduce other sources of technical noise. It would therefore be preferable to switch to absorption detection and/or employ simultaneous imaging of both states.

One way to realise simultaneous detection is outlined in [70]. Using light induced forces from the Raman

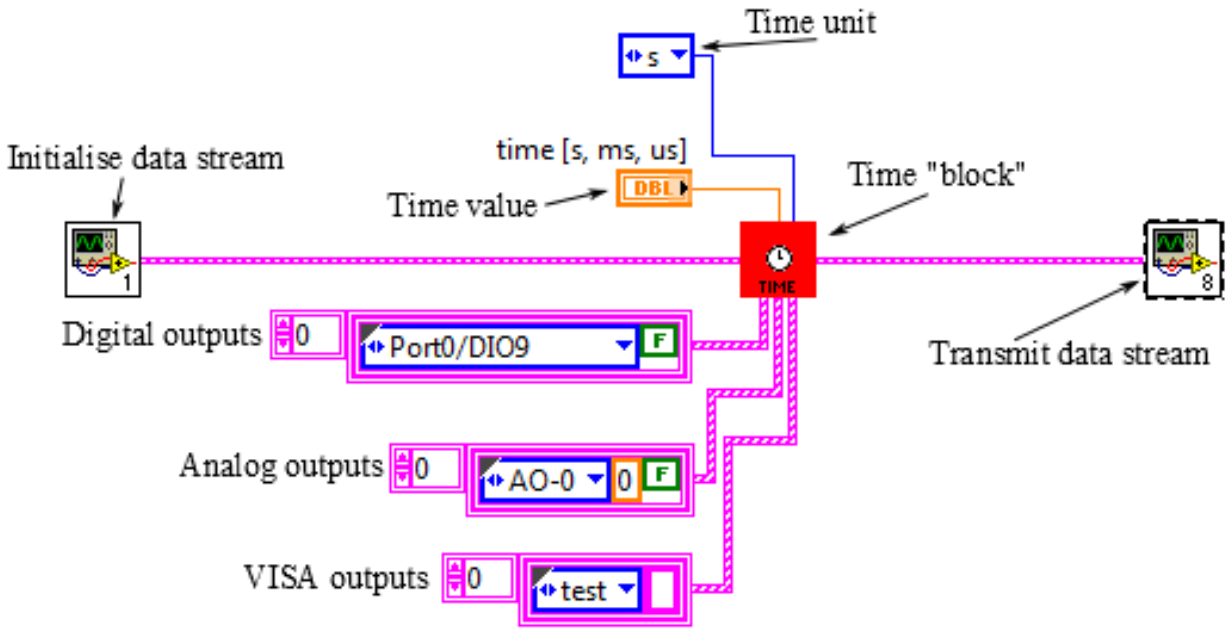

Figure 3.14: Basic coding block for computer control. "Initialise data stream" prepares the data structure used to write to the FPGA hardware. "Time blocks" are user commands thats are executed for a defined time and can contain digital, analog and VISA controls. To write a sequence of insrtuctions one chains many of these blocks together. "Transmit data stream" writes the "Time blocks" to the FPGA hardware.

beams one can physically separate the $|F = 1\rangle$ and $|F = 2\rangle$ states and then detect them with a common light beam. This gives common-mode suppression of the laser intensity and frequency noise [71].

3.9 Computer Control

The computer control for this experiment is based on a National Instruments sbRIO-9632 FPGA, controllable with LabVIEW. Much of the backend programming was done by [72] and the basic operating procedure will be summarised here.

Fig. 3.14 shows a typical but very simple program on the host computer that one would use for controlling the experiment. The idea is that all of the data structures are created and initialised by the first sub-program. These data structures can then be modified by assigning values to them for certain lengths of time which is handled by the "time block". Here one sets the duration and values of everything that one wishes to change and a program consists of chaining several of these together. Finally the chain of time blocks are sent to another sub-program which converts the data into a memory array which can be understood and read-out by the the FPGA. The FPGA will interpret the sequence and continue to loop the same sequence until a

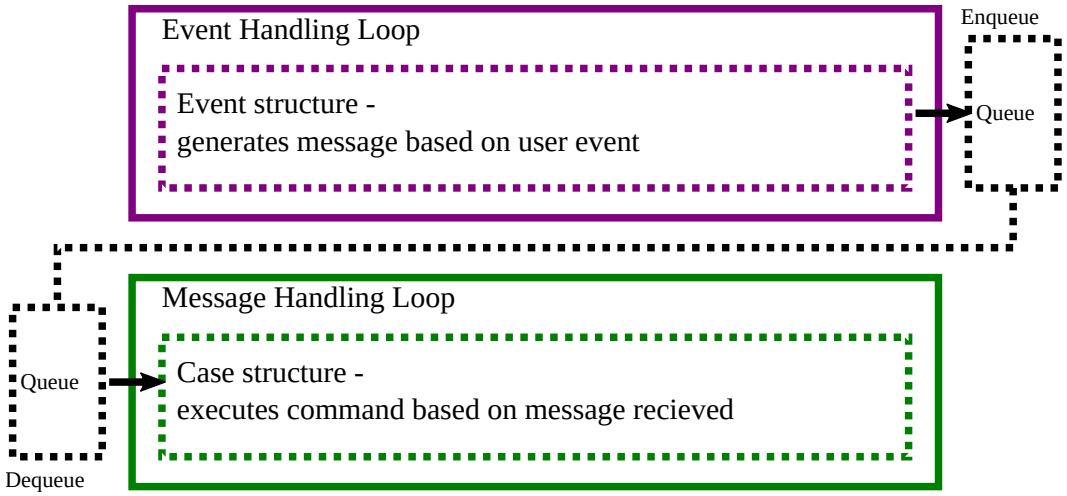

Figure 3.15: Queued Message Handler (QMH) logic loop. Two loops run in parallel to handle user input and the system response. Any input from the user is handled by the first loop and generates a message which is added to a queue. The second loop empties the queue in the order it recieves messages and completes the associated tasks.

new one is given.

The combination of LabVIEW and FPGA interacts with most hardware in the experiment. It provides frequency and amplitude instructions to the DDSs which control all of the AOMs. It provides TTL signals to fibre switches, IGBTs for magnetic field switching and RF switching.

There are problems with the current control which are currently being addressed. The FPGA is underclocked to 10 MHz which limits timing resolution to 100 ns because the code is not efficient and occupies too much FPGA memory to run at maximum speed. The nature of a looping program means that the time at which a new sequence starts is not deterministic. For this second point, a new method, such as a queued message handler (QMH), for executing code is desirable. This would allow one to trigger sequences at defined times based on certain criteria being fulfilled.

Fig. 3.15 outlines the logic of QMH architecture. The system consists of two loops, the first of which responds to user input and the second handles data processing. Upon receiving a command from the user, an event is triggered in the first loop which produces a message to be added to a queue. The second loop, running in parallel, is constantly checking the queue for messages to process. As soon as a message is discovered, the second loop executes the corresponding commands and removes the item from the queue.

This method of programming has benefits in LabVIEW as a whole where it is trivially easy to crash the GUI with user input if the backend is not robustly programmed. It has the added benefit of allowing one to update the experimental sequence being executed by the FPGA more deterministically by adding a new sequence to the queue.

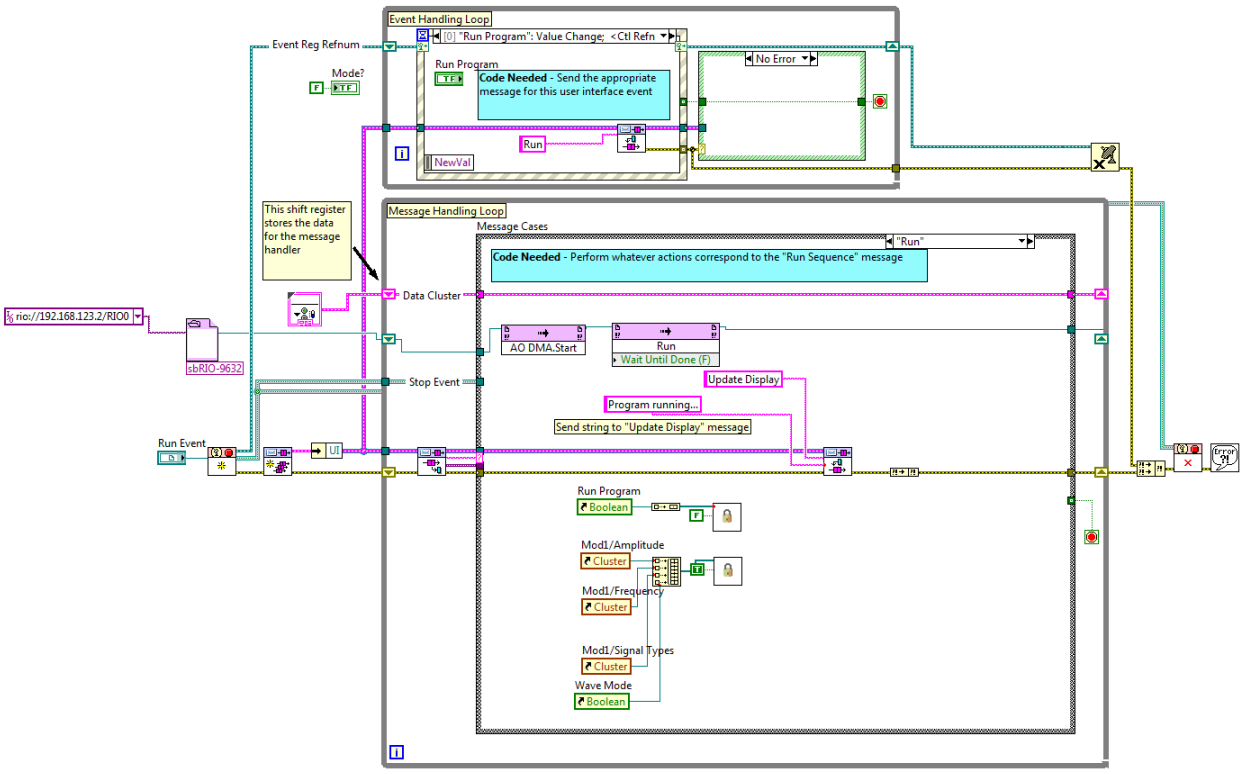

Figure 3.16: LabVIEW interpretation of the logic outlined in Fig. 3.15 [73].

3.10 Magnetic Field Control

For the 3D trapping region it is important to compensate the effect of the Earth's magnetic field for sub-Doppler cooling. Sub-Doppler cooling is realised by ramping the intensity and frequency of the trapping light in the absence of magnetic trapping potential. Therefore, any residual fields will give rise to a position dependent force that moves the atoms out of cooling beams. To counter this effect a set of three pairs of Helmholtz fields in an orthogonal configuration is used to provide a magnetic field equal but opposite to residual fields.

For interferometry, as discussed in Sec. 2.6.2, a small magnetic perturbation gives rise to a similar order of magnitude phase shift to that of gravity gradients. In order to suppress this effect it is desirable to shield the atoms from external magnetic perturbations.

Much of the research on magnetic shielding has been completed by another student but the conclusion was that reducing the effect of external fields by a factor of 1000 should suppress the phase noise enough to get a precise measurement of gravity gradients. An idea for shielding to achieve this is presented in Fig. 3.17. Here the tube where the atoms are interrogated is the most well shielded region as this is where perturbations

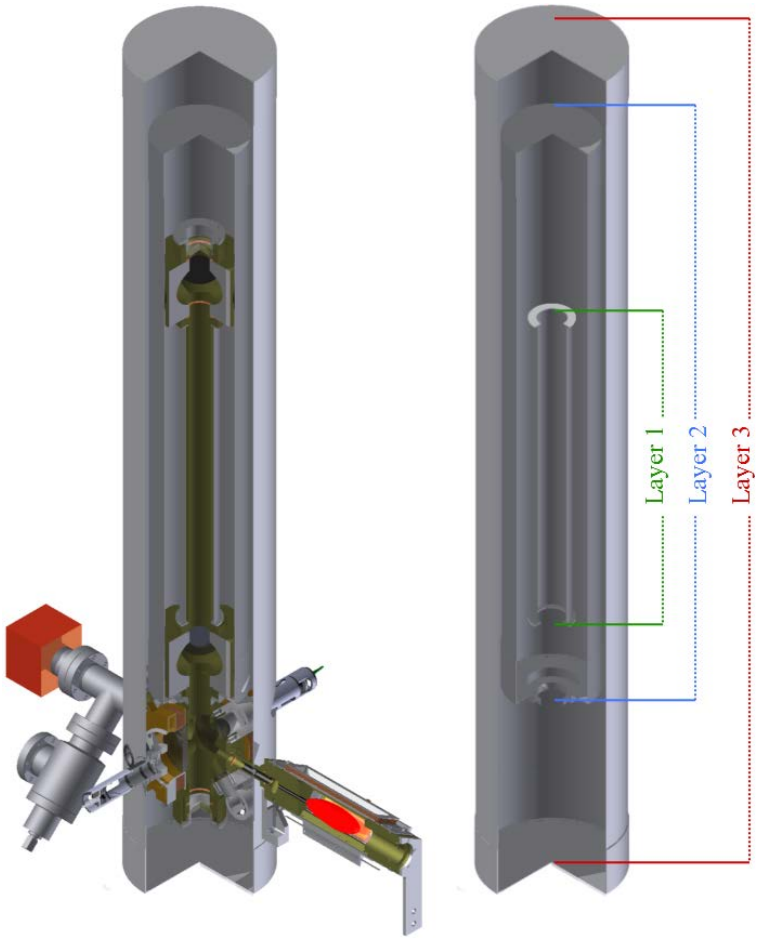

Figure 3.17: Author's impression of the design for three-layers of magnetic shielding constructed from Mu-Metal cylinders. The goal is to create maximal shielding over the entire interferometer region of the vertical tube. A shielding factor of 1000 should be very achievable with a three-layer design.

will cause the largest phase shifts. The outer two shields cover more of the experiment to provide shielding to both the inner tube and other parts of the experiment.

Inside the innermost shield will be a solenoid shaped bias field for the interferometry region. This will provide the necessary quantisation axis for velocity selection and Raman transitions and is important that this remains clean and unaffected by external fields.

CHAPTER 4

PRELIMINARY RESULTS

This chapter presents the results of the GGtop experiment in its current state. At the time of writing this thesis the experiment has developed to the stage where Rabi oscillations and Ramsey fringes have been observed and atoms have been successfully launched.

To start, parameters including loading rates, atom number and temperature for the 2D and 3D MOTs will be presented. An investigation into the optimal cooling during the molasses stage and the velocity tuning of the atomic launch are included. Finally the Rabi and Ramsey data achieved with the Raman laser system will be discussed in detail as there are several optimisations that must be done to improve this data.

4.1 Atom Trapping

4.1.1 2D-MOT loading of 3D-MOT

The purpose of the 2D MOT is to enhance the loading rate of the 3D MOT such that a juggling scheme can be realised for gradient measurements. In an ideal case, loading rates on the order of 10^{10} atoms/s would allow for 10^9 atoms to be loaded into the 3D MOT with a few hundred ms loading time. Below this an insufficient number of atoms are loaded into the 3D MOT and the signal to noise ratio of the interferometer suffers.

To test the loading rate from the 2D MOT, the intensity of the the 2D MOT light was varied and the number of atoms loaded in the 3D MOT was recorded via absorption imaging using the setup in Fig. 3.12 as a function of time. Each time measurement was an average of ten absorption images. For each intensity, a linear fit was applied to the linear region at the start of the atom number vs. time loading curve, which is a safe approximation for the short loading times we intend to use in the interferometry sequence, to extract the number of atoms captured per second.

By repeating measurements for several intensities as described above we found a maximum loading rate of $\sim 2.7 \times 10^7$ atoms/s at only half of the maximum 2D MOT laser power. Increasing the power of the beams further did nothing to increase the loading rate suggesting the flux was limited by something other than the intensity. This is considerably lower than the design specification in Tab. 3.1. The result was verified by studying the fluoresence signal of the loading curve (calibrated for a photodiode, see App. B.4) measured for the 3D MOT.

To explain this one must consider that the angle of the 2D MOT telescopes was not optimised due to mechanical constraints and no separate pushing beam was included. Based on the work done in [65], optimisation of the telescope angle should allow for this system to achieve the desired loading rate and work is being done to modify the mounting design. In the current state it would be required to include an additional pushing beam to achieve a higher loading rate but due to a failure in the light delivery design this was not implemented.

4.1.2 3D-MOT

Loading and Atom Number

Loading rates of the 3D MOT were already discussed in the previous section, they are repeated here in the context of the total number of atoms loaded into the trap. The loading rate, $\sim 2.7 \times 10^7$ atoms/s, stated

previously is for short loading times. At longer loading times the atom number in the MOT begins to saturate as the number of atoms captured per second equals the number of atoms lost per second as described by Eq. B.10. From experiment the MOT is essentially fully loaded after 5 s with a small increase noticeable if allowed to load for longer. The total number of atoms in the fully loaded trap is on the order of 1.2×10^8 (measured with absorption imaging as described in App. B.5). This number is on the low side and will limit interferometer signal to noise ratio in the future due to the loss of atoms associated with vertical velocity selection. It is difficult to increase the number of atoms in the 3D MOT by modifying the 3D MOT design as the trapping beams are at their maximum diameter, limited by 20 mm windows and intensity, limited by losses in the fibre network. The 2D MOT flux should be characterised to establish whether the limitation lies with the atom flux or the 3D MOT design.

Temperature

The temperature of the atoms is an extremely important quantity for a gravity gradiometer. When the atom cloud is launched and is in free flight it will expand due to thermal motion. If it expands too much then atoms will be lost to the walls of the chamber. It is therefore essential that the cloud is cold before being launched.

For a typical ^{87}Rb MOT, the temperature should be in the 10's of μK range, below the Doppler temperature of 146 μK [75] due to sub-Doppler cooling mechanisms [76]. The temperature of the MOT was measured for optimisation purposes but was found to be on the order of 1 mK. In this case we can't reliably assign a temperature to our cloud as the large value is due to non-thermal effects arising from poor beam balance and imperfect magnetic field compensation. Such "temperatures" are far too large for our fountain geometry as the expansion will be too great. Further cooling techniques which are necessary to reduce the temperature are described later in this chapter.

Position

Data for the central position of the 3D MOT were taken over a period of 40 minutes to assess the stability of the beam balance in the experiment. Fig. 4.1 shows the results of this particular measurement which revealed that the centre of the cloud drifts by ~ 5 and ~ 3 mm in the x and y directions respectively. This data highlights that there must be a significant drift in the intensity balance of the trapping beams which shifts the spatial location of the zero Doppler-force region. A shift of position of the cloud explains why it was difficult to optimise the magnetic field compensation to obtain realistic temperature measurements because the cloud was drifting to different regions of the magnetic field and experiencing different forces.

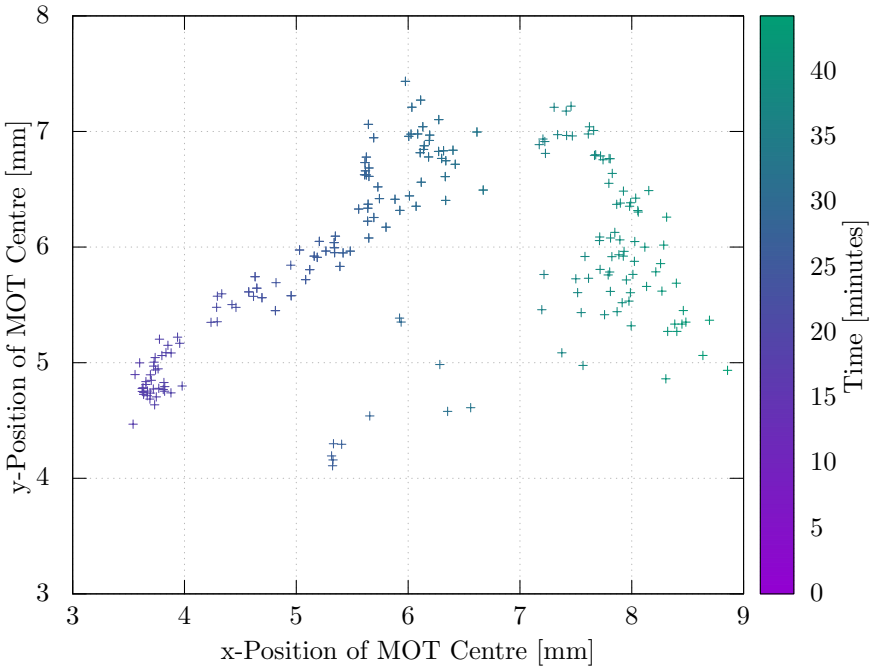

Figure 4.1: Position of cloud center in 3D MOT relative to the CCD camera used for absorption imaging. Points were measured with the absorption imaging system and recorded over a period of 40 minutes.

There is another issue associated with this measurement. Drift in the x direction is prohibitive for precision interferometry measurements as the interrogation sequence employs vertical laser beams which have a Gaussian intensity profile in the plane of the atoms and hence the spatial intensity profile seen between successive measurements is also drifting. In addition, if the beam balance is drifting then the launch angle of the cloud will be drifting resulting in additional Coriolis effects.

4.2 Atom Launch

To launch atoms is conceptually simple, one only needs to detune the trapping beams relative to each other. However, the temperature of the atoms following the MOT stage is high enough that the cloud will disperse rapidly while being launched and this is obviously problematic. To address this effect, an additional stage of cooling is employed before launching to reduce the cloud temperature further and limit the expansion. Parameters to be optimised for launching include:

- Alignment of trap beams
- Compensation coils for geomagnetic field

- Intensity and detuning of cooling light
- Duration of cooling stages
- Launch direction

4.2.1 Molasses Cooling

Following the MOT stage of the experiment, the magnetic fields are turned off for a short time and the atom cloud is held solely by the laser beams. This will be referred to as the molasses stage although other literature may use the term molasses differently. Theory shows that if during this stage one decreases the intensity of the light field and also increases the detuning further from resonance, the temperature of the cloud will decrease [77]. Decreasing the intensity to cool further can be explained as follows; there is a maximum area over which polarisation gradient cooling (Sisyphus cooling) is effective in the MOT, beyond which Doppler cooling dominates. As the field gradient decreases the area over which the polarisation gradient cooling is most effective increases and so more atoms reach a lower temperature [78, 79]. A similar argument can be made for frequency detuning because as the detuning increases, a larger range of velocities are cooled resulting in more cooled atoms.

The equilibrium temperature reached for polarisation gradient cooling in optical molasses can be approximated as $T_e \approx C\hbar\Omega^2/k_B|\delta|$ where C is a numerical constant ~ 0.1, $\Omega = 2\mathbf{d}.\mathbf{E}/\hbar$ is the Rabi frequency, δ is the laser detuning from resonance and k_B is Boltzmann's constant. At a given intensity, temperature is inversely proportional to detuning and at a given detuning is proportional to intensity through the Rabi frequency [77].

To investigate molasses temperature a time of flight (TOF) technique is used where the magnetic field and light of the 3D MOT are turned off and the cloud of atoms is allowed to expand for a variable amount of time before being imaged. We start by trapping a cloud of atoms for 5 s to get a decent atom number in the 10^8 range. We then simultaneously shut off the magnetic field and begin adjusting the light field via a digital trigger. After this short period of light field manipulation we turn off all fields and allow the cloud to expand in the dark for some predetermined amount of TOF. After the elapsed time we detect the atoms with an absorption imaging pulse followed by an image of the light field with no atoms present to suppress intensity noise.

By imaging the cloud for several different TOFs and understanding that thermal expansion has a Gaussian shape one can find the temperature of the cloud from the rate of the expansion using a Gaussian fit to

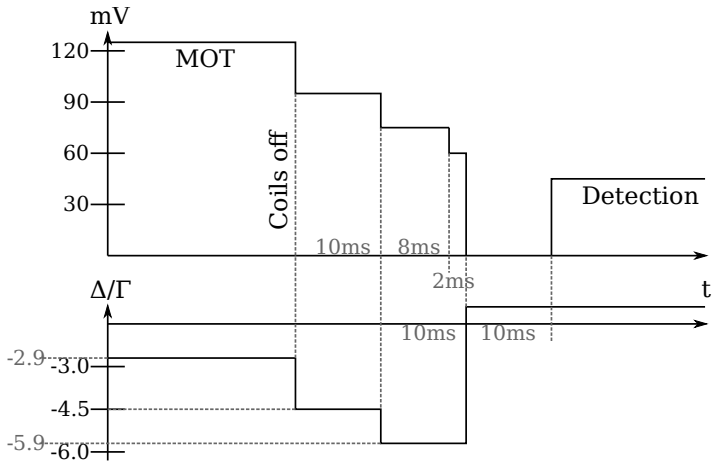

Figure 4.2: Molasses cooling sequence for reducing temperature below the MOT limit. After the trapping field is turned off the light intensity is decreased in a stepwise manner. Simultaneously the detuning from resonance is increased further towards the red in a stepwise manner. After the cooling steps the frequency is stepped back towards resonance for detection of the atoms. The time taken for the lock to follow this large frequency step limits the earliest time a detection pulse can be applied to the atoms.

the width of the cloud as described by [74]:

$$T_{x,y} = \frac{m_{Rb}}{k_B}\left(\frac{\sigma_{x,y}(t)^2 - \sigma_{x,y}(0)^2}{t^2}\right) \tag{4.1}$$

The sequence used for molasses cooling is shown in Fig. 4.2. Our experimental control allowed us to step or ramp both the intensity and detuning of our light and it should be noted that the sequence shown here isn't necessarily optimised but provided the best results after some iteration.

Examining Fig. 4.2, following the MOT period the coils are switched off and immediately the intensity of the light field is decreased and the detuning increased in a stepwise manner. 10 ms later a further step is applied to both. Two more steps are applied to the intensity in the next 10 ms, reducing it to 0 after which a final step is applied to the detuning to shift it towards resonance for detection. This must be done in advance of our detection due to slow lock scanning speed. The whole molasses sequence takes 20 ms.

The reduced temperature profile from such a sequence is shown in Fig. 4.3. One can see a decrease in temperature from the Doppler limit of 146 μK to $\sim$ 33 μK in the x-direction and $\sim$ 64 μK in the y-direction. Further investigation is required to reach desired low μK temperatures. In particular it is predicted that ramping the intensity rather than stepping should aid in cooling as the cloud can follow the ramp adiabatically.

The current x-temperature of molasses is undesirable because it corresponds to $\sim$ 55 mm/s of horizontal velocity. For a total parabolic flight time of 750 ms this relates to a 42 mm spread of the atom cloud in the detection region making it difficult to collect a reasonable signal. This effect would be even worse in the

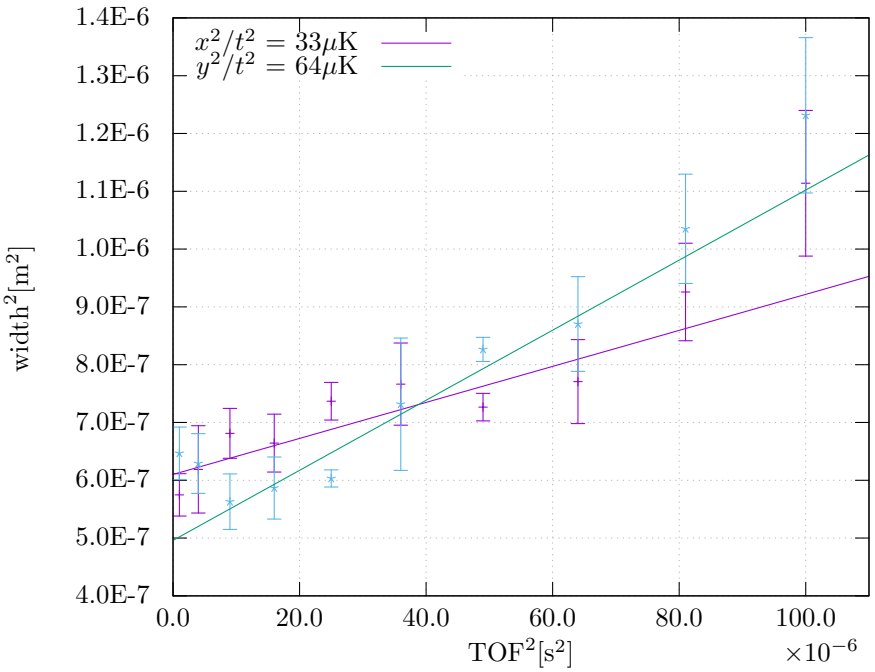

Figure 4.3: Time of flight measurement to assess temperature of 3D MOT following sub-Doppler (molasses) cooling. Width of the cloud for various free expansion times measured from a 2D Gaussian fitting program. Fitted gradients give temperatures an order of magnitude higher than desired.

vertical direction but velocity selection mitigates this to an extent.

Even at the 1 μK temperatures specified in the design of Tab. 3.1 there is a 7 mm horizontal spread. Spatial inhomogeneity caused by this expansion can create unwanted sources of noise. One way to address the spread is to perform a horizontal velocity selection during atom preparation [80] at the expense of total atom number.

4.2.2 Launch Velocity Tuning

To launch atoms the moving molasses technique [1,81] is used. The downwards and upwards propagating trap beams are detuned relative to each other such that the frequency imbalance causes an acceleration upwards of the atoms. It should be noted here that acceleration does not imply heating. Only those atoms whose Doppler profile matches that of the detuned laser beams are accelerated as all of the beams will appear to have the same frequency. The velocity of the atoms in this regime is given by:

$$v_z = \frac{\delta}{k \cos \xi} \tag{4.2}$$

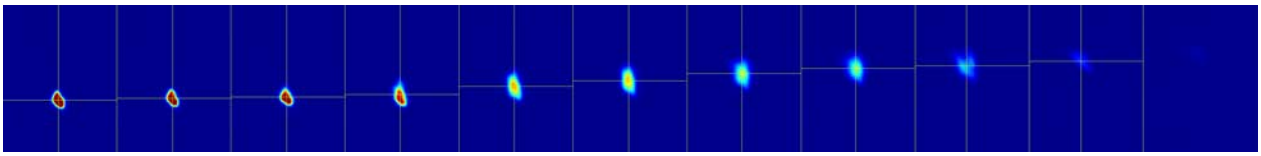

Figure 4.4: Sequence of fluorescence images of launched atom cloud at 500 μs intervals. The visibility of the cloud decreases as the intensity of launching light was ramped down to provide cooling. There is a clear demonstration of the central point of the cloud accelerating vertically.

where δ is the relative detuning, k is the wavevector of the light and ξ is the angle between the trap beam and the horizontal axis, in this experiment $\xi = 45°$. The moving molasses technique damps the atomic velocity to zero with respect to the moving frame, their velocity spread about their mean velocity is equivalent to that in the stationary molasses regime and hence the temperature is the same in both cases despite this upwards force.

It is straightforward to show that the height to which the atoms are launched depends on their velocity as:

$$v_z = \sqrt{2gh} \tag{4.3}$$

and for the maximum height of the experiment, 70 cm, a maximum velocity of 3.7 ms^{-1} is needed.
Figs. 4.4 and 4.5 show launch data captured in the experiment. Absorption images for the cloud were taken at different flight times over successive runs to map how the cloud launches when detuning is applied.

The agreement between theory and experiment is poor. There are two logical explanations for the disagreement. The first reason is down to how the velocity of the cloud is calculated from experiment. A fitting algorithm to find the centre of the cloud is used and the difference between centres allows one to estimate the velocity based on there always being 500 μs between images. However, the clouds were often diffuse and disorderly making it difficult to accurately pinpoint the centre. The images used to calculate the velocity are a 2D absorption image of the cloud in one particular plane, only showing the vertical motion. The images give no information about the launch angle which could realistically have a component perpendicular to the imaging plane and would result in a lower measured velocity than that predicted by theory and would explain the disagreement between gradients.

The second reason is due to poor optimisation of the magnetic field compensation and intensity balance in the trapping beams. Residual magnetic field gradients from poor compensation cause a force on the atoms during the molasses cooling and launch period where the anti-Helmholtz field is switched off but the light remains on. Such a force would explain the velocity offset of the fitted line from zero velocity at zero

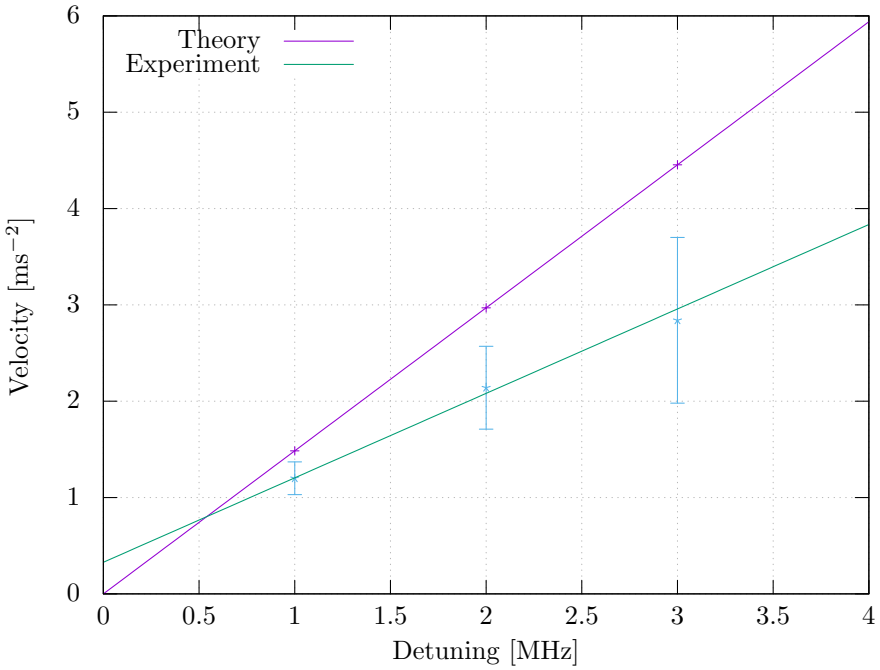

Figure 4.5: Launch velocity of atoms as a function of AOM detuning. *Purple:* Theoretical launch velocity based on beams making a 45° angle with the launch direction. *Green:* Measured launch velocity is less than the theoretical prediction by approximately half.

detuning and could change the launch angle, resulting in the lower measured gradient. The argument for intensity imbalance of the trapping beams is similar as this also creates a force imbalance. Tests with better compensation fields and stabilised beam intensities have not yet been carried out.

4.3 Rabi Oscillations

4.3.1 State Transfer with Raman Light

An atom interferometer sequence revolves around the $\pi/2 - \pi - \pi/2$ pulses. Calculation of pulse durations from theory is possible but our resolution of Raman detuning was limited by the laser to $\sim 1\ pm \approx 0.1$ GHz. It was therefore easier to measure how long these pulses should be for fixed detunings and intensities of the Raman beam.

Preparing the atoms for this measurement involved trapping $\sim 10^8$ atoms, doing 20 ms of molasses cooling to reach low 10s of μK and finally preferentially preparing the atoms in the $|F = 2\rangle$ level by disabling the cooling light but leaving the repumping light on for a few extra ms. To transfer atoms to the $|F = 1\rangle$ state

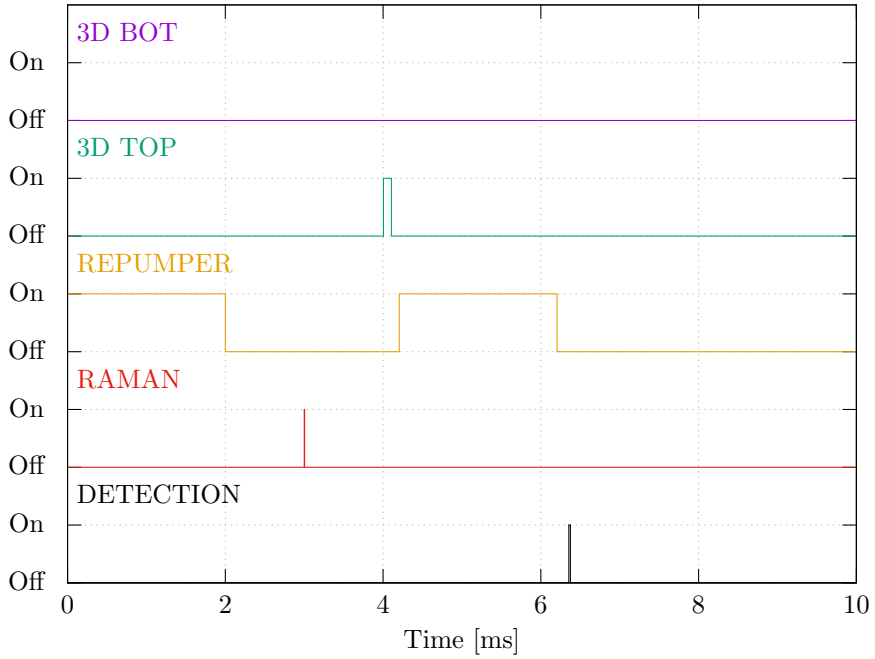

Figure 4.6: Computer sequence used to observe Rabi oscillations with atoms prepared in the $|F = 2\rangle$ state following molasses cooling. A short Raman pulse of variable duration transfers an amount of atoms to the $|F = 1\rangle$ state then the remaining $|F = 2\rangle$ atoms are blown away by the 3D TOP light. The $|F = 1\rangle$ atoms are then repumped and detected.

a pair of co-propagating circularly polarised light fields with a frequency difference equal to the hyperfine groundstate splitting of 6.834 GHz and equal intensity are used. The number of atoms transferred are then detected by blowing away the remaining $|F = 2\rangle$ atoms, repumping the $|F = 1\rangle$ and detecting the new $|F = 2\rangle$ atoms.

We use several fluorescence traces like those shown in Fig. 4.7 to generate Rabi oscillation data. For each shot (trace) we normalise the transfer fluorescence by first subtracting the detection background and then dividing by an average of the MOT fluorescence minus the trapping background light for a short period before the molasses cooling begins. This is repeated for 10 shots to average fluctuations and then the Raman pulse length is increased. A plot of transfer fluorescence vs. pulse length is created.

For an intensity of 131 mW/cm^2 and detuning of 2.2 GHz from the intermediate level the Rabi oscillation recorded is shown in Fig. 4.8.

Fig. 4.8 follows the shape outlined in Eq. 2.31 with an additional damping term. The fitted Rabi oscillation period of 33.8 kHz agrees roughly with a theoretical value of 58.1 kHz based on our parameters (see App. A.3). The decreased oscillation frequency measured here is indicative of the atoms interacting with a lower intensity area of the Gaussian wavefront in comparison to the model which assumes a flat wavefront. For the model

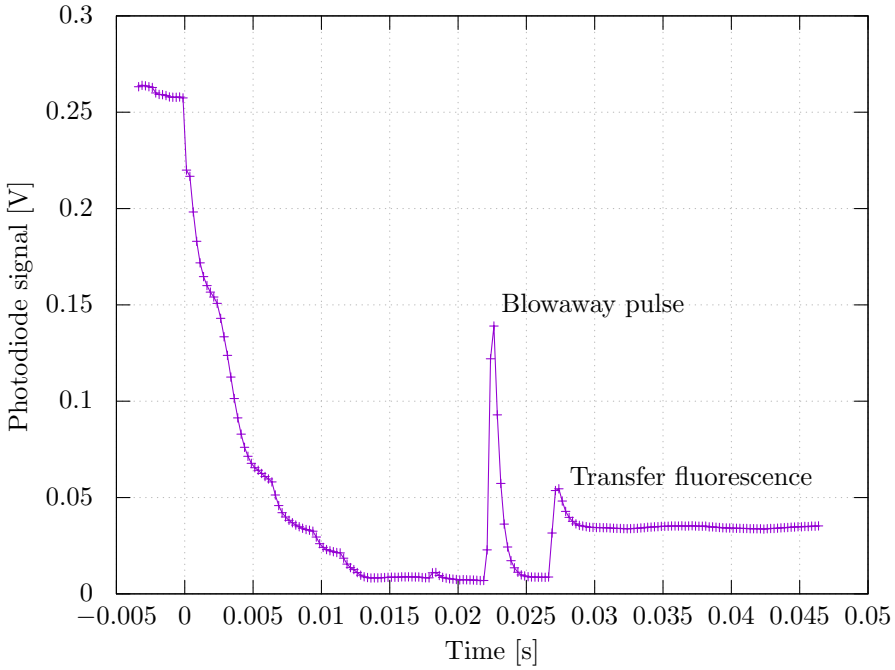

Figure 4.7: Fluorescence signal recorded for sequence outlined in Fig. 4.6. The initial high fluorescence signal comes from the atoms trapped in the 3D MOT. The signal quickly falls as the intensity is stepped down for molasses cooling. The peak at ~ 0.02 s corresponds to the blowaway from the 3D TOP beams. The following peak is the signal from the transferred atoms as they are repumped and illuminated with detection light.

and measured data to agree the cloud centre would need to move by ~ 10 mm from the beam centre to see the intensity which would drive this oscillation. This is larger than the measured drift in Fig. 4.1 suggesting the centres were poorly aligned. Given that our Raman telescope was ~ 700 mm from the atom cloud, a misalignment of 10 mrad from the vertical would easily account for this error.

There is a heavy amount of damping which causes the oscillation to die down after ~ 2 cycles. Loss of coherence such as this is related to the temperature of the cloud [82]. The energy levels of the atoms are shifted by the ac Stark effect which is proportional to the laser intensity at the atom's position. On average, the hotter atoms will experience a smaller light shift than the cold ones and this results in a range of Rabi frequencies across the cloud. One would expect the coherence to increase as the temperature decreases, allowing one to observe more oscillations.

The contrast of the oscillation is low, i.e. there is a small amount of state transfer, on the order of 12%. This can be explained if the atoms are spread among the 5 m_F levels in the initial $|F = 2\rangle$ state. Assuming an even distribution (for simplicity) then immediately 40% of the atoms are lost from the $m_F = \pm 2$ states which are unable to make the $\Delta m_F = 0$ transition to the $|F = 1\rangle$ state, limiting the number of atoms which

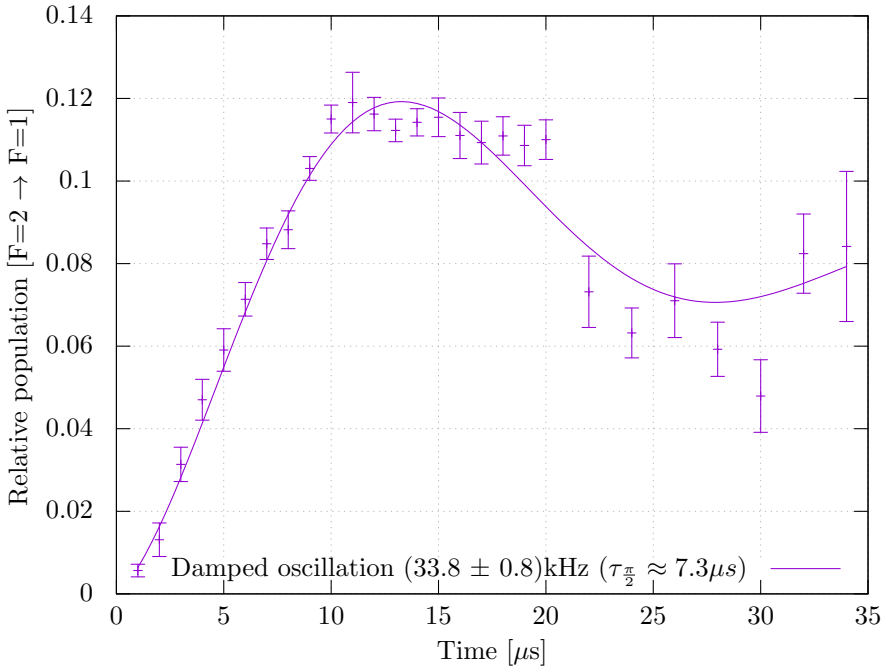

Figure 4.8: Rabi oscillation for intensity 131 mW/cm^2 and detuning 2.2 GHz. The data shows the number of atoms transferred to the $|F = 1\rangle$ state as a function of the duration of the Raman pulse. Each point is an average over 10 measurements.

can interact. The single-photon detuning, Δ_R and two-photon detuning, δ_R, from the 6.834 GHz splitting should account for the remainder of the contrast loss in accordance with with Eq. 2.31.

There are experimental improvements to be made that would improve the oscillation data shown here. For a start, the beam balance between the MOT laser beams was known to fluctuate as in Fig. 5.4. This has several major consequences for measuring Rabi oscillations. As already mentioned, the 3D MOT position would drift over the course of Rabi measurements as the beam balance drifted. This has the effect that the cloud is not in the same position with respect to the Raman beam wavefront in every measurement and hence a different intensity is seen. Referring back to Eq. 2.16 a different intensity results in a different transition probability. Secondly the temperature reached following molasses cooling would drift for the same reason. This had the effect of changing the coherence and damping the oscillations. One final remark is again about the magnetic fields in the 3D MOT region. It would be preferable to have a well defined bias field for doing Rabi oscillations to prevent noise from unwanted m_F levels appearing in measurements.

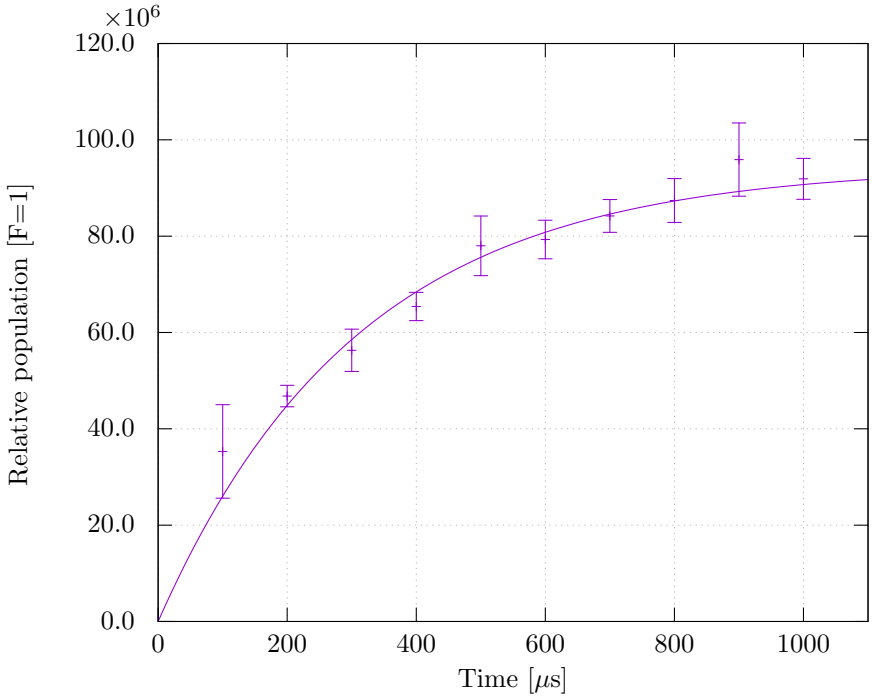

Figure 4.9: Atom population in $|F = 1\rangle$ for different durations of cooling with no repumping light. Each point is an average of 10 measurements with standard deviation error.

4.3.2 Cooling Depump

For doing state preparation in the interferometer it was necessary to investigate whether we could completely extinguish repumping light as this would transfer atoms back into the $|F = 2\rangle$ level when they would ideally be prepared in the magnetically insensitive $|F = 1\rangle$ level. A similar sequence to the one used in the previous section was used here but instead the cooling and repumping are reversed at the end of the sequence such that the atoms accrue in the $|F = 1\rangle$ state. The remaining $|F = 2\rangle$ atoms are blown away before the $|F = 1\rangle$ atoms are repumped and detected.

The number of atoms in the $|F = 1\rangle$ state varies with the duration the repumping light is disabled suggesting that the repumper is sufficiently weak. After 1 ms the number of atoms appears to saturate and so for complete transfer to $|F = 1\rangle$ one needs only apply 1 ms of cooling with the repumper disabled.

4.4 Ramsey Fringes

The sequence shown in Fig. 4.10 to generate Ramsey fringes is a modified version of that used to show Rabi oscillations with atoms prepared in the $|F = 2\rangle$ state. Modification here refers to adding a second $\pi/2$

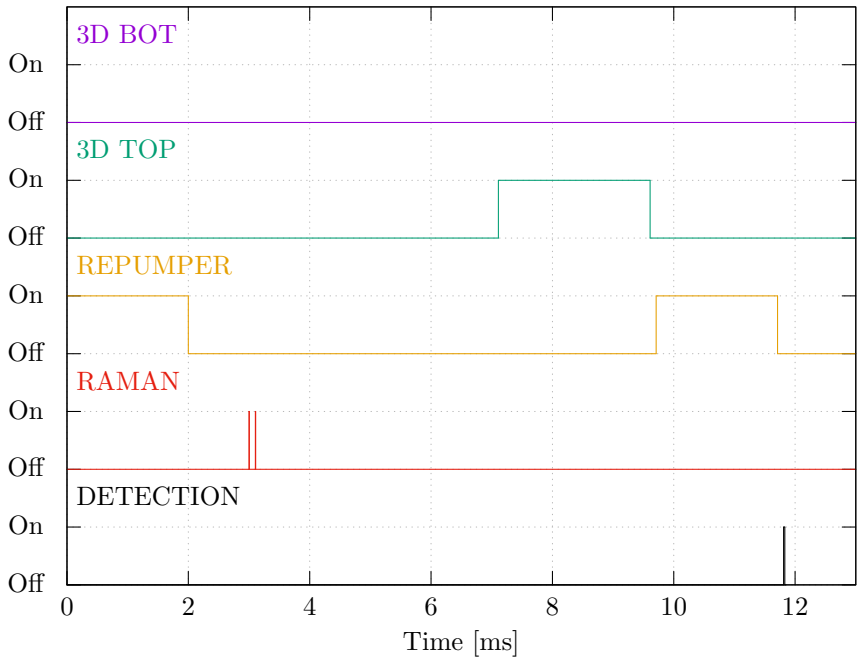

Figure 4.10: Ramsey sequence for measuring interference fringes between hyperfine levels. The sequence is essentially the same as that used for Rabi oscillations but employs two Raman pulses tuned to $\pi/2$ duration. The population in the $|F = 1\rangle$ state is then measured as a function of the two-photo Raman detuning which is varied between shots.

pulse to interfere the atoms with themselves, equivalent to the Ramsey technique in NMR spectroscopy [48]. The duration of the Raman pulses is set to be $\pi/2$ by first sweeping the Rabi measurement sequence and extracting the pulse length. The Ramsey sequence then involves: preparing atoms in $|F = 2\rangle$, applying $\pi/2$ pulse, waiting some 100 μs, applying $\pi/2$ pulse, blowaway of $|F = 2\rangle$ atoms and finally repumping and detecting $|F = 1\rangle$ atoms. Between the first and second pulses the frequency detuning between the two Raman fields is stepped by some kHz and this value is swept over many measurements to map an interference fringe.

Shown in Fig. 4.11 are the data for 1 and 2 kHz detuning steps when scanning the interference fringes. Theoretically, the interferences should look like a sine-squared oscillation inside a sinc^2 envelope. One may be able to convince themselves that this is the case but it is far from clear. The obvious reason for this is that the contrast is poor. The number of atoms in the $|F = 1\rangle$ state only changes from $\sim 7\%$ to $\sim 9\%$ making it difficult to draw any real conclusion.

The poor resolution of the data can be explained as follows. For a start, atoms were prepared in the $|F = 2\rangle$ state meaning the atoms in the $m_F = \pm 2$ are not addressed as $\Delta m_F = 0$ from selection rules - lowering the overall signal. The Rabi $\pi/2$ duration was inferred from a graph for this measurement rather than fitted accurately and we estimate this could be as much as 20% below the real value. Imperfect transfer

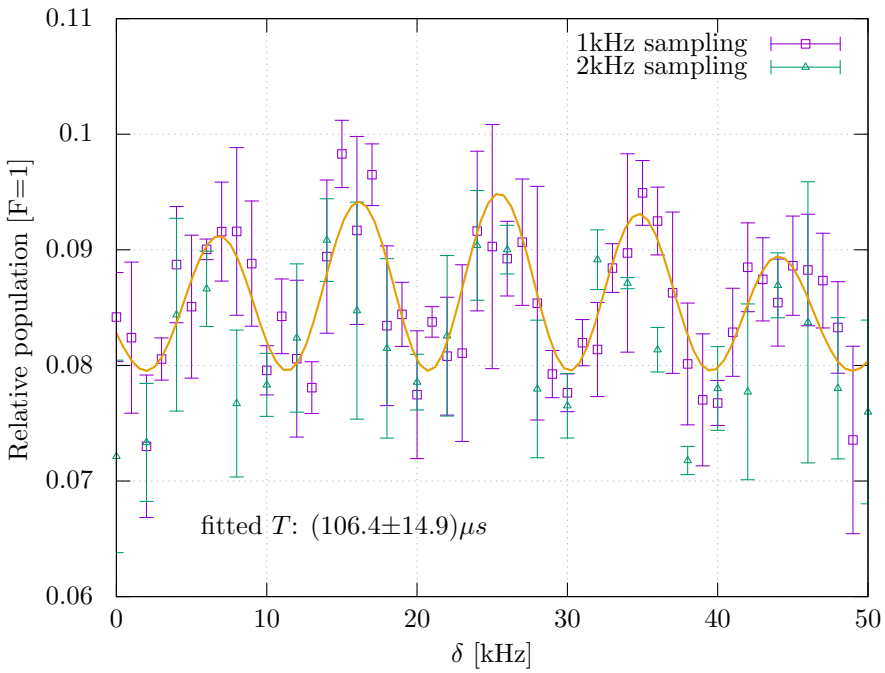

Figure 4.11: Population of $|F = 1\rangle$ state measured for 1 and 2 kHz detuning steps with $\tau_{\frac{\pi}{2}} = 7$ μs. Time (T) between Raman pulses was 100 μs.

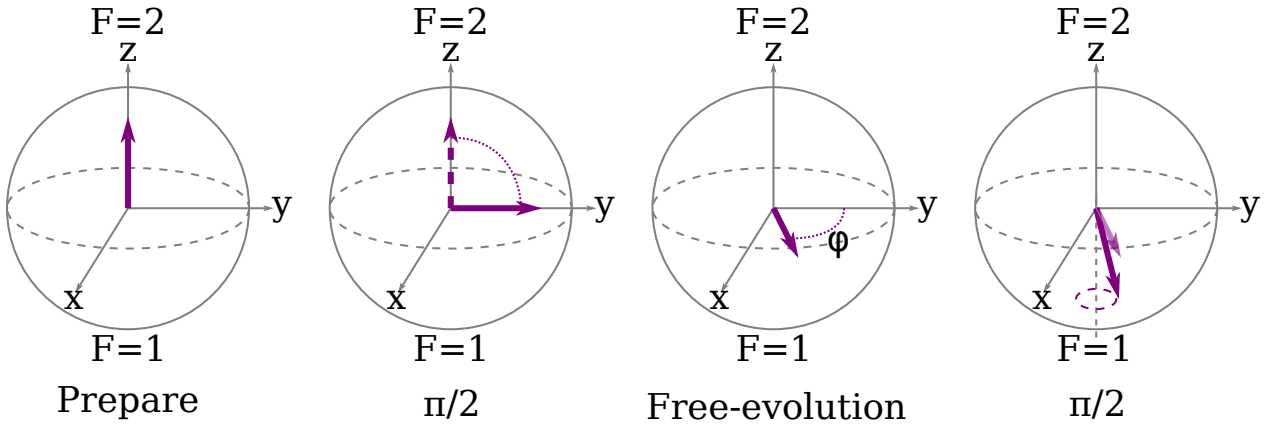

Figure 4.12: Bloch sphere interpretation of Ramsey interference for a $\pi/2 - \tau - \pi/2$ sequence. For a sample intially prepared in the $|F = 2\rangle$ state, the first $\pi/2$ pulse acts to put the atoms in an equal superposition of $|F = 1\rangle$ and $|F = 2\rangle$ illustrated by a rotation onto the x-y plane. Over time the vector will precess about this axis causing dephasing as the two states evolve at different rates. Application of a final $\pi/2$ creates an interference proportional to the phase between states.

for both $\pi/2$ pulses in the Bloch-Sphere picture illustrates the weakened interference if one looks at Fig. 4.12 and imagines an imperfect transfer consisting of the $\pi/2$ pulse not rotating the vector all the way between the z-axis and x-y plane. The choice of 100 μs evolution time was arbitrarily chosen. In reality, interference fringe visibility varies as a function of free evolution time with a decrease in visibility for longer times. Shorter evolution times may have aided visibility.

The experimental flaws that plagued the Rabi measurements will have an influence on these measurements. Fluctuations in the Raman laser power will cause fluctuations in the $\pi/2$ time. The number of atoms loaded into the MOT, the temperature achieved by molasses cooling and the position of the MOT in the Raman laser would all change between measurements. Changes in temperature are of particular importance as it effects the dephasing rate during the free-evolution period. The number of atoms loaded into the MOT can be normalised with the number of atoms transferred for a given $\pi/2$ time but the position and temperature of the MOT affect the $\pi/2$ time. Finally, magnetic field control was poor resulting in a badly defined quantisation axis for the circularly polarised light. This would have resulted in every m_F level contributing in some way to the signal and an overall degradation of the measurement.

4.5 Improved Oscillations

For the previous studies of Rabi oscillations and Ramsey fringes atoms were prepared in the $|F = 2\rangle$ state. This was essentially only chosen because it was the simplest thing to do via the computer control. To progress towards better measurements it was more logical to prepare atoms in the $|F = 1\rangle$ state which has fewer m_F levels and study the effects of state manipulation. The Raman telescope was exchanged for one which gave a collimated beam of 19 mm waist to increase intensity for a given laser power.

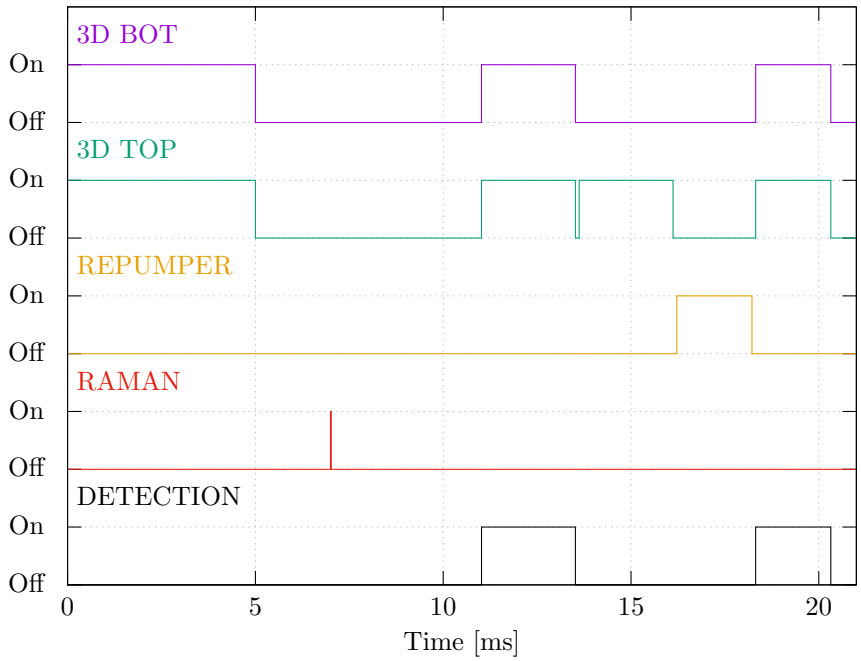

Figure 4.13: Computer sequence used to observe Rabi oscillations with atoms prepared in the $|F = 1\rangle$ after molasses cooling. A short Raman pulse of variable duration transfers atoms to the $|F = 2\rangle$ state which are then detected by fluorescence illumination with 6 MOT beams. These $|F = 2\rangle$ atoms are then blown away by the 3D TOP beams so that the remaining $|F = 1\rangle$ atoms can be repumped and detected for total atom number normalisation.

Using the knowledge of the cooling depump effect from the previous section, atoms were preferentially prepared in the $|F = 1\rangle$ state at the end of molasses cooling. Following preparation a Raman pulse of a pair of co-propagating circularly polarised light fields with a frequency difference equal to the hyperfine groundstate splitting of 6.834 GHz and equal intensity is used. This has the effect of transferring atoms from $|F = 1\rangle$ to $|F = 2\rangle$. Detection of atoms in $|F = 2\rangle$ is then done by fluorescence before blowing away these $|F = 2\rangle$ atoms. Blowaway here is not entirely necessary as the detection is destructive, it is done as a precaution. The remaining $|F = 1\rangle$ atoms that weren't transferred by the Raman pulse are then repumped to $|F = 2\rangle$ and detected again with fluorescence.

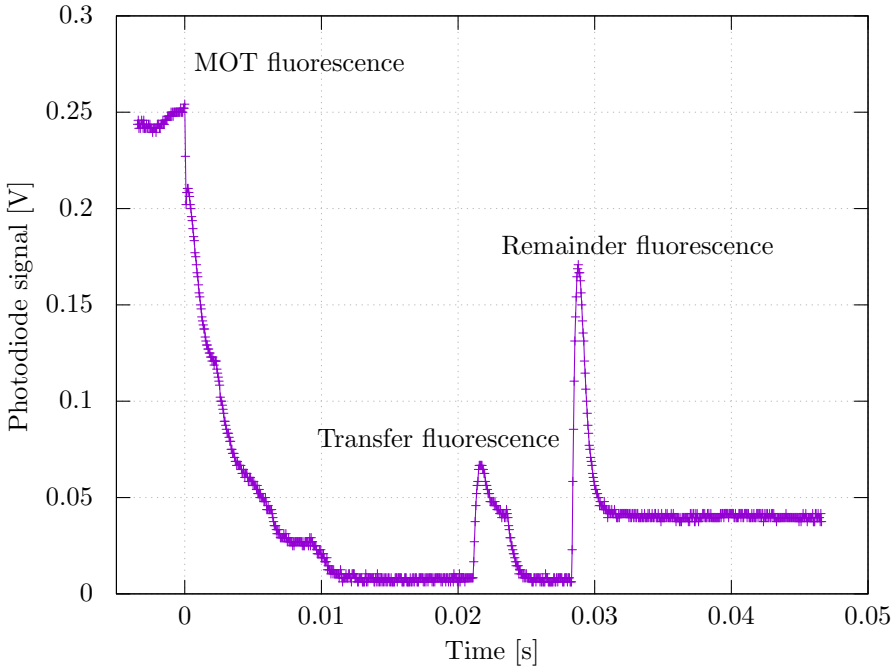

Figure 4.14: Fluorescence signal recorded for sequence outlined in Fig. 4.13. The initial high fluorescence signal comes from the atoms trapped in the 3D MOT. The signal quickly falls as the intensity is stepped down for molasses cooling. The peak at ~ 0.02 s corresponds to the fluorescence from the atoms transferred to the $|F = 2\rangle$ by the Raman pulse. The following peak is the signal from the remaining $|F = 1\rangle$ atoms as they are repumped and illuminated with detection light.

The first peak corresponds to the fluorescence from atoms that were transferred from $|F = 1\rangle$ to $|F = 2\rangle$. The lack of signal from the blowaway pulse in this trace is indicative that the first detection was destructive and there are no atoms to blowaway. There is a second peak from the repumped atoms being detected. In an ideal case the sum of the first and second peaks should reach a similar fluorescence value as at the end of the MOT stage. A big discrepancy here suggests that many atoms were lost and the cloud was not cold or well magnetically compensated.

Plotting the value of the transferred fluorescence normalised to the MOT fluorescence against the Raman pulse duration generates the plot for Rabi oscillation shown in Fig. 4.15.

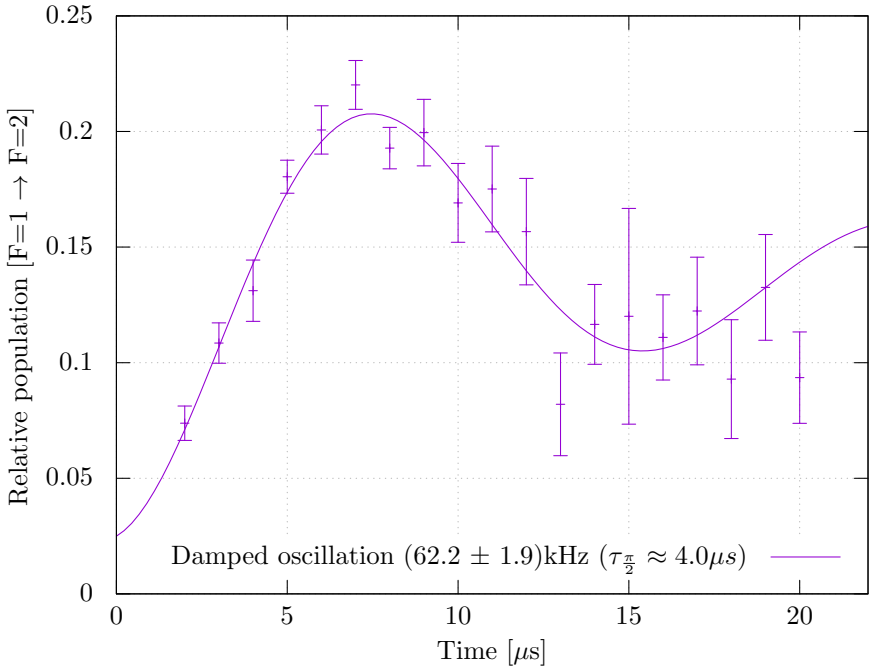

Figure 4.15: Rabi oscillation for intensity 194 mW/cm^2 and detuning 4.7 GHz. The data shows the number of atoms transferred to the $|F = 2\rangle$ state as a function of the duration of the Raman pulse.

The theoretical Rabi frequency for these laser parameters is 209 kHz, roughly triple the measured frequency of 62.2 kHz. Again the theory is assuming a flat beam so the discrepancy might be explained by the Gaussian nature. The point at which the cloud sees one third of the intensity is $\sim$ 7.5 mm from the beam center. The cloud center was measured to drift by $\sim$ 5 mm (see Fig. 4.1) which gives better agreement to the theoretical value. It also highlights a critical stability problem for later gravity measurements.

Comparing with Fig. 4.8 there is a major difference in the contrast. For preparation in the $|F = 1\rangle$ state, the peak transfer of atoms to $|F = 2\rangle$ is double that compared to when atoms are prepared in $|F = 2\rangle$. This can be explained if one considers the difference in the number of m_F levels and selection rules.

Both traces agree on loss of coherence after one/two oscillations which indicates the temperature of the cloud is consistently too high to maintain good coherence.

4.6 Computer Control

DDS Characterisation

The direct digital synthesiser (DDS) controls both the frequency and amplitude of all lasers in this experiment.

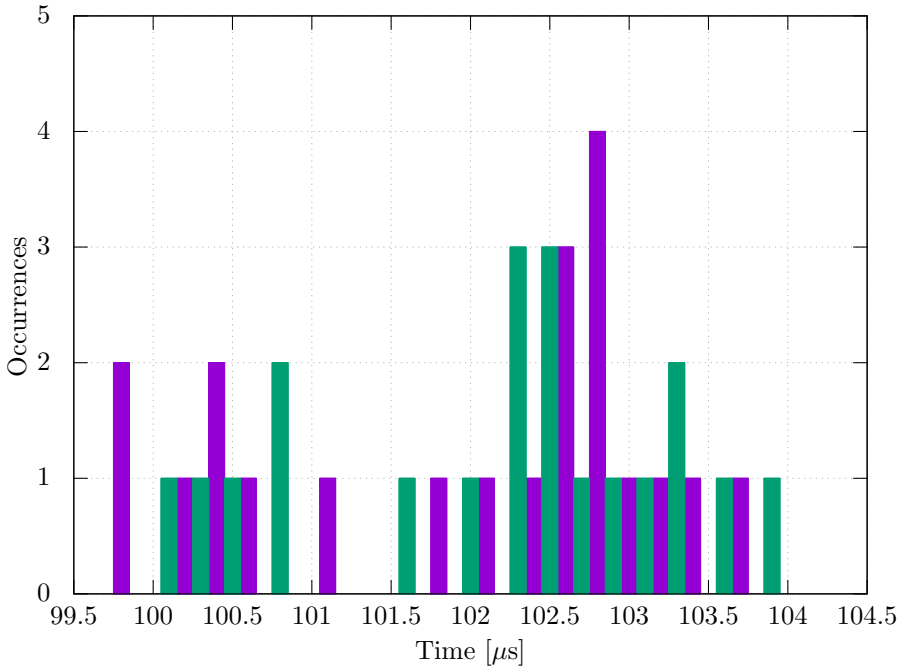

Figure 4.16: Jitter analysis of the DDS used to control the intensity and frequency of cooling light for 100 μs minimum resolution steps. Data shows a jitter of $\sim$ 4% or 4 μs. Colours are for illustration only.

It is therefore important to understand how it behaves with regards to timing robustness in order to correctly plan sequences. From specification, the minimum timing resolution the DDS can perform is 100 μs - i.e. after receiving a control trigger it will take 100 μs to execute the next command stored in its memory. Using an auxiliary output of the DDS allowed us to monitor when it executes a change of output. The delay between the control trigger and this signal are shown in Fig. 4.16.

The maximum jitter is on the order of $\sim$ 4 μs. This is significantly lower than the DDS timing resolution and for most parameters operated on by the DDS in this experiment it is a negligible effect.

4.7 Conclusion

Assembly and initial testing of the experiment revealed substantial limitations that would prevent the experiment from reaching the projected sensitivity. The stability of the 3D MOT was particularly bad which was reflected by the attempt to record Ramsey interference fringes. Stability problems were attributed to the fibre system used to manipulate the light. It was known before assembly that this would be a risky design choice but the potential benefits were many. For this reason the experiment evolved into two parallel

development streams.

- Assess the viability of fibre components to understand if a similar system could be realised in the future. This included research into more compact Raman laser systems using fibre laser components and sophisticated modulation techniques.

- Build a quick and simple free-space light delivery system for the 3D MOT to push for better performance and study how the experiment will perform under ideal conditions. The motivation here was to work towards a sensitive gravity measurements and then slowly replace components to enhance portability and study their impact on sensitivity.

CHAPTER 5

FIBRE OPTIC DELIVERY SYSTEM

This chapter presents the work done on the fully integrated fibre system used to manipulate light in the GGtop experiment. A fibre system was chosen over a free-space optics approach used in most cold atoms experiments as a means of providing robustness for field applications. As an additional benefit, a fibre-based approach allows for a very compact light delivery system even when compared to a miniature optics setup. The entire system was designed and assembled in-house from a collection of commercially available fibre-integrated components.

The chapter will start with an outline of the system as a whole; to familiarise the reader with the subsequent discussion. In this outline, the choice of using a fully spliced system will be motivated by presenting the typical tolerances of manufactured fibre components. This ideaology will be reinforced in the following sections where data is presented to support the design choices. The chapter will close with some recent tests that have been done towards improving the current deign.

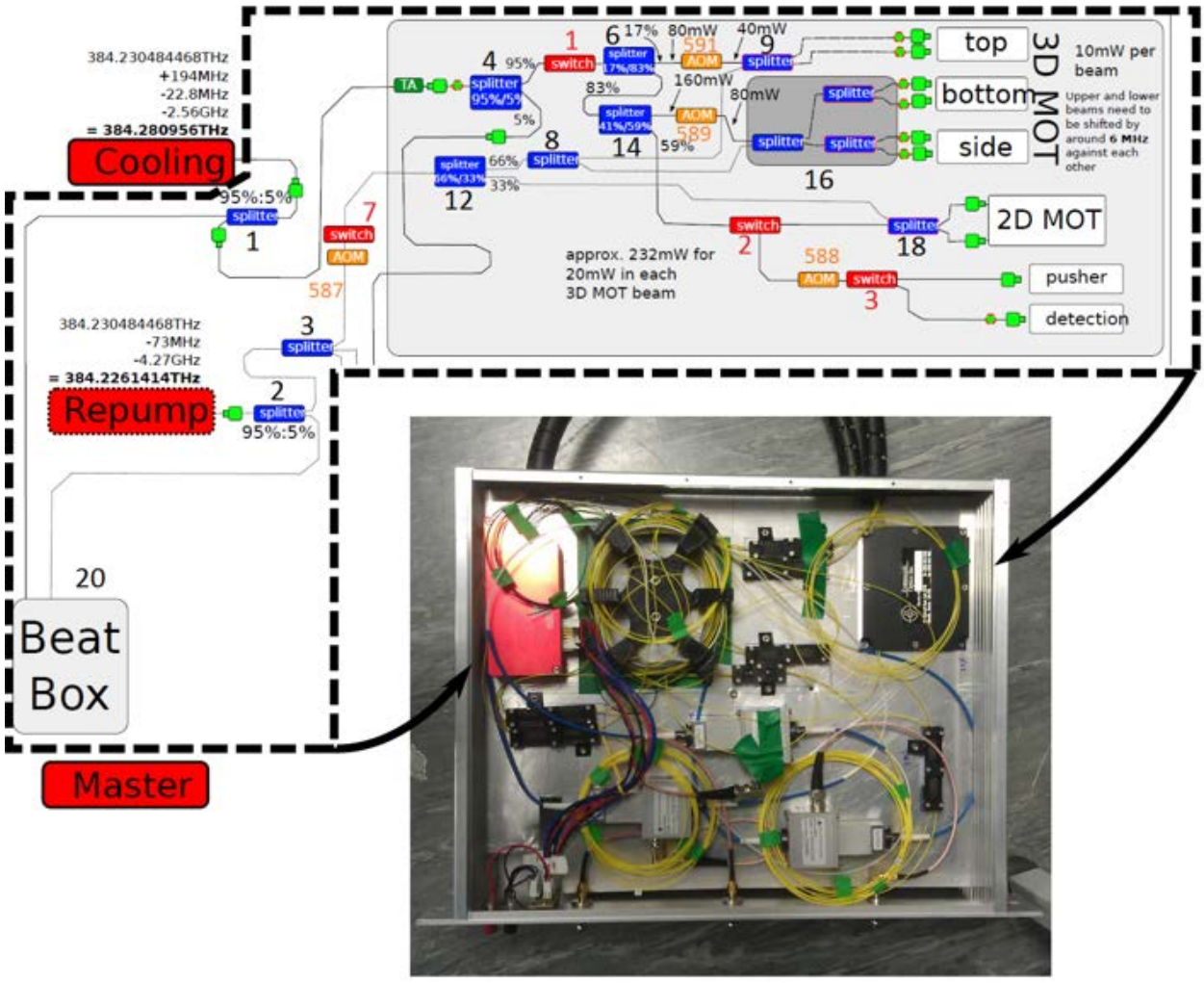

Figure 5.1: Schematic and packaged fibre system. Every component necessary to split, redirect and modulate the light is contained in a fully fusion-spliced network of integrated devices. Once packaged the whole system fits in a 3U height 19-inch rack box with front panel connections for modulation and TTL signals.

5.1 GGtop Fibre Delivery

To start, the fully assembled system is presented so that one can gain an appreciation for the complexity and performance. The individual components will then be discussed in more detail to illuminate possible problems or undesirable properties. It should be noted that everything discussed from this point involves polarisation maintaining (PM) fibres and FC/APC connectors unless otherwise stated.

Fig. 5.1 highlights the components used and the package in which they are mounted. Everything fits inside a 3U height 19-inch rack mountable box. An effort could be made to minimise the size of this box further but this was initially avoided for fear of over constraining the fibre bending radii which could introduce stress

Connector Type	Key Width (mm)	Key Slot Width (mm)
Narrow Key	1.97-2.02	2.03-2.08
OZ Optics	1.98-2.02	2.03-2.07
Seikoh Gieken	1.98-2.02	2.03-2.07
Diamond SA	1.99-2.00	2.02-2.05
Wide Key	2.09-2.14	2.15-2.20
Seiko Instruments	2.09-2.14	2.15-2.20
Diamond SA	2.14-2.15	2.17-2.23

Table 5.1: Industry standard tolerances for wide and narrow key PM fibres along with manufacturer tolerances. [83]

birefringence in an axis different to that provided by the stress rods of the fibre - ruining the polarisation maintaining ability.

Between each component shown in the diagram a spliced connection is made. The justification for this design choice was to reduce the amount of light intensity loss that is typically associated with fibre-to-fibre mating sleeves. The precision of a fibre splice is higher than the mechanical tolerance of both the fibre key and the mating sleeve key slot and so has the added benefit of reducing polarisation fluctuations from angular misalignment. Typical tolerances for several fibre manufacturers are given in Tab. 5.1.

Taking the narrow key as an example, the worst case scenario leads to a maximum difference in tolerance between key and key slot of 0.09 mm. With such tolerances there is 1.71° of freedom for the fibre to rotate. For an ideal fibre, the polarisation extinction ratio from angular alignment is [83]:

$$ER \leq 10 \log_{10}(\tan^2 \theta) \tag{5.1}$$

From this equation, to achieve an extinction ratio better than 30 dB (i.e. <0.1%) the fibre must be aligned to better than 1.8° which is close to mechanical tolerances. If several fibres are connected in series using these mating sleeves, each with a 1.71° misalignment then there is a small accumulation of polarisation extinction loss at every connection. Over many connections this can degrade polarisation quality substantially.

On the other hand, the splicing tool used to join fibres achieves a typical precision of 0.6° giving an extinction ratio of 40 dB per splice.

5.1.1 System Performance

Output Power

The power output from every designated output fibre from the system was tested to check for any losses in the splices.

Output	Out Power (μW)	In Power (mW)	Percentage (%)
MOT 2	535.5±2	9.61±0.16	5.55±0.09
3D TOP(a)	211.0±2	9.66±0.16	2.18±0.04
3D TOP(b)	242.0±2	9.25±0.16	2.62±0.05
3D SIDE(c)	209.9±2	9.34±0.16	2.25±0.04
3D SIDE(d)	199.0±2	9.42±0.16	2.11±0.04
3D BOT(e)	201.1±2	9.41±0.16	2.14±0.04
3D BOT(f)	213.0±2	9.48±0.16	2.25±0.04
2D MOT(x)	760.0±2	9.37±0.16	8.11±0.14
2D MOT(y)	759.0±2	9.35±0.16	8.12±0.14
Pusher	713.0±2	9.23±0.16	7.72±0.14
Detection	701.0±2	9.13±0.16	7.68±0.14
Total			50.73±3

Table 5.2: Output power from fibre network module 1. Input power is measured at the input to splitter 4 in Fig. 5.1 for every measurement to decouple power fluctuations. The percentage is defined as the ratio of power from the output fibre of interest to the input power at splitter 4. The "Total" is the sum of the output power percentages which shows that approximately half of the input power is lost.

Output	Out Power (μW)	In Power (mW)	Percentage (%)
MOT 3	455.1±2	9.33±0.39	4.88±0.21
3D TOP(a)	288.8±2	9.39±0.39	3.08±0.13
3D TOP(b)	283.6±2	9.38±0.39	3.02±0.13
3D SIDE(c)	213.0±2	9.06±0.39	2.35±0.10
3D SIDE(d)	228.6±2	8.63±0.39	2.65±0.12
3D BOT(e)	205.6±2	8.44±0.39	2.44±0.12
3D BOT(f)	216.4±2	8.50±0.39	2.55±0.12
2D MOT(x)	678.0±2	8.50±0.39	7.97±0.37
2D MOT(y)	836.0±2	8.60±0.39	9.72±0.44
Pusher	651.0±2	8.55±0.39	7.61±0.35
Detection	665.0±2	8.55±0.39	7.00±0.32
Total			53.27±8

Table 5.3: Output power from fibre network module 2. Input power is measured at the input to splitter 4 in Fig. 5.1 for every measurement to decouple power fluctuations. The percentage is defined as the ratio of power from the output fibre of interest to the input power at splitter 4. The "Total" is the sum of the output power percentages which shows that approximately half of the input power is lost.

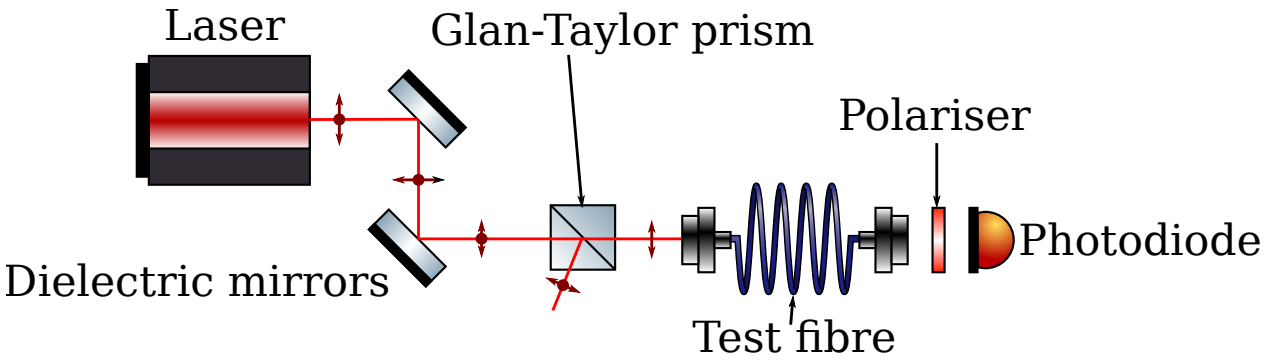

Figure 5.2: Setup for testing polarisation extinction of fibres. Linearly polarised light from the laser is cleaned by 50 dB Glan-Taylor prism before being injected into a test fibre. The output polarisation of the fibre is analysed by a 38 dB polariser and photodiode.

Common to both modules is that $\sim 50\%$ of the input light intensity is lost. This is to be expected with fibre-AOMs which were specified with 3 dBm loss in every path due to coupling efficiency back into the fibre following the crystal. What this suggests is that at the splices themselves there is relatively little loss. One striking feature of both is the imbalance in powers for the 3D MOT outputs. This is due to the splitting ratio tolerances of our fibre splitters which is $\pm 0.5\%$ (i.e. $50:50 \rightarrow 49.5:50.5$). For trapping it is therefore required that we balance the output powers using a polariser in the MOT telescopes.

One consideration that has not been implemented yet was the capability to temperature stabilise the fibre splitters. From datasheets it was estimated that the splitting ratios would vary by $\sim 0.186\%$ per $^{\circ}C$. When the experiment is taken into the field it is perfectly reasonable to expect temperature changes of over $10^{\circ}C$ which will alter beam balances. The ability to temperature stabilise would serve a dual purpose; firstly it would remedy long term temperature drifts affecting the beam balance and in addition it would provide a method of tuning the splitting ratio for optimisation purposes.

Output Polarisation Extinction Ratio (PER)

The polarisation quality of the fibre outputs is an important quantity for both cooling and launching of the atoms. For cooling, the polarisation quality is directly related to the intensity balance in the trapping beams which affects the number of atoms that will reach the desired temperature and the position/shape of the cloud. A similar problem is encountered for launching where an intensity imbalance will result in an angled launch trajectory.

A simple experiment (Fig. 5.2) containing a Glan-Taylor prism is used to inject a well defined linear polarisation into test fibres. The Glan-Taylor prism is specified to have a PER of 50 dB which far exceeds any fibre under examination.

Output	PER (dB)	Error Bounds (dB)
MOT 3	23.87	23.79-23.94
3D TOP(a)	16.53	16.46-16.60
3D TOP(b)	12.90	12.85-12.94
3D SIDE(c)	14.02	13.97-14.07
3D SIDE(d)	17.22	17.14-17.31
3D BOT(e)	15.50	15.42-15.58
3D BOT(f)	18.44	18.31-18.56

Table 5.4: Output PER from fibre network module 2.

At the output of the fibre light is collimated and passed through a 38 dB polariser (measured) and recorded on a standard photodiode. The PER is then investigated by placing approximately 10 cm of the fibre in a heat bath at $\sim$ 40-50 °C where the thermal shock causes a change in the stress properties. The difference in the transmitted intensity with and without the heat bath is used to determine the PER via:

$$\mathrm{PER} = 10\log_{10}\left(\frac{\Delta I_{\mathrm{bath}}}{I_{\mathrm{air}}}\right) \tag{5.2}$$

where ΔI_{bath} is defined as the largest peak-to-peak intensity change caused by the thermal shock and I_{air} is the maximum transmitted intensity along the wanted axis at normal laboratory temperature. This definition was chosen as it gives a worst scenario measurement of the fibres.

The first entry in Tab. 5.4 is used to monitor the PER of the fibre system directly after the first splitter in the network. What this shows it that already after the first splitter there is a relatively poor definition of polarisation which can only get worse as it propagates through splices and integrated components; the output PER of the total system should be some product of the PERs of individual components[1]. It is believed that this poor quality input is limited by the input fibre which was spliced in-situ with a Thorlabs PM patchcord. As will be shown in Sec. 5.2, there are more suitable fibres for maintaining polarisation.

In addition to the poor input fibre there was a mechanical failure of a switch (red number 1 in Fig. 5.1) which led to it being replaced. Due to mechanical constraints the replacement splicing was done with manual alignment of the fibre stress cores leading to a potential source of polarisation loss.

The outputs for the 3D MOT highlight a very real problem. On average the PER of the 3D MOT fibres is $\sim$ 15.7 dB which corresponds to $\sim$ 2.7% intensity fluctuations. The telescope which delivers light to the atoms contains a polariser identical to the setup used here for assessing polarisation and so intensity fluctuations measured are related to an intensity change of the same amount at the atoms.

[1] i.e. two fibres of PER= 10 dB could give maximum intensity fluctuations in the wrong axis of $I_{\mathrm{fast}} \approx I_{\mathrm{slow}} - I_{\mathrm{slow}} \times 0.9^2 = 0.19 I_{\mathrm{slow}}$

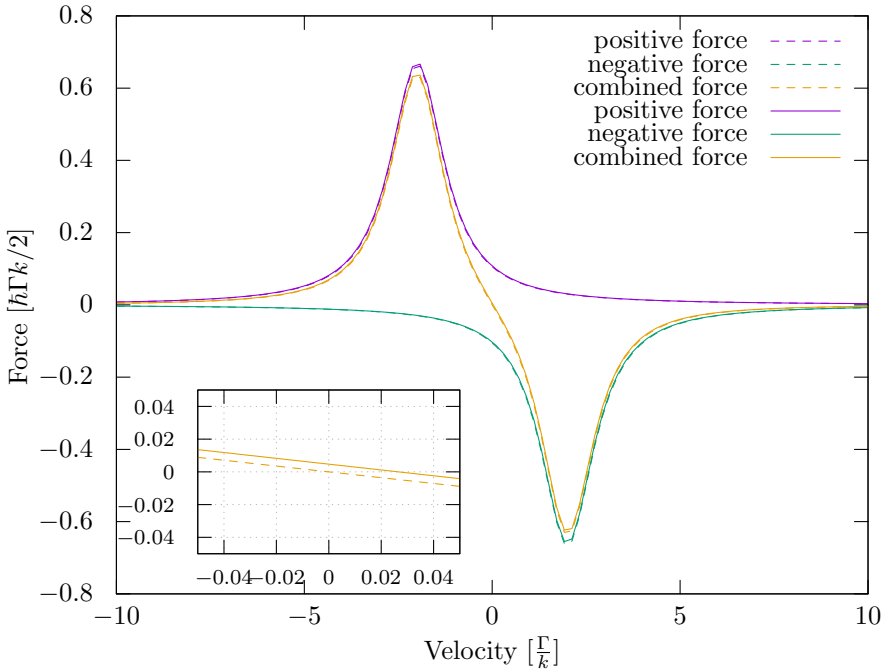

Figure 5.3: Molasses force for intensity variation of ±2.5% in opposing beams (solid lines). Dashed lines show Doppler force for balanced intensities. Figure assumes a nominal 3D MOT intensity of $2I_{\text{sat}}$ and detuning from resonance $\delta = 2\Gamma$.

Fig. 5.3 illustrates the effect of intensity imbalance for the fluctuations measured above. In the worst case scenario where opposing beams have drifted in opposite directions there is an intensity imbalance of ∼5%. This leads to a residual force as the atoms approach zero velocity of $\sim 2.5 \times 10^{-3}\hbar\Gamma k$, misaligning the magnetic centre and zero velocity region and weakening the cooling effect.

For launching atoms in a fountain the residual force imparts a horizontal acceleration on the atoms of ∼500 ms^{-2}. If the atoms spend 10 ms traversing the trap beams while they're launched they accumulate a horizontal velocity kick of ∼5 ms^{-1} causing all atoms to collide with the vacuum walls before a measurement can be made. This is an exaggeration because the actual mechanisms and forces acting upon the atoms are slightly more subtle, but it highlights a real problem.

The results presented above were achieved with a very well controlled input polarisation to the fibre system. In reality the alignment control we had with custom built waveplate mounts for the lasers was much more coarse and so it was prudent to test the quality of the light emerging. A result from placing a photodiode at the output of the 3D MOT telescope and monitoring the intensity is shown in Fig. 5.4.

One can see that the intensity fluctuations are large and this is problematic for atom number, temperature and launching. Intensity variations of the laser itself were tested and found to be negligible, highlighting the

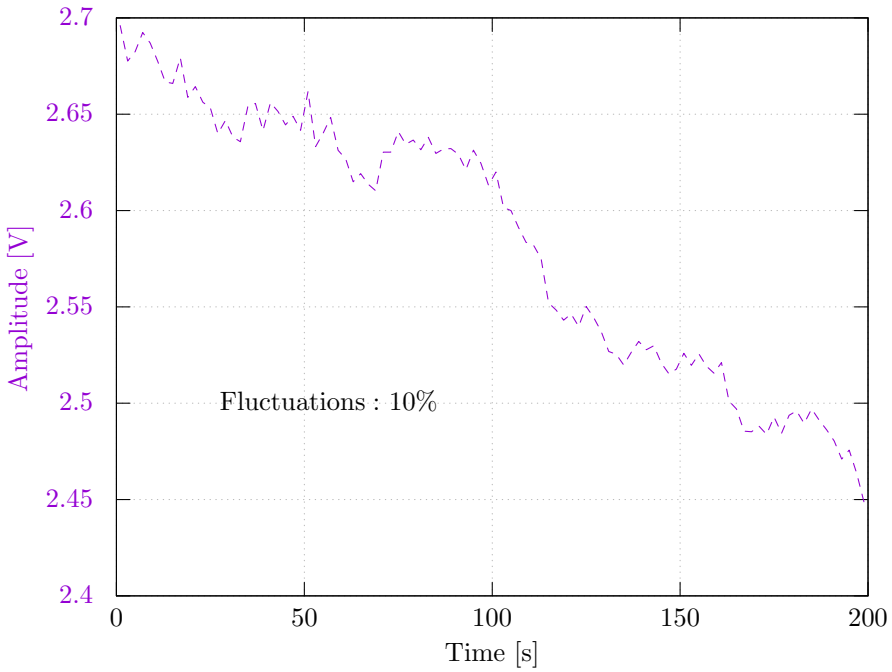

Figure 5.4: Light intensity following a polariser aligned to the fibre polarisation axis in a 3D MOT telescope as a function of time. An intensity drift of 10 % is apparent over the measurement period of 200 s.

lack of polarisation control as the real issue causing the effects of Fig. 4.1.

AOMs

The AOMs in the system serve a dual purpose of being used for frequency control of MOT beams and as fast shutters. Shown in Figs. 5.5 and 5.6 are the responses of the light when the AOMs are used as a switch.

Fig. 5.5 shows the response of the light turning off when the RF signal powering the AOM is stepped to 0 amplitude. There is a delay of $\sim$ 650 ns before the light begins switching. This is easily explained with typical acoustic velocities of $\sim$7000 m/s for a lithium niobate crystal [84] and a crystal length $\sim$5 mm.

Fig. 5.6 shows the response of the light turning on when the RF signal powering the AOM is increased from 0 to full amplitude. Again there is a delay of $\sim$ 650 ns before the light begins switching which suggests that the switching response is symmetric. This delay is a small problem in the timing of experimental sequences as there is a small lag on light turning on/off which must be accounted for.

Zooming in on the above traces allows one to examine the rise/fall times of the light. Again this is symmetric and on the order of 55-60 ns meaning very rapid adjustment of the light field intensity can be achieved.

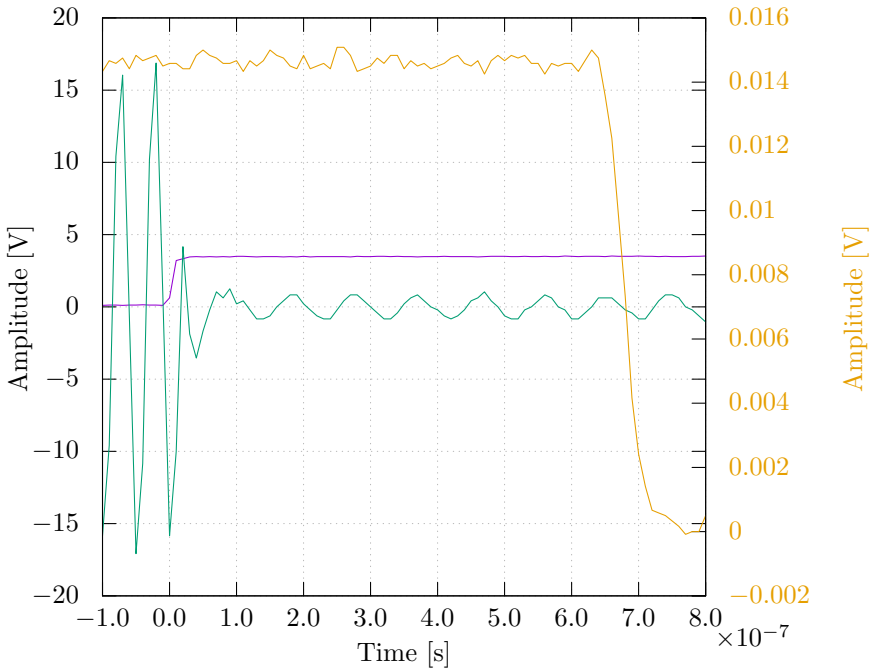

Figure 5.5: *Green:* 80 MHz RF signal generated by DDS driving the AOM. *Purple:* 3.3 V TTL signal generated by digital output channel of FPGA board to trigger RF-switch. *Yellow:* Response of light field as measured by a photodiode.

Mechanical Switches

While the AOMs are used for fast switching of the light field, they do not provide perfect extinction and for this reason mechanical fibre switches are also included. It was expected before testing that these devices would be considerably slower at switching than an AOM as they use moving parts to deflect the light into a fibre. Data recorded for the pusher/detection switch is shown in Fig. 5.9.

In terms of timing there is around a 3 ms delay between the TTL triggering the switch and the response. Once the switching starts it takes $\sim 1\ ms$ for the light in output 1 to extinguish but ~ 5 ms for the light in output 2 to settle. The power in output 2 settles at a power that is not the peak suggesting that the mechanical alignment inside the switch is not perfect for this output. This is possibly related to the settling time if there is some spring force that causes the alignment to slowly drift away from the correct alignment.

At the second TTL slope there is some even stranger behaviour. There is a small oscillation of the output powers suggesting that the switch overshoots its position and bounces back into the correct place. This lengthens the time needed for the switch to reach a steady state and must be taken into consideration when switching is done in experimental cycles to allow for long enough switching times.

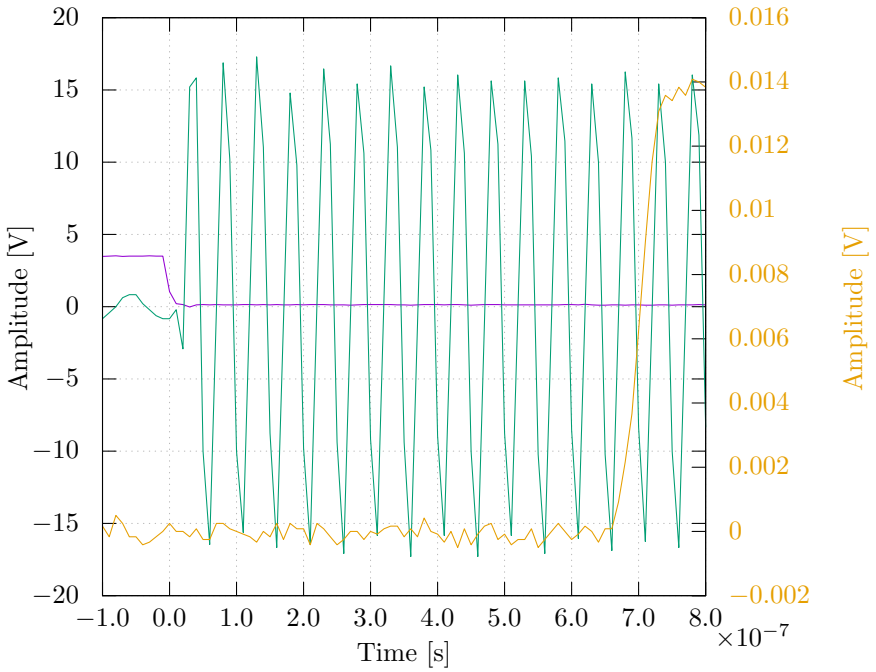

Figure 5.6: *Green:* 80 MHz RF signal generated by DDS driving the AOM. *Purple:* 3.3 V TTL signal generated by digital output channel of FPGA board to trigger RF-switch. *Yellow:* Response of light field as measured by a photodiode.

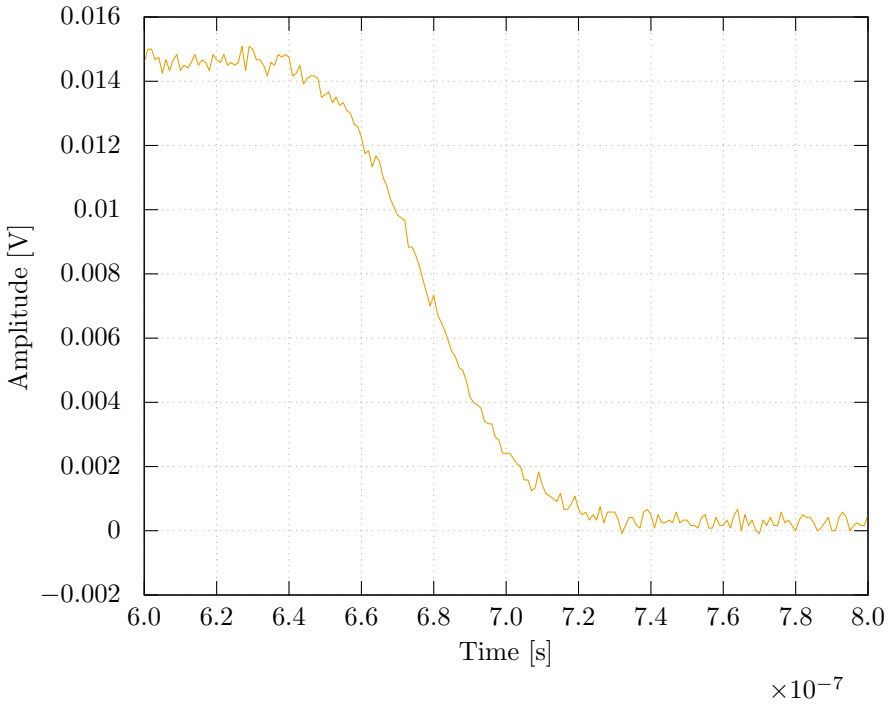

Figure 5.7: Zoomed region showing fall time of light field when RF power driving AOM is disabled.

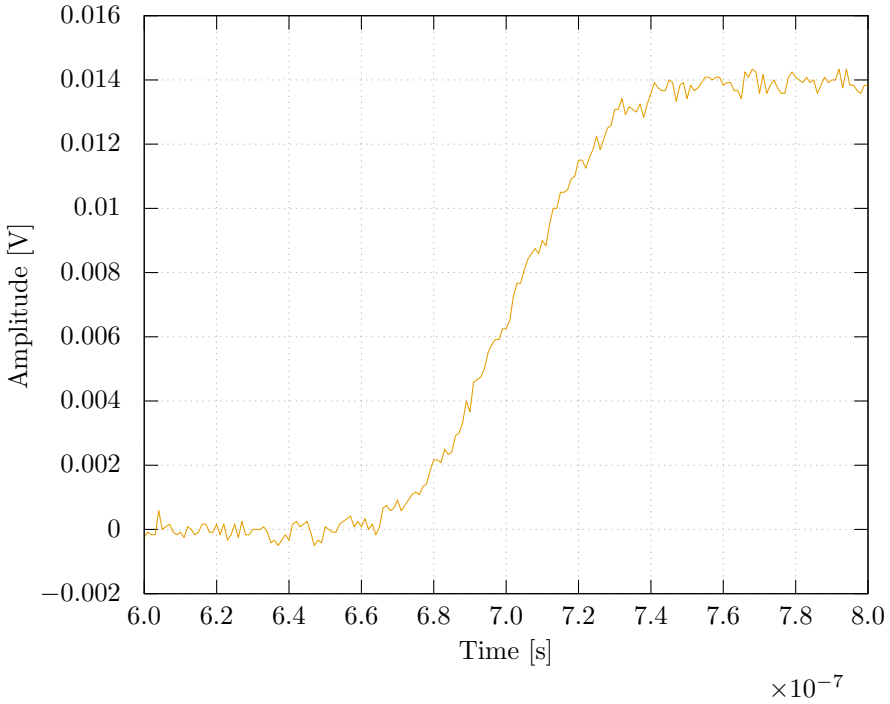

Figure 5.8: Zoomed region showing fall time of light field when RF power driving AOM is enabled.

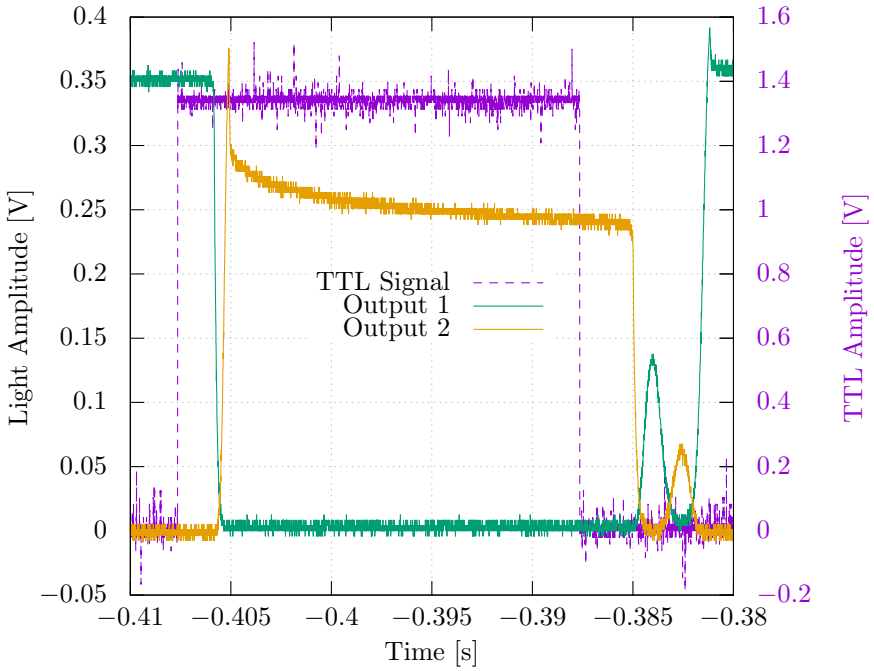

Figure 5.9: *Purple:* TTL signal generated by digital output channel of FPGA board to trigger fibre-switch. *Green:* Response of light field as measured by a photodiode for output port 1. *Yellow:* Response of light field as measured by a photodiode for output port 2.

Manufacturer	Expected PER (dB)	Measured PER (dB)	Error Bounds (dB)
Oz Optics	>33	37.2	36.90-37.43
Schäfter + Kirchoff	>30	33.18	33.06-33.30
Thorlabs Patch	>20	22.36	22.29-22.43
Thorlabs Custom	>27	23.67	23.35-23.99

Table 5.5: Polarisation extinction for a stressed fibre from different manufacturers. All fibres were 2 m FC/APC PANDA patchcords.

Baseline	Mating Fibre	Measured PER (dB)	Error Bounds (dB)
Oz Optics	-	33.54	32.70-34.38
	Oz Optics	28.11	27.47-28.75
	Thorlabs Custom	14.72	14.50-14.94
	Schäfter + Kirchoff	16.37	15.94-16.79
Schäfter + Kirchoff	-	33.18	33.06-33.30
	Oz Optics	18.62	16.49-20.38
	Thorlabs Custom	20.64	20.03-21.25
	Schäfter + Kirchoff	17.28	16.92-17.63
Thorlabs Custom	-	23.67	23.35-23.99
	Oz Optics	9.94	8.75-11.12
	Thorlabs Custom	9.10	8.94-9.26
	Schäfter + Kirchoff	10.61	10.56-10.66

Table 5.6: Polarisation extinction for a stressed fibre from different mating connections. All fibres were 2 m FC/APC PANDA patchcords.

5.2 Comparison of Fibre Manufacturers

For debugging and further development of a fully integrated fibre system, 2 m patchcord fibres from several manufacturers were tested to assess their ability to maintain polarisation along the incident axis. Tab. 5.5 shows the expected vs. measured PERs from different manufacturers.

What is clear is that the ability of fibres to maintain incident polarisation depends heavily on the manufacturer and depending on requirements one should take care what one purchases. Disregarding this fact, Tab. 5.5 highlights that, individually, every fibre tested exceeds the PER displayed by the assembled fibre system of Tab. 5.4. The only fibre found to perform below manufacturer specification was the custom patchcord from Thorlabs and this was the best fibre out of a batch of five.

There are two commonly used methods for connecting the vast array of fibre components needed for the experiment; mating with bulkhead adaptors and fibre splicing. Data were taken to assess the viability of bulkhead mating and are presented in Tab. 5.6.

In each test the baseline fibre was first optimised to give the highest possible PER with the fibre output connected to the polarisation analysis setup. Once optimised the output connector was connected to a securely

Component	Measured PER (dB)	Error Bounds(dB)
AOM1	15.78	15.31-16.71
AOM2 w/ 1 splice	17.19	17.11-17.27
AOM3 w/ 2 splices	14.81	14.19-15.43
Switch Ch1	18.18	17.24-19.05
Switch Ch2	21.17	19.40-22.42
Splitter Port 1	21.26	20.70-21.83
Splitter Port 2	17.20	16.63-17.80
Polarising fibre	27.67	27.61-27.73

Table 5.7: Polarisation extinction for integrated components.

mounted bulkhead mating sleeve where test fibres were also connected. In some agreement with Tab. 5.5 there are certain differences between the quality of fibres from different manufacturers. Unanimously there is degradation in PER when a second fibre is connected making mating sleeves a poor choice to connect many components. Based on mechanical tolerances of the fibre keys and the bulkhead key-width the maximum angular misalignment of the two fibres is on the order of 3°. From Eq. 5.1 this corresponds to a PER of $\sim$ 25 dB.

Of the tested fibres the most interesting result concerns the fibres from Oz Optics. They were the only fibre tested that when connected to each other maintained reasonable PER in agreement with the theory. In comparison, the fibres from Oz Optics and Schäfter + Kirchoff showed PERs $\gtrsim$ 30 dB individually but when connected only showed $\gtrsim$ 16 dB. This is not explained by angular misalignment between the keys so must be indicative of fibre-to-key alignment tolerances from different manufacturers.

5.3 Comparison of Integrated Components

Tab. 5.7 details the testing of several fibre-integrated components used in the fibre system. Data revealed relatively large polarisation fluctuations at the output of the AOMs giving at best 2% fluctuations in intensity. It has been shown that certain fibres (Tabs. 5.5 and 5.6) exhibit polarisation fluctuations even when injected with well controlled polarisation. One can therefore imagine that the propagation of the fluctuations caused by the AOM will only worsen at any connection between two fibres. For this reason the AOM outputs with spliced fibres were tested. The results were promising showing no real degradation in PER.

A polarising fibre from iX Blue was tested as an alternative to the polarising plate contained in the 3D MOT telescopes. The measured PER of 27.7 dB is in good agreement with the specification of $>$ 30 dB but was limited by the intensity noise of our detector due to the low output power.

Number of Splices	Measured PER (dB)	Error Bounds (dB)
0	36.22	30.37-38
1	33.74	29.02-38
2	35.37	29.99-38
3	31.49	27.64-38
4	29.59	26.37-34.75

Table 5.8: Polarisation extinction for a stressed fibre with splices. Error bounds are large from the uncertainty in angle of the fibre key following reinsertion.

5.4 Fibre Splice Analysis

A fibre patchcord was used for characterisation of polarisation changes due to spliced connections. First the PER for the base fibre was measured by injecting a well defined linear light source into the fibre and measuring the output. Once the fibre had been characterised it was cut and respliced several times (each time making a new splice) to study the effect of having multiple splices in a single path. The results of this test are summarised in Tab. 5.8

The data shows a negative trend for PER as one would expect with an increasing number of splices. The key result is that even after 4 splices the fluctuations in polarisation (and hence intensity) are at the $\sim 0.1\%$ level. This is a considerable improvement over the mating connectors presented in Tab. 5.6 and removes any doubt on splices causing the fluctuations found in Tab. 5.4.

The error bounds on this data represent extremal values and are large because of the method used for obtaining the data. In an ideal scenario, the input connector of the characterised fibre would have remained connected while the splices were added. Unfortunately, due to physical constraints, the fibre had to be removed for each splice and so the error stems from the angular misalignment when reinserting the fibre as specified in the mechanical tolerances of Tab 5.1. For an Oz Optics fibre there is a maximum difference between key and key width of 0.09 mm which corresponds to $\sim 1.7^\circ$ of angular freedom and is taken as the error. An upper error limit of 38 dB is enforced by the polariser used for analysis at the output of the fibre.

5.5 Investigating Improvements to Polarisation Fluctuations

The results obtained in Tab 5.4 were achieved with a well controlled input polarisation and hence represent an upper limit to the quality of the output polarisation. The worst telescope output recorded shows intensity fluctuations on the order of 5%. Referring back to Fig. 5.4 one can see that intensity fluctuations are a factor of 3 higher from which one might conclude that the input polarisation during measurements was not optimal.

Fibre	PER (dB)	Error (dB)	PER w/ Polarising fibre (dB)	Error (dB)
OZ Optics	2.82	0.26	16.51	0.48
Thorlabs	0.80	0.18	7.25	0.08
AOM	7.00	1.00	17.78	1.80

Table 5.9: Polarisation extinction for a stressed fibre with imperfect polarisation alignment with and without polarising fibre.

Returning to Tab. 5.4, an intensity fluctuation of 5% is still higher than one would want for atom trapping and launching, especially in this case where μrad precision in the verticality of the launch is the aim. Ideally one would want the beam balance to be stable to $< 1\%$.

A polarising fibre from iX Blue was used to address the issue of polarisation. The fibre works in a similar manner to a PM fibre and in-line polariser but in this case any light with a polarisation vector which is not along the stressed axis will be attenuated heavily along the entire length of the fibre. The key difference is that with a PM fibre and polariser one converts polarisation fluctuation into intensity modulation. Whilst this is true for the polarising fibre, the fact that intensity is lost over the entire length of the fibre means that at the output the fluctuations are minimal (only the correct polarisation has been guided) at the expense of the overall intensity.

An intentionally unoptimised polarisation system was used to test the effect of the polarising fibre and data were recorded for different patch fibres with and without the polarising fibre as shown in Tab. 5.9.

For reference, an angular misalignment of 10° would give a PER of ~ 15 dB (from Eq. 5.1) demonstrating that the tested components were truly misaligned. Addition of the polarising fibre showed large improvements in all cases. A polarising fibre at every output of the fibre system and careful control of the input polarisation should bring intensity fluctuations to $< 1\%$ however this was not fully verified. A quick test with one output of the fibre system with an unoptimised input showed an improvement from 8.21 dB (15% matching Fig. 5.4) to 15.10 dB (3%) with the inclusion of the polarising fibre.

From the results presented above and earlier in this chapter it would suggest that fibre components are not inherently terrible and with the inclusion of a fibre polariser we can correct for a large percentage of the fluctuations. The poor performance of the fibre system used to originally generate the trapping light must be attributed to poor design choices and careless assembly. For this reason we expect an all-fibre solution to work if one carefully selects the components used and pays high attention to how they are connected together. As a proof of principle we have replaced the Raman laser in our experiment with a fully fibre-integrated solution and used this to perform fringe measurements which will be presented in the following chapters. Following the outcome of the Raman laser integration it may be decided to reattempt a fibre approach for MOT light.

CHAPTER 6

FREQUENCY DOUBLED LASER SOURCE FOR RUBIDIUM COLD ATOM EXPERIMENTS

The use of frequency doubled laser sources is not uncommon in cold atom experiments [85–87]. In recent years there has been particular interest in the use of telecom laser components for laser cooling Rubidium as the frequency band of telecom is conveniently half of the Rubidium excitation frequency. Using such components presents several advantages, namely that the telecom industry is well established and the components are rigorously tested allowing one to obtain high quality tools for a reasonable price. In addition to this, it is possible to develop very powerful, low linewidth laser sources that are relatively compact which is of interest here for the future of compressing the size of the experiment.

This chapter is focused on the design and theory of compact telecom laser systems and will start by introducing the system that has been developed as part of this work. Included will be the theory of light modulation for generating multiple frequencies along with the second harmonic generation technique used to produce the necessary frequency for laser cooling. Information on the future development of the laser will be presented which includes the proposed method of frequency stabilisation and advanced modulation techniques. The Pound-Drever-Hall [88] method for stabilising the laser frequency will be discussed in some small detail and designs for the development of a single laser system capable of delivering all the required frequencies for an atom interferometer will be presented.

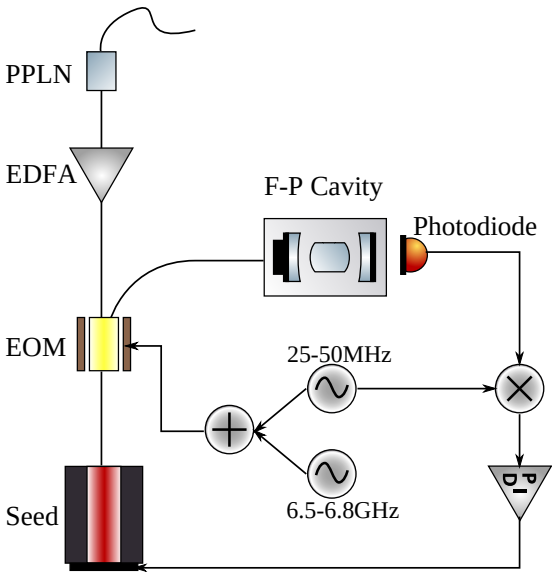

Figure 6.1: Frequency doubled laser system for atomic cooling or Raman beams. A secondary laser frequency is generated by modulating an EOM at the required frequency of 6.5 GHz for cooling & repumper or 6.8 GHz for Raman I & Raman II. An additional modulation is included for PDH locking and part of the light is split off for locking to a Fabry-Perot cavity. The remainder of the light is amplified and undergoes second harmonic generation.

6.1 Single Laser for Atom Trapping or Raman Transitions

The motivation for moving towards a single laser system to provide either trapping or Raman light is driven by the application nature of this project. Most cold atom experiments employ a master-cooler-repumper laser configuration as explained in chapter 3. For making a transportable and robust system, having three separate lasers along with control electronics for each increases redundancy and size. In principle, it is possible to use a single laser in conjunction with frequency modulation to generate the desired laser frequencies and such a system is described here.

Shown in Fig. 6.1 is the system that has been developed for either laser cooling or atom interferometry in the form of Raman beams. 20 mW of 1560 nm light is generated by an NKT Photonics Koheras Basik fibre laser which is then passed into a Photline 10 GHz Electro-optic Modulator (EOM). 1% of the light exiting the EOM is picked off for laser frequency stabilisation, the remaining 99% enters an NKT Photonics Boostik EDFA where the optical power is amplified up to 1 W. The final step is to pass the 1560 nm light through a periodically-poled Lithium-Niobate (PPLN) waveguide which doubles the frequency of the light through second harmonic generation of photons.

6.1.1 Modulation of Light

In order to obtain the required frequencies for either laser cooling or Raman interferometry from a single laser one must modulate the light in some way. Here the modulation is done by modulating the phase of the light with two different sinusoidal frequencies. The first of these frequencies is on the order of a few 10s of MHz and is used for stabilisation of the laser frequency which will be discussed later. The second modulation is driven by either a 6.834 GHz oscillator (corresponding to the hyperfine ground state splitting) for the Raman beams or a ≈ 6.6 GHz oscillator (roughly the difference between cooling and repumping frequencies) for laser cooling.

Starting from a monochromatic laser beam of frequency ω, the electric field can be written as:

$$E(\omega, t) = A\mathrm{e}^{i\omega t} \tag{6.1}$$

One now introduces a modulation at frequency Ω and modulation depth m. The phase modulated output can hence be written as:

$$E(\omega, t) = A\mathrm{e}^{i(\omega t + m\cos\Omega t)} \tag{6.2}$$

If the modulation amplitude is small then this simplifies and one can write an approximation:

$$E(\omega, t) \approx A\mathrm{e}^{i\omega t}(1 + im\sin(\Omega t)) \tag{6.3}$$

Switching to the exponential form of sine allows this to be rewritten as:

$$E(\omega, t) = A\mathrm{e}^{i\omega t}\left(1 + \frac{m}{2}(\mathrm{e}^{i\Omega t} - \mathrm{e}^{-i\Omega t})\right) = A\left(\mathrm{e}^{i\omega t} + \frac{m}{2}(\mathrm{e}^{i(\omega+\Omega)t} - \mathrm{e}^{i(\omega-\Omega)t})\right) \tag{6.4}$$

Here one can see that there are three oscillating fields; the carrier at frequency ω and two sidebands at frequency $\omega \pm \Omega$. Only the first order terms have been shown here, in reality there are an infinite number of sidebands at multiples of the modulation frequency but they have sufficiently small amplitude that they can be neglected.

6.1.2 Frequency Doubling

Using a 1560 nm seed laser for this experiment requires that the frequency is doubled (wavelength halved) before it is useful for laser cooling or Raman transitions. For this reason a non-linear crystal operating under

second harmonic generation is used [89].

Light passing through the doubling medium causes the atoms to oscillate like dipoles as they absorb and re-emit. It is possible that the light will drive these oscillations such that a non-linear response from the medium is induced and the atoms re-emitting light will emit additional frequencies. The material used here, PPLN, is particularly prone to second order non-linear effects.

A second order effect non-linear effect involves the mixing of three electromagnetic waves. The particular process of mixing here is second harmonic generation (SHG) where two input photons produce a single photon of twice the frequency.

$$\lambda_{SHG} = \lambda_{\text{input}}/2 \qquad \text{or} \qquad f_{SHG} = 2f_{\text{input}} \tag{6.5}$$

An important quantity in frequency doubling is conservation of photon phase, also known as phase matching. For phase matching to work, the relative phase between the different light frequencies must be fixed as they propagate through the medium else destructive interference will occur. However, the refractive index of the material is frequency dependent and so in a bulk crystal there is a phase shift of π between the fundamental and generated frequency over a distance defined by the coherence length:

$$l_c = \lambda/4(n_2 - n_1) \tag{6.6}$$

where λ is the fundamental wavelength and n_i are the wavelength-dependent refractive indices of the crystal.

To circumvent the phase matching problem, a technique of quasi-phase-matching [90] is employed by periodically poling the doubling medium. By inverting the crystal domains at distances of multiples of π phase shift the destructive interference is lessened and a greater power in the harmonic frequency is observed as shown in Fig. 6.2.

6.1.3 Laser Stabilisation

The laser was locked to a scanning Fabry-Perot cavity at 1560 nm using the technique of Pound-Drever-Hall (PDH) [88]. The decision to use this method over the more traditional method of spectroscopy locking the frequency doubled component to a Rubidium transition was made to allow for extinction of the 780 nm light without losing the laser lock. It is perfectly possible to realise a system with a spectroscopy lock and have light extinction but this requires additional splitting and switching components which lower overall

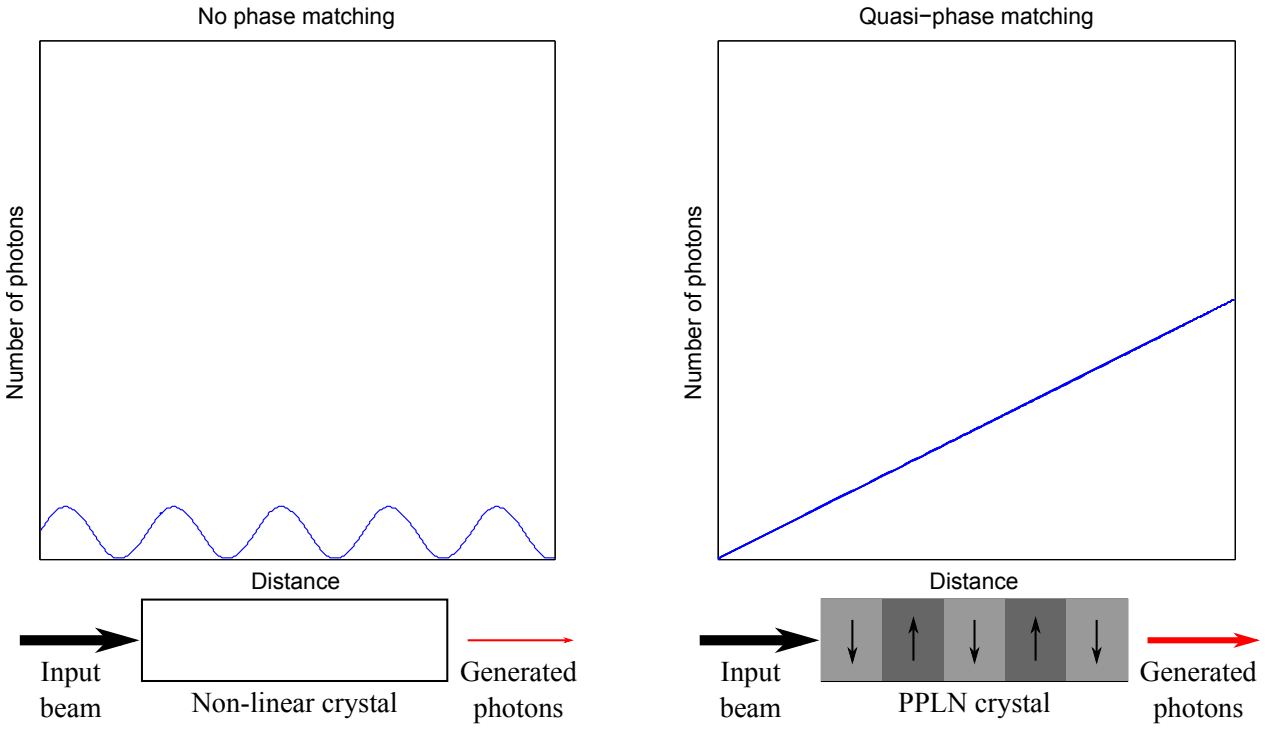

Figure 6.2: Comparison of number of generated photons between a standard non-linear crystal and a PPLN crystal. By periodically poling the crystal domains destructive interference from accumulated phase delay is lessened and a regime of quasi-phase matching is observed. In this regime the number of generated photons increases with the length of the crystal.

robustness and available laser power at the experiment. An additional benefit of cavity locking is that it allows one to block the light before the frequency doubler and use this as an additional attenuator due to the intensity dependence of doubling.

Fig. 6.1 shows the locking scheme used. Traditional PDH uses the reflected component of the cavity light field for a faster response however the fibre-coupled cavity used here allowed only for the transmitted component to be detected. In this case, the laser frequency is locked to the side of a transmission fringe.

6.2 Towards a Single Laser for Atom Interferometry

Outlined in the previous sections are techniques to develop a stabilised laser source to be used for either laser cooling or Raman transitions. The focus of this section is to take the previously mentioned technology and build a single laser system that can act as *both* the cooling and Raman lasers. This type of experimental setup is driven by our application and the need to have a compact and portable setup. To achieve this, one requires a method of shifting the central frequency of the laser by some GHz within some ms time window.

6.2.1 Serrodyne Modulation Technique

Shifting the frequency of a laser is useful in many atomic physics experiments. Here the goal is to have a laser tuned to cooling frequency which can rapidly be tuned to the Raman frequency. The traditional approach of using an AOM to shift the frequency is undesirable. Whilst they can shift frequencies by $\approx 30 - 2500$ MHz, their tuning range about their central frequency is typically limited to $\approx \pm 10\%$ which would limited the flexibility in frequencies we desire. EOMs allow one to transfer power from the central frequency into sidebands at $\pm$ the modulation frequency which can be tuned over a wide range but the amount of power transferred is limited by a first order Bessel function at $\approx 33\%$ when driven sinusoidally.

Driving an EOM with a linear ramp in principle shifts the laser frequency by an amount proportional to the ramp, the time derivative of the phase of a signal defines its frequency. However, generating a long linear signal with a sufficient slope is electronically challenging. Instead one can employ the technique of sawtooth (serrodyne) modulation which at high frequencies mimics the response of a linear ramp - the linear phase shift of sawtooth results in fixed frequency shift proportional to the slope [91]. The extent to which a serrodyne signal mimics a linear ramp depends on the bandwidth of the driving signal, a high bandwidth signal is desirable to minimise oscillations at the discontinuity in the sawtooth. A limitation arises from the fact that any physical sawtooth waveform has a finite fall-time which creates a periodic discontinuity in the phase of the serrodyne optical signal in the time domain and results in harmonic spurs in the frequency domain. For this reason the technique of serrodyne modulation cannot be 100% efficient.

In this experiment, the serrodyne signal is generated by driving a non-linear transmission line (NLTL) with a sinusoid of the desired sawtooth frequency (Fig. 6.3. This technique allows us to generate sawtooths from $0.2 - 1.2$ GHz. An NLTL is made up of a ladder of inductors and voltage dependent capacitors. It is these capacitors that give rise to the non-linearity of the device. When driven by a sinusoidally varying voltage, the higher voltage parts of the wave pass through the inductor-capacitor ladder quicker than the low voltage parts and hence the sine wave is distorted. The shape of the output sine wave looks remarkably similar to that of a sawtooth.

Light exiting a linearly modulated EOM has the form $E(t) = E_0 \cos(\omega t + \phi(t))$. Here, $\phi(t)$ corresponds to the linear phase ramp, $\phi(t) = (m\delta) \cdot t|2\pi m|$. The desired frequency shift is then given by $\dot{\phi}(t) = m\delta$ which has period $2\pi m$. Therefore what is required is a sawtooth with angular frequency δ and amplitude $2\pi m$.

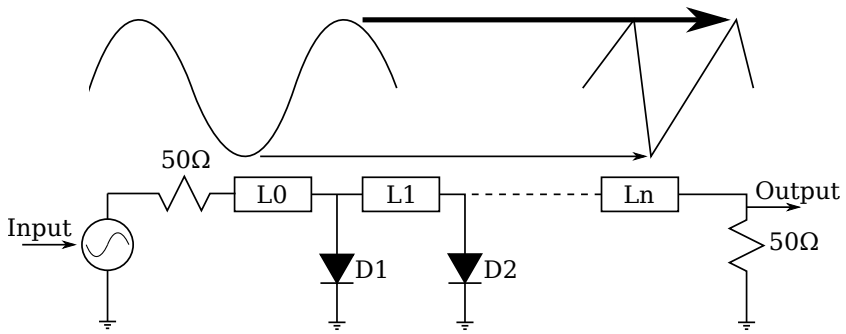

Figure 6.3: Illustration of the non-linearity effect in the NLTL arising from the voltage-variable capacitance of the inductors and diodes. This has the effect of distorting a sine wave such that the higher voltage parts pass through the device faster than the low voltage parts, forming a perfect sawtooth in an ideal case.

6.2.2 Fourier Analysis of RF Signals for Serrodyne Modulation

To better understand how the various RF signals interact with the laser system one can simulate the overall modulation by using the Fourier domain to combine the individual modulation frequencies. Such mathematics allow one to express a linear ramp (sawtooth), like that used for serrodyne modulation, as a sum of sines and cosines which makes it simpler to combine with the sinusoidal modulation being used for the PDH lock.

Fourier Series - Sawtooth Wave

A mathematical treatment for a generalised Fourier series can be found in any good mathematics textbook. Here the result for the particular case of a sawtooth wave will be used.

Treating a sawtooth like a string of length $2L$, fixed at one end and perturbed at the other has the form:

$$f(x) = \frac{x}{2L} \tag{6.7}$$

Hence the components of the Fourier series are:

$$a_0 = \frac{1}{L}\int_0^{2L} \frac{x}{2L}\mathrm{d}x \tag{6.8a}$$

$$= 1 \tag{6.8b}$$

$$a_n = \frac{1}{L}\int_0^{2L} \frac{x}{2L}\cos\left(\frac{n\pi x}{L}\right)\mathrm{d}x \tag{6.8c}$$

$$= \frac{[2n\pi\cos(n\pi) - \sin(n\pi)]\sin(n\pi)}{n^2\pi^2} \tag{6.8d}$$

$$= 0 \tag{6.8e}$$

$$b_n = \frac{1}{L}\int_0^{2L} \frac{x}{2L}\sin\left(\frac{n\pi x}{L}\right)\mathrm{d}x \tag{6.8f}$$

$$= \frac{-2n\pi\cos(2n\pi) + \sin(2n\pi)}{2n^2\pi^2} \tag{6.8g}$$

$$= -\frac{1}{n\pi} \tag{6.8h}$$

and so the Fourier series is given by:

$$\begin{aligned} f(x) &= \frac{1}{2} - \frac{1}{\pi}\sum_{n=1}^{\infty}\frac{1}{n}\sin\left(\frac{n\pi x}{L}\right) \\ &= \frac{1}{2} + \frac{i}{2\pi}\ln(-\mathrm{e}^{-i\pi x/L}) \\ &= \frac{1}{2} - \frac{1}{2\pi}\arg(-\mathrm{e}^{-i\pi x/L}) \end{aligned} \tag{6.9}$$

Plotting this formalism for several values of n is shown in Fig. 6.4.

Combining Sawtooth Waves with Fourier Series

To realise a large frequency shift of the laser frequency ($>$ 2GHz) it was necessary to combine multiple sawtooths as the highest frequency comb generator available to us could only drive 1.2 GHz sawtooths. Understanding how multiple sawtooth waves sum is useful for the next section where the effect of this on the PDH error signal is examined.

Fig. 6.5 shows the effect of summing two sawtooth waves of different frequencies that are perfectly in phase. As one might expect, the response of the sum is simply a linear modulation at the lower sawtooth frequency.

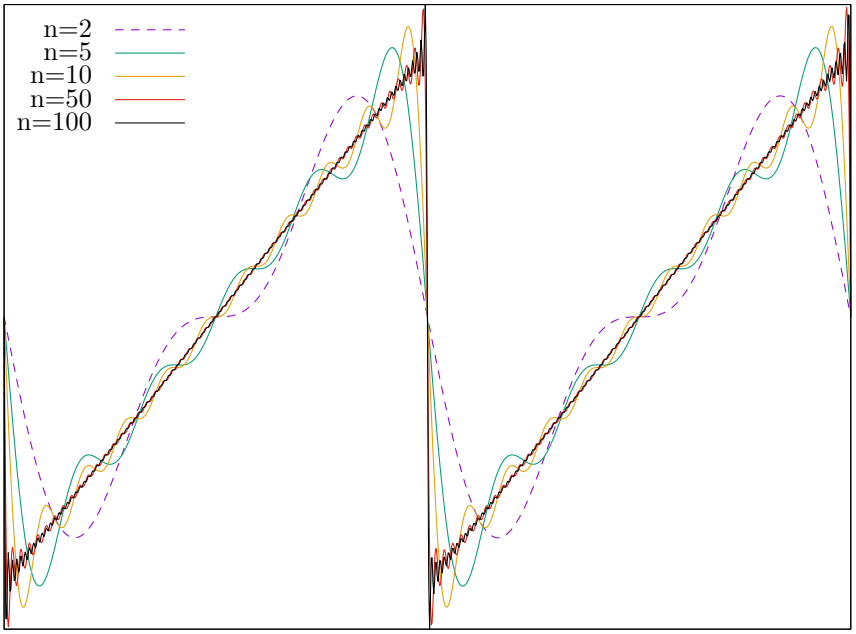

Figure 6.4: Fourier analysis of a sawtooth wave composed of sine waves for multiple values of n.

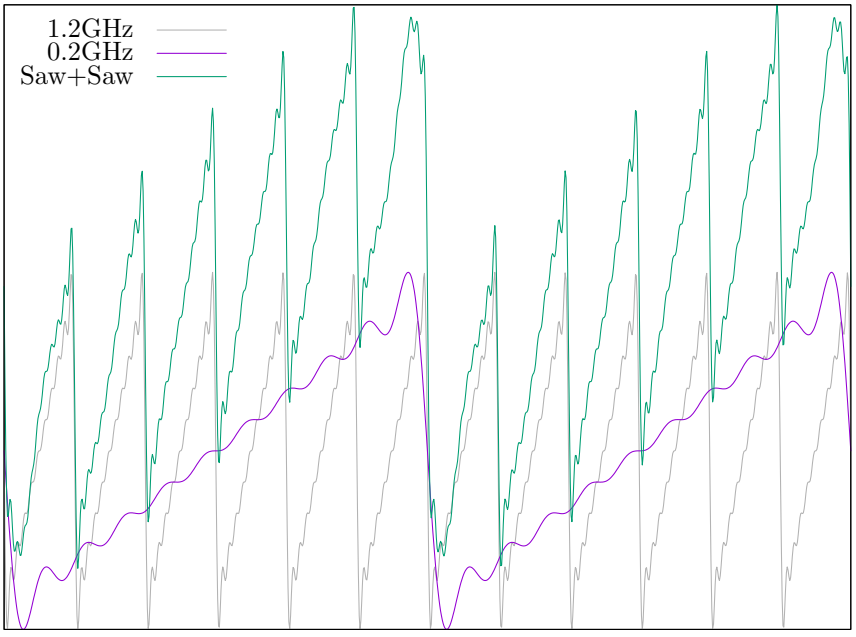

Figure 6.5: Theoretical output from summing two sawtooth waves of different frequencies for $n = 100$. The result is simply a modulation of the low frequency sawtooth with a higher frequency sawtooth.

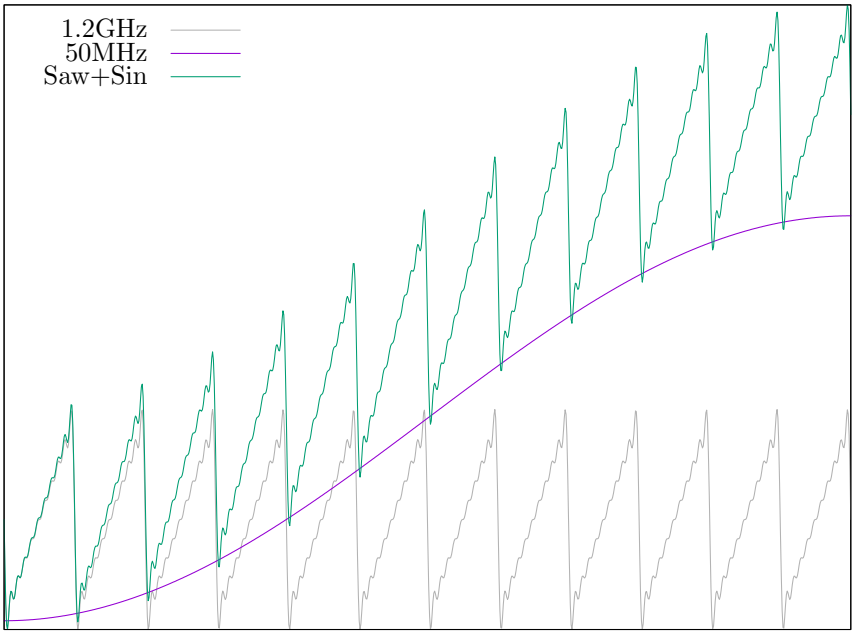

Figure 6.6: Theoretical output from summing two sawtooth waves of different frequencies for $n = 100$ and a sine wave. The result is simply a modulation of the low frequency sine with a higher frequency sawtooth.

Combining Sinusoidal and Sawtooth Waves

In the laser stabilisation arrangement outlined in the following section, the PDH modulation signal and serrodyne frequency shifting signal are incident on the same EOM. It is therefore useful to understand how this might affect the error signal one would normally get from a simple sinusoidally modulated PDH.

Fig. 6.6 shows that the signal from a sawtooth modulated by a low frequency sine wave. The important result of this section is illustrated by applying this signal to a typical PDH setup as shown in Fig. 6.7. Whilst this figure does not account for the amplitude that would be lost due to imperfect sawtooth shape, it shows that the entire signal is shifted in frequency space by an amount directly proportional to the applied sawtooth frequency. The lower frequency sidebands which are used in the PDH lock are also shifted by the same amount so the error signal retains the desired shape. It should therefore be possible to lock a laser to the slope of one of these error signals and jump frequency by several GHz to a new desired lock frequency as long as it is jumped between cavity modes. This idea has important consequences for the design of a single, agile laser design which is discussed towards the end of this section.

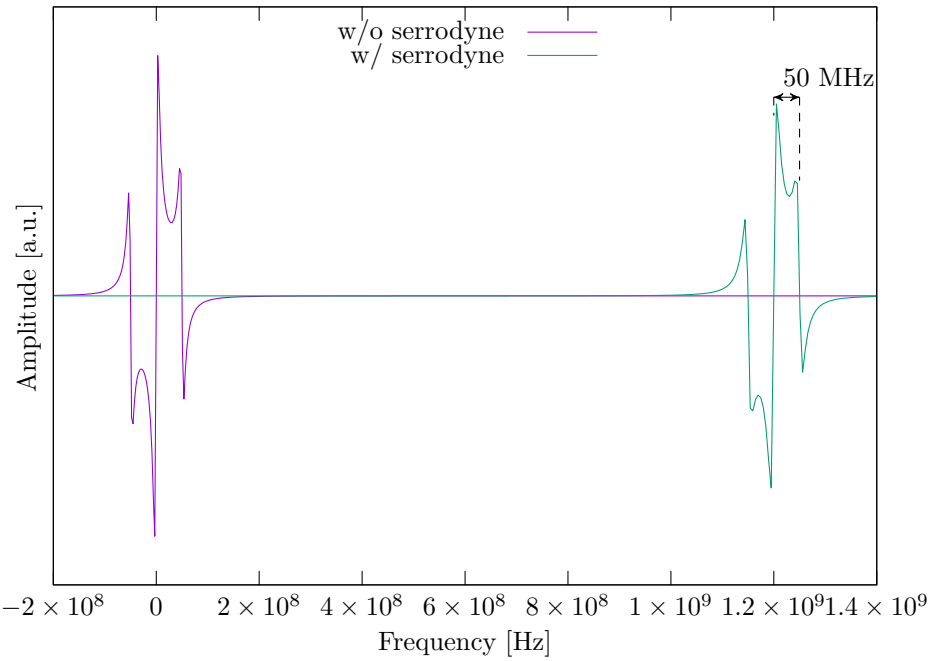

Figure 6.7: Simulated PDH signal with serrodyne modulation. The entire error signal is shifted by 1.2 GHz when a serrodyne signal of the same frequency is applied. This simulation assumes 80% efficiency in shifting associated with the imperfect skew of the sawtooth shape.

6.2.3 High Bandwidth and Large Dynamic Range Laser Lock

The simulations above suggest that stabilising the laser frequency via feedback to an external frequency shifting component is possible in this experiment. The motivation for including such a scheme was to circumvent the limited bandwidth of traditional piezo locking schemes. Whilst the piezo in this experiment has a tuning range of ≈ 4 GHz, the bandwidth is on the order of kHz. Using an EOM to frequency shift the light with the scheme detailed here, one can achieve a range of up to 10 GHz (limited by the EOM) and a bandwidth on the order of MHz [92].

6.2.4 Generation of Desired Frequencies

Serrodyne modulation has been mentioned multiple times in earlier sections as a technique for shifting the laser frequency. In the previous section it was used to stabilise the frequency of the laser as a fast lock but here it will be taken one step further. In order to realise a single laser source one must shift the central frequency of the laser by some GHz. Here serrodyne modulation will be used as in [93, 94] to achieve the shift.

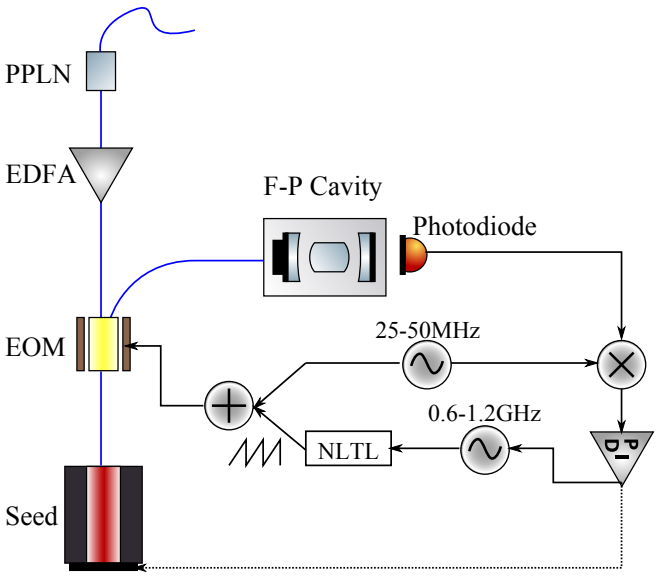

Figure 6.8: Laser frequency stabilised to a Fabry-Perot cavity via the technique of PDH using feedback to a VCO driving a serrodyne modulated EOM. An optional path is included to apply slow modulation to the laser piezo for temperature drifts.

Fig. 6.9 shows the setup used to achieve such a shift. After the seed laser, part of the light is split off to be used for stabilisation as in Fig. 6.8. The remaining light passes through 2 EOMs which can be switched on or off at the desired frequency shift using RF switches at the VCOs. This allows for a maximum of 2.4 GHz central frequency shift with a switching time on the order of μs. At the second EOM there is an additional frequency that can be mixed in corresponding to whether the laser is in cooling (6.5 GHz for repumper) or Raman (6.8 GHz hyperfine splitting) mode.

The drawback with such a system is the amount of components required - especially the number of expensive EOMs. Shown in Fig. 6.10 is the same system but with a single EOM. Such a system is realisable if one shifts the laser frequency by a multiple of the cavity free spectral ranges (1.5 GHz in this case) such that the lock can be maintained or quickly recovered.

6.3 Serrodyne Modulation

Serrodyne modulation is a powerful tool for realising a compact laser system with multiple frequency outputs. Work demonstrated in [92–94] highlighted the ability of a serrodyne-driven EOM to apply frequency shifts to the central frequency of a laser with high efficiency and bandwidth. From this it became possible to realise a laser that can deliver cooling, repumping and both Raman frequencies simply by sweeping the laser frequency

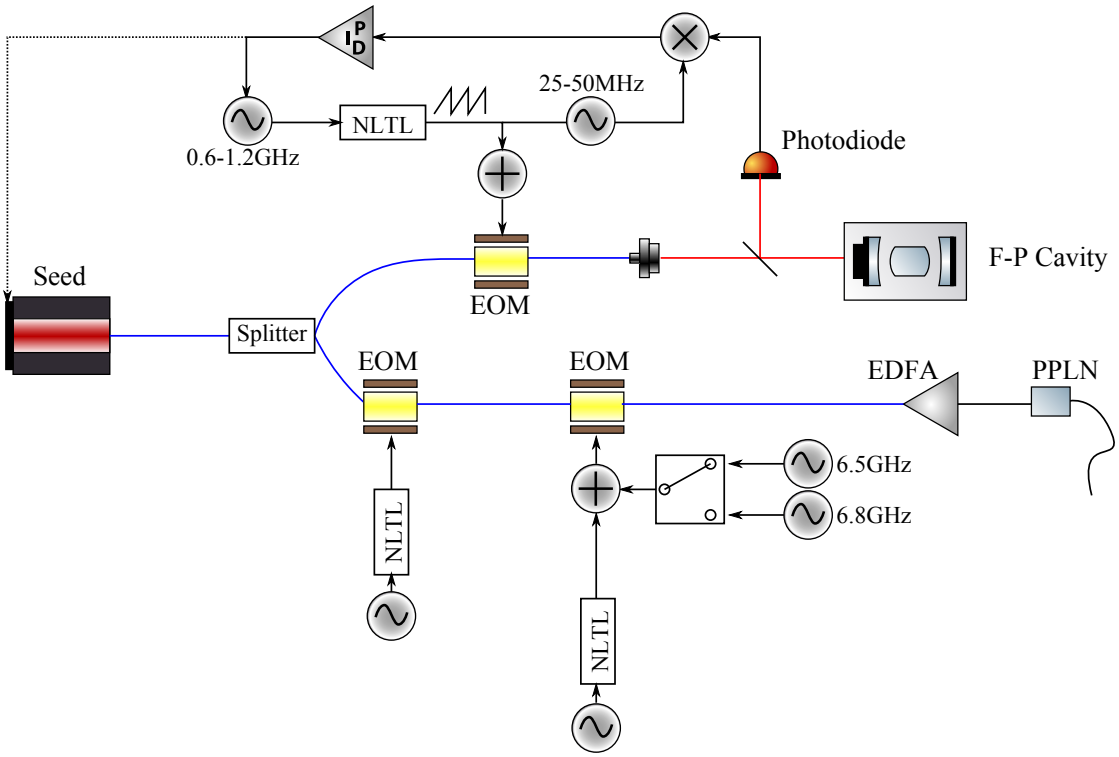

Figure 6.9: Single laser system for both laser cooling and Raman interferometry. The seed laser is split into two arms. The upper arm is used for frequency stabilisation via the serrodyne PDH lock of Fig. 6.8. The lower arm is used for frequency control of the light. The NLTLs driving the EOMs are used to shift the carrier frequency between cooling and Raman I ($\sim$ 2.4 GHz). An additional frequency is switched on the final EOM to provide the sideband for repumper (6.5 GHz) or Raman II (6.8 GHz).

via the EOM.

6.3.1 Sawtooth Characterisation

To achieve optimal frequency transfer with a serrodyne driven EOM, the driving signal must closely resemble a perfect sawtooth. When this is satisfied a high efficiency frequency shift will be realised with a magnitude proportional to the slope.

Data taken for an NLTL (Aeroflex MLPNC-7100) driven by an amplified (Minicircuits ZHL-2-12+) 150 MHz sinusoidal waveform (Novatech DDS8p) are shown in Fig. 6.11. For low driving amplitudes there is poor agreement to the theoretical shape, in particular for the downward slope gradient. One finds that as the amplitude is increased the agreement between downward slopes increases. For this particular NLTL the data suggests that the optimal driving amplitude is at the maximum signal that can be safely handled by the device. However this shows weird behaviour in the ramping slope where it appears to have a step-like

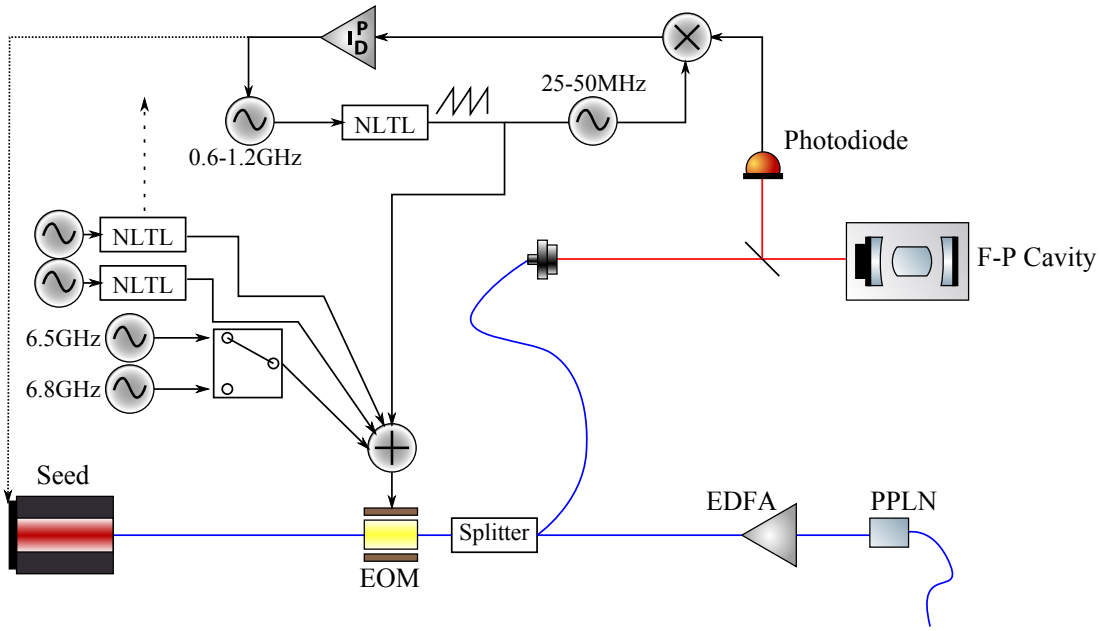

Figure 6.10: Single laser system for both laser cooling and Raman interferometry as described in Fig. 6.9 but combining all necessary frequencies and using a single EOM for modulation.

change in gradient.

Recall that the NLTL essentially consists of a linear series of inductors and semiconductor diodes which function as voltage-variable capacitors [94]. The shape of the generated sawtooths suggests that the voltage scaling is not functioning as intended. It is mentioned in [95] that the efficiency can be limited by voltage breakdown effects in the diodes but this has not been verified in this work. In addition to the discrepancy between real and generated sawtooth waves there is an extra modulation frequency on both the sinusoidal driving frequency and the generated sawtooth. The source of these ripples is unknown and still being investigated.

6.3.2 PDH Error Signal

Using the experiment presented in Fig. 6.8 the effect of a serrodyne signal on a PDH scheme was tested. The transmission signal from a Fabry-Perot cavity was first examined and is shown in Fig. 6.12.

Shown in green is the expected transmission signal for a light field frequency modulated by an EOM as in PDH. In this case, a 50 MHz local oscillator (LO) is used. The data shows a clear carrier peak and two smaller peaks spaced by 50 MHz from the carrier. There is an asymmetry in the form of a small bump on the peaks which is most evident on the carrier. It is believed to be caused by cavity alignment issues as the

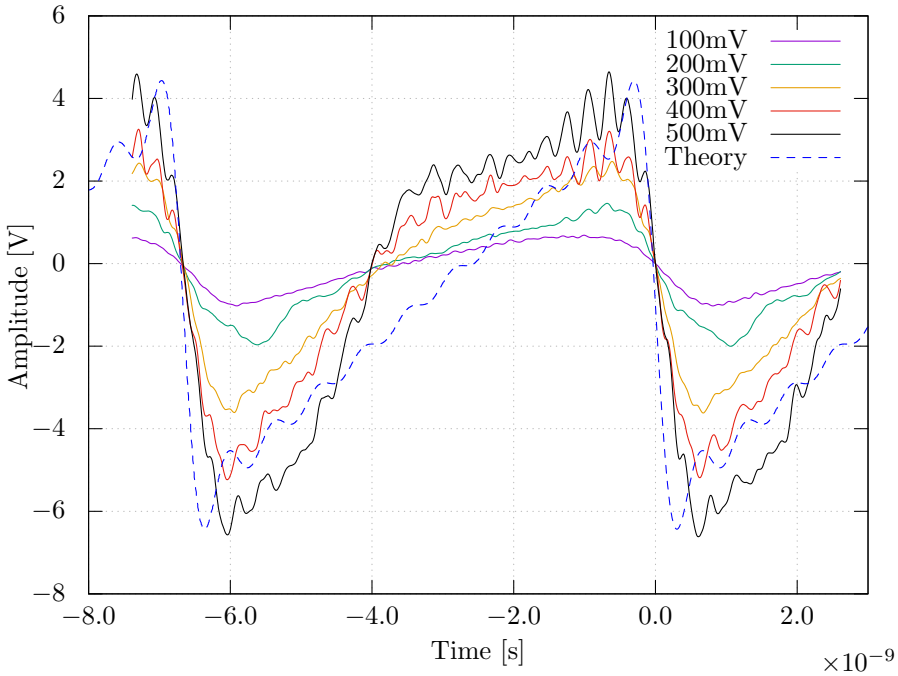

Figure 6.11: Sawtooth response of NLTL to sinusoidal driving frequency of 150 MHz for various driving amplitudes compared to a theoretical sawtooth made from a Fourier series of the first 10 terms.

setup was quickly engineered with a bulkhead fibre collimator.

Summation of the LO and a serrodyne signal (Aeroflex MLPNC-7103) by a broadband power combiner (Minicircuits ZFRSC-42+) at the EOM input generates the trace in purple in Fig. 6.12. A 1.2 GHz shift, in agreement with the serrodyne driving frequency, is observed. The transfer efficiency of this shift is ∼56% which is in good agreement with previous work by [93,94] (∼ 61%). The lower value recorded here is explained due to only having coarse control of RF amplitude with fixed attenuators.

Demodulation of the cavity transmission signal with the LO signal reveals the typical PDH error signal shown in Fig. 6.13 (Green). The asymmetry problems become more prominent in the error signal showing a kink at the zero crossing in the center of the trace.

Addition of the serrodyne signal again shows a frequency shift and decrease in amplitude however the efficiency appears to have decreased by at least a half. The exact reason for this is unknown but is likely due to electronics and phase matching. This is further motivated by the shape of the error signal when serrodyne is applied in that it picks up a considerable amount of noise.

Thus far it has been unsuccessful to lock a laser to such an error signal because of the size and noise generated. Attempts to clean the signal with bandpass filters were made but proved futile.

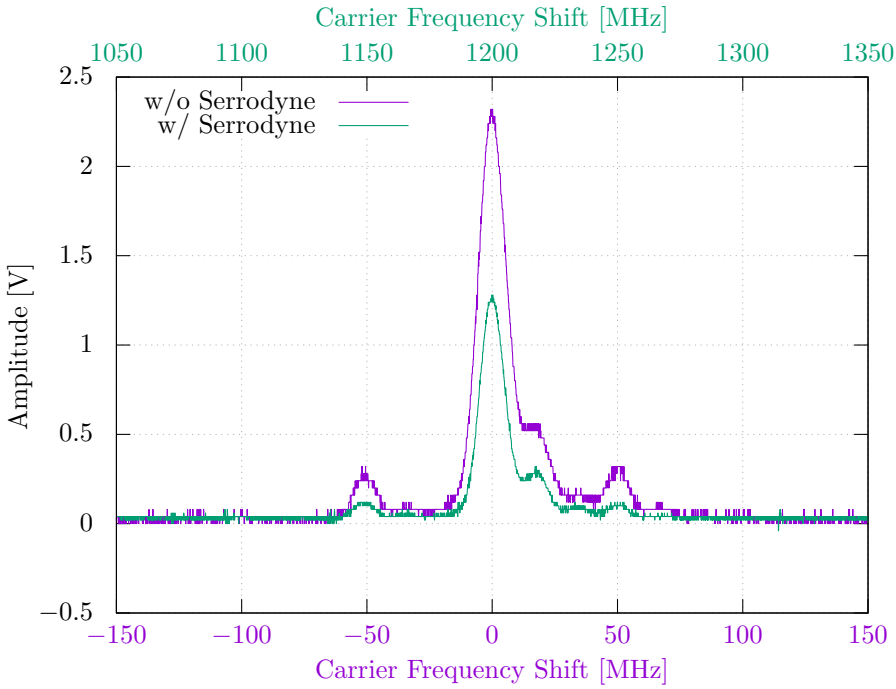

Figure 6.12: Purple: Fabry-Perot cavity transmission signal for laser field electro-optically modulated at 50 MHz. Green: same signal with additional 1.2 GHz serrodyne summed at the EOM input.

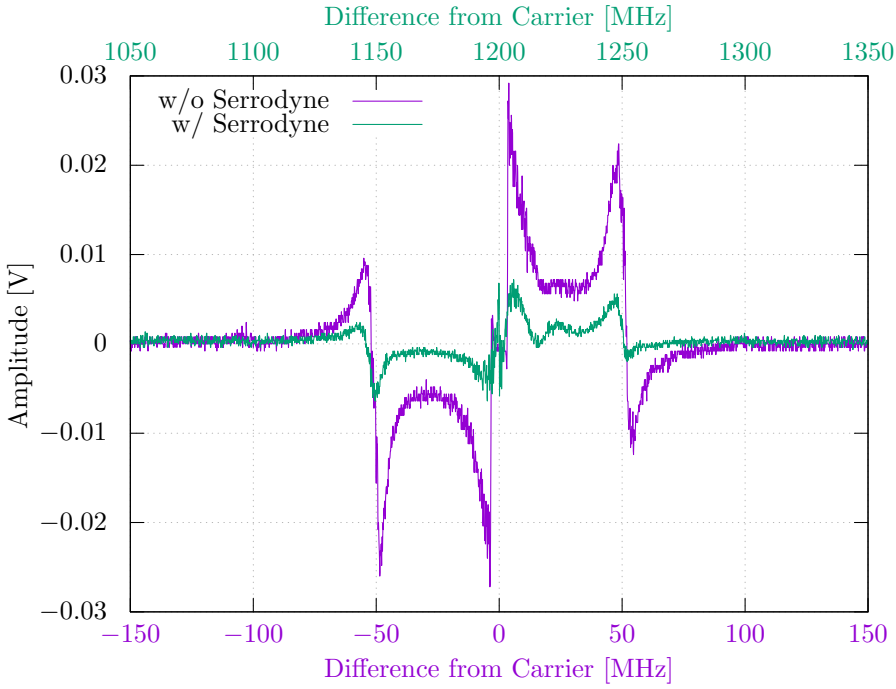

Figure 6.13: Purple: Fabry-Perot error signal for laser field electro-optically modulated at 50 MHz. Green: same signal with additional 1.2 GHz serrodyne summed at the EOM input.

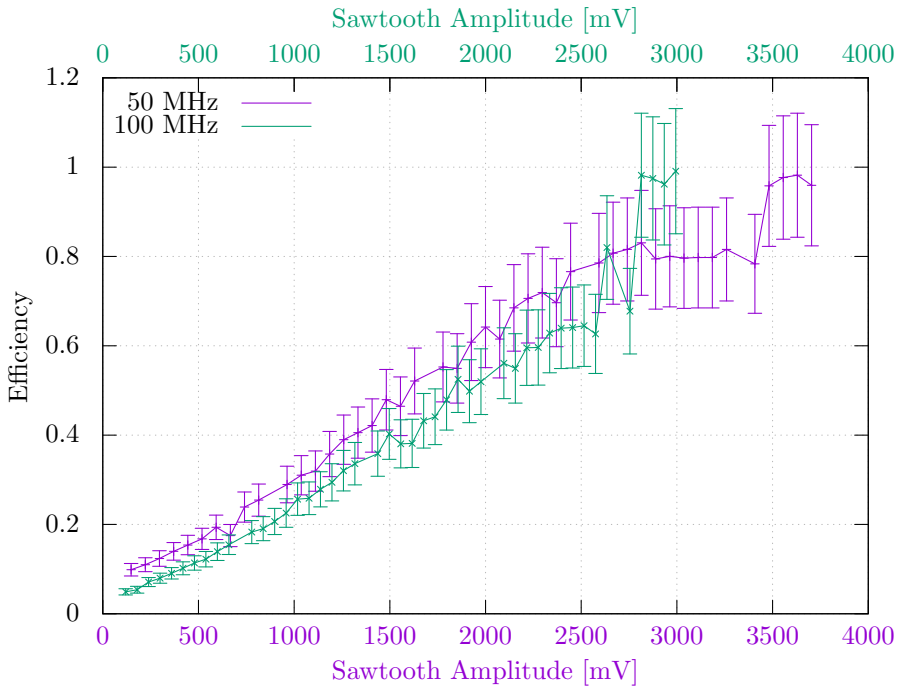

Figure 6.14: Efficiency tuning graph for serrodyne signals measured as the fraction of power transferred to the first order sideband as a function of the unmodulated carrier power. Driving amplitude was limited by the bandwidth of the function generator used.

6.3.3 Arbitrary Waveform Generation of Sawtooth

The results of the previous sections did not present serrodyne modulation with NLTLs as a promising avenue for future research despite the success achieved by other groups [92, 94]. In an effort to understand where the failing occurred, the experiment was repeated with an arbitrary waveform generator (AWG) (Tektronix AFG3252C) providing a sawtooth at lower frequencies.

Fig. 6.14 showed good efficiency could be achieved by driving the EOM with a sawtooth generated by the AWG. Efficiency here is a measure of the optical power in the first order sideband when the serrodyne signal is present divided by the unmodulated optical power of the carrier signal. The large error bars here are a reflection of the intensity noise caused by variations in transmission from an unstabilised cavity.

Efficiencies on the order of 80-90% are extremely promising. With current technology progress in the field of high speed electronics there is significant motivation to repeat this experiment with higher sampling-rate AWGs. However, as of right now these devices are prohibitively expensive for most experiments but may be common-place in years to come.

To understand why there is a stark discrepancy between the maximum serrodyne efficiencies achieved with

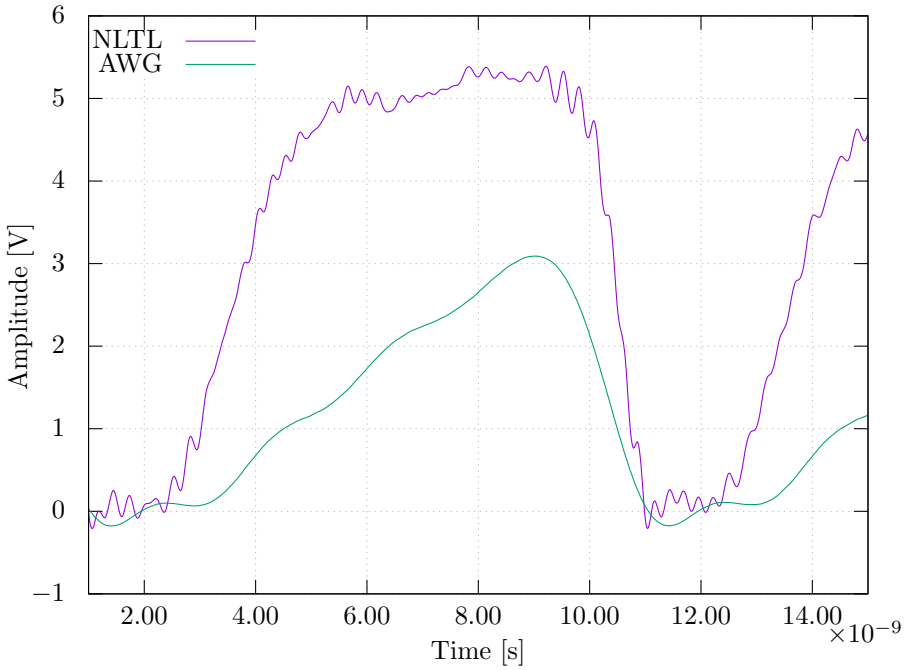

Figure 6.15: Purple: sawtooth generated by NLTL for a sinusoidal input of 100 MHz at 27 dBm. Green: sawtooth generated by an AWG overdriven to 100 MHz at 3 V_{pp}.

AWG (80-90% at 100 MHz)and NLTL (∼56% at 1.2 GHz, efficiency at 100 MHz is too poor to measure), the waveforms at 100 MHz were examined and are shown in Fig. 6.15. From the traces it is clear that the AWG waveform much better resembles the shape of a sawtooth and so it is no surprise it exhibits better efficiency.

The AWG used places a limitation on the comparisons that could be conducted. Nominally the AWG is capable of producing 2 MHz sawtooth waveforms with 5 V_{pp} amplitude but can be forced to drive higher frequencies at the expense of amplitude. Here 100 MHz was achieved with a limit on amplitude of ∼3 V_{pp} which was ample to drive the EOM shift with high efficiency. At this frequency the AWG completely outperforms the NLTL which has a negligible efficiency. However, to fully verify this test a higher bandwidth AWG would be needed to compare the signals at the maximum 1.2 GHz achievable by our NLTLs to see if the efficiency beats 56%.

CHAPTER 7

NEW GENERATION RESULTS

During the final year of the project the entire experiment was transported to a new laboratory. A combination of previous results and this relocation shifted the scientific goals of the experiment from focusing on portability and robustness to absolute precision followed by enhancing portability.

With the data presented in Chapter. 5 it was clear that certain fibre components were inhibiting the progress of the experiment for making gravity measurements. Whilst fibre-optic approaches for light delivery are employed in other groups for single beam atom traps [96], the complication of six beams decreases performance to unacceptable levels. This chapter focuses on the technology that is currently under development towards increasing portability, starting with a much more compact Raman laser. Using the compact laser and a completely redesigned light delivery system a much improved performance was shown for Ramsey interference.

7.1 Frequency Doubled Laser Source for Portable Applications

An introduction to the components used for 780 nm light generation was already shown in Fig. 3.9 and will not be repeated here. The distinction to be made here is that this laser system for 780 nm light was originally used for Raman light as it was convenient for generating high-power, dual-frequency laser pulses. Whilst the performance of this laser system was good, it was far from compact or robust for field applications which motivated research into other systems. For a compact and robust laser system it was again elected to use a fibre based approach with integrated fibre components (Fig. 6.1).

7.1.1 780nm Light Generation

A waveguide doubling crystal was used over traditional bulk crystal material for the increased efficiency at low optical powers [97, 98]. The drawback of such a system is a lower absolute power handling of $\sim$ 250 mW at the input when compared to our free-space system $\sim$ 20 W but the reduction in volume is around a factor of 5. (In reality the device we used had a specified damage threshold of 250 mW but we noticed no degradation in performance when operated at 1 W input). Performance characterisation for the new system is outlined in Figs. 7.1, 7.2 and 7.3.

It was known from theory [99] and the manufacturer that the PPLN waveguide would have an optimum operating temperature for efficient second harmonic generation of photons to ensure that the quasi-phase matching criteria is fulfilled. Experimentally this was found to be at 56.7 °C and was subsequently stabilised to within 1 mK using home-built electronics. All measurements in the remainder of this section assume temperature was optimised.

The relationship between input 1560 nm power and output 780 nm power was investigated in Figs. 7.2 and 7.3. As one would expect the output power increases as the input power increases. What is interesting is that the efficiency increases as the input power increases although this is predicted by theory. The output power of a typical waveguide doubling crystal follows the relation:

$$P_{2\omega} = \tau P_{\omega} \tanh^2\left(\sqrt{\eta L^2 \tau P_{\omega}}\right) \tag{7.1}$$

where τ is the coupling efficiency, L length of crystal and η is normalised conversion efficiency [99].

Saturation from this theoretical efficiency curve can occur due to green induced infrared absorption [97] and it appears there is some plateauing beginning after 200 mW on the trace in Fig. 7.3. A similar saturation of efficiency was reported in [100] and was suggested that this is caused by photorefractive effects in the

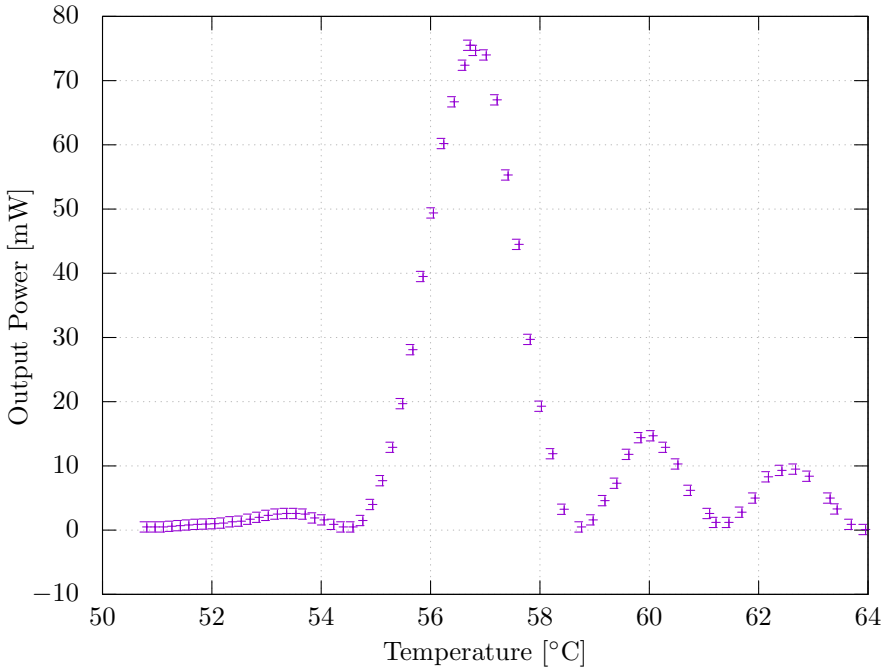

Figure 7.1: Output light power measured at 780 nm when injected with 200 mW of 1560 nm light as a function of PPLN temperature. There is a clear peak near 57°C where the quasi-phase matching criteria is fulfilled.

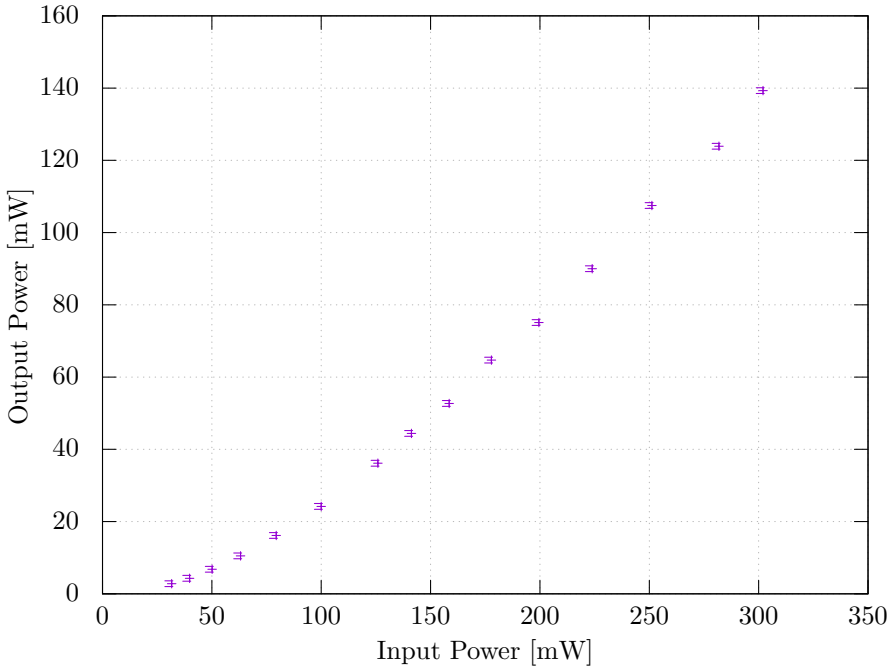

Figure 7.2: Output light power measured at 780 nm as a function of input 1560 nm light power.

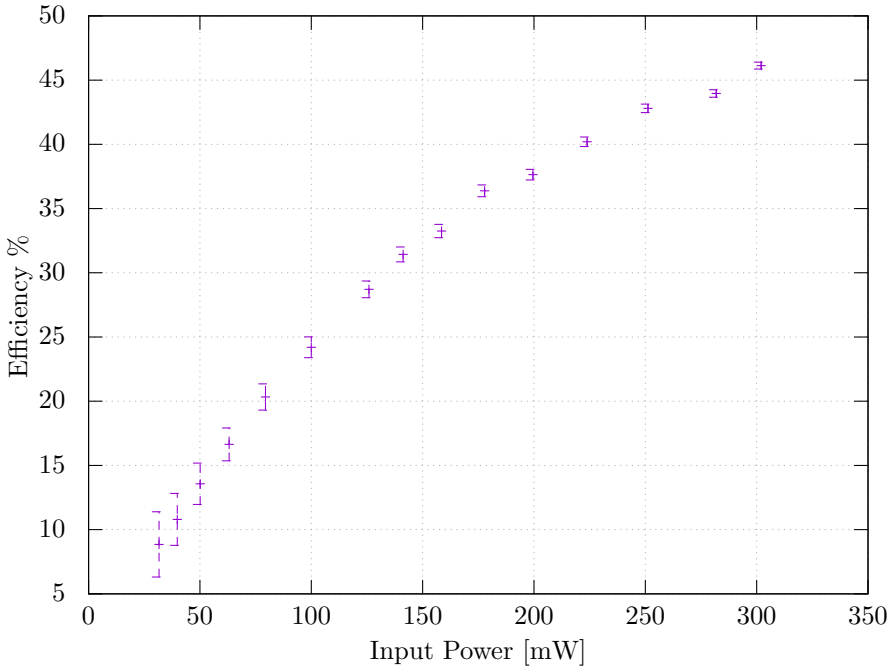

Figure 7.3: Efficiency of frequency doubling as a function of input power. An increase in efficiency for higher input powers is observed in agreement with Fig. 7.2 up to a plateau level where losses due to green induced infrared absorption dominate.

waveguide. It is expected that photorefractive effects could be lessened by heating the waveguide further but this was no verified.

The results show that our requirements on laser power for atom cooling and Raman pulses can be achieved by the new system. For trapping we could easily realise > 160 mW at the output of the doubling crystal and splitting this six ways leaves more than 25 mW per MOT beam. For Raman the situation is considerably more limited compared to using a 20 W amplifier. The maximum output at 780 nm with this new system is in the region of 500 mW which limits the extent of detuning accessible for Raman transitions. This situation can be improved with a higher power EDFA without increasing the volume of the setup substantially but the upper limit of the PPLN waveguide damage threshold is currently unknown.

7.1.2 Frequency Sidebands

When modulating the light field to generate sidebands it is necessary to understand the relationship between the driving amplitude and power transferred to the first order sidebands. Firstly it is useful when the laser is used in the cooling+repumping configuration as generally one would want most of the power in the cooling

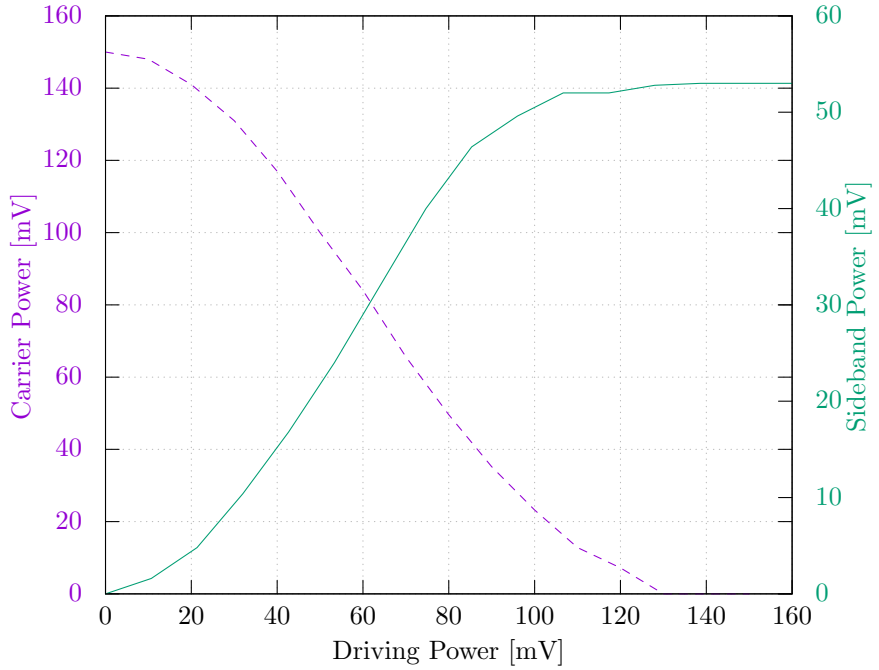

Figure 7.4: Relative intensities in the carrier and first order sidebands out of an EOM for increasing driving power.

and only a small fraction for repumping. For the Raman sideband configuration it is needed to be able to control the relative power between the two beams in order to cancel the Stark shift as outlined in Sec. 2.6.2.

Fig. 7.4 shows the measured powers in the carrier and first-order sideband as a function of the RF driving power. As expected, the maximum amount of power achievable in the first order sidebands saturates at ∼33% of the unmodulated carrier power as specified by the Bessel function of the first kind. The data shows that the ratio between carrier and sideband is widely tunable to satisfy ac Stark shift compensation.

A further useful property is that complete suppression of the carrier is possible by increasing the RF power. In the scenario where carrier and sideband are used for cooling and repumping respectively this allows one to have all possibilities of solitary cooling, cooling and repumping, and solitary repumping. This has implications for state preparation which may prove useful experimentally.

7.2 Modifications to Existing Experiment

7.2.1 Development of Free Space Light Delivery

The results of chapters 4 and 5 highlighted major systematic effects in the experiment which were caused by the fibre system. To remedy these problems and progress with the development of a gravity sensor it was

elected to build a free-space optics system for use in laboratory as shown in Fig. 7.5.

The major difference between the two approaches to light distribution is that the master laser has been excluded in the free-space approach and the cooler is directly locked to a rubidium reference via modulation transfer spectroscopy (MTS) [101] with frequency control provided by a double-passed AOM. The repumping (and eventually Raman) light was phase locked to the cooling light at a controllable frequency offset using a modified Analog Devices ADF4108. The motivation for this design choice is due to instrument performance not previously mentioned in this thesis. To summarise, the old locking scheme exhibited poor bandwidth for frequency sweeps of the cooling laser on the order of 10 ms for a 40MHz sweep. More information on this topic can be found in [102].

Use of waveplates and polarising beamsplitters allowed for good control over the intensities in every path. Frequency and amplitude control of the various trapping and detection beams was achieved with double-pass AOMs near the output fibres. These provided frequency tuning ranges of $\sim \pm 40$ MHz which were ample for molasses cooling and atomic launching as well as full intensity control for molasses and switching. Another subtle difference in this setup was that the repumping light needed for the 3D MOT was only mixed into the side trapping beams. This makes relatively little difference to the trapping but saves on additional beam splitting optics.

7.2.2 Results With Free Space System

Cold Atom Source

Using the refitted experiment, the 3D MOT was first recharacterised to test that an acceptable atom number and loading rate could be achieved from a newly-fitted dispenser. Following loading tests the temperature of the cloud after molasses cooling was reoptimised with the modified locking and computer control.

Fig. 7.6 shows the loading rates recorded by fluorescence for the 3D MOT. The optimal current for loading was found to be 4.7 A, above this value the loading rate would increase at short times but the total atom number trapped at long times would decrease due to high background pressure. For the data presented in the remainder of this work the dispenser was operated at 4 A to preserve the lifetime and because this gave a sufficient ($\sim 10^8$) atom number with a few seconds of loading. From the traces it is currently impossible to reach the 10^9 atom number specified in the design goals of Chapter. 3. The current limitation on the number of atoms we can load is background pressure from the rubidium released by the dispenser.

In the previous iteration of the experiment the frequency ramping component of molasses cooling was achieved by sweeping a mix frequency provided to the cooling offset lock. This had the effect of sweeping the

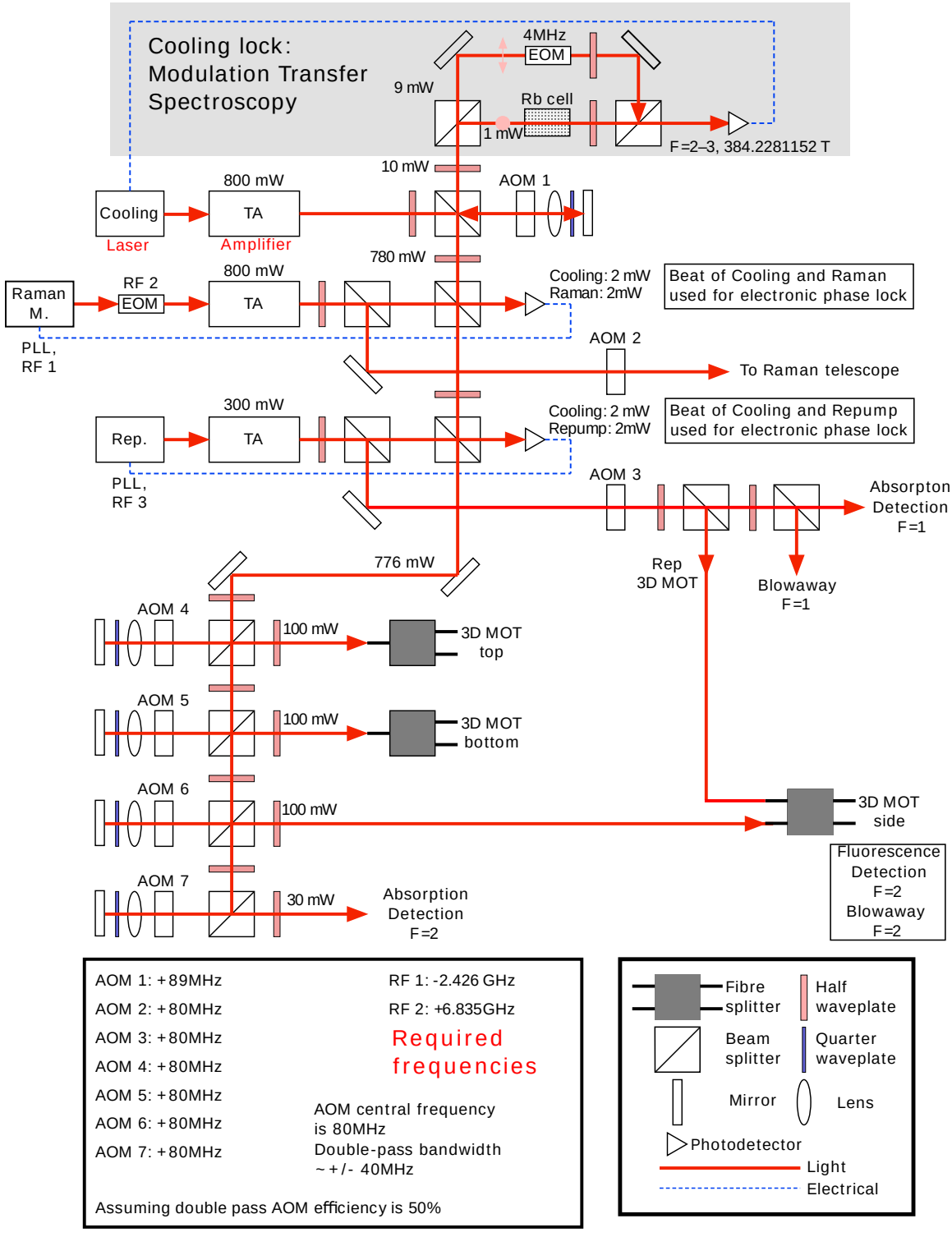

Figure 7.5: Proposed free space optics to replace fibre distribution system. In this design the master and offset lock scheme has been replaced with the cooling light directly locked to the rubidium reference and a phase locked loop (PLL) employed to lock the repumper and Raman lasers. Double pass AOMs are used for frequency control of light. All AOMs at outputs are used as optical switches.

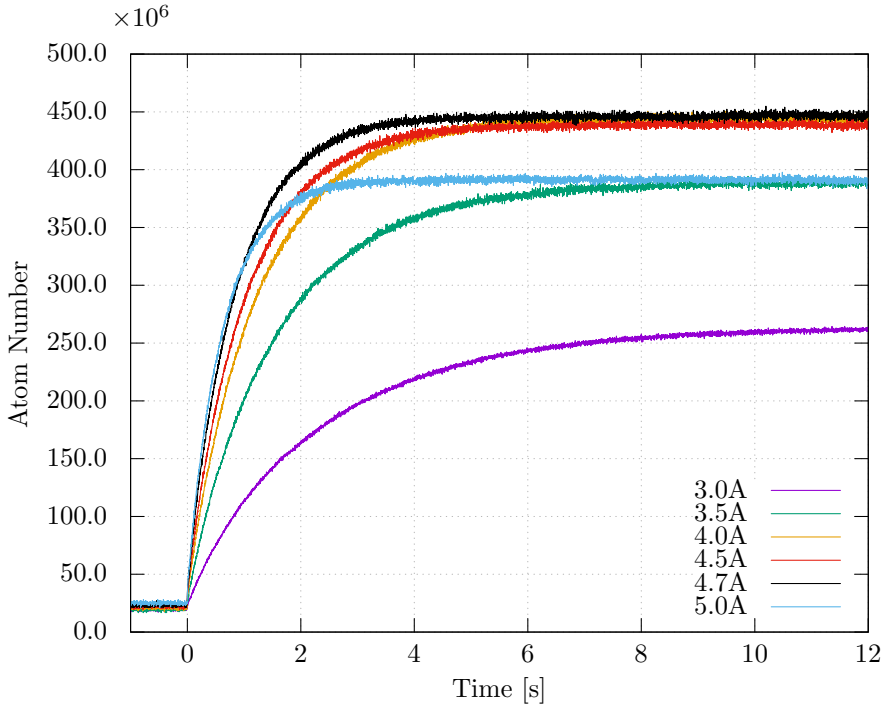

Figure 7.6: Number of atoms loaded into 3D MOT as a function of time for varying dispenser currents.

frequency of all 6 beams in an identical manner without affecting the intensity and was necessary because the tuning range of a typical single-pass fibre-AOM is on the order of a few MHz. In the new configuration the frequency of any set of beams can be swept independently with a double-passed AOM affording a tuning range of $\sim \pm 40$ MHz but the intensity of the light in this case is also affected by the changing AOM efficiency. The molasses sequence previously used was therefore no longer relevant and had to be recharacterised.

With very little effort a post-molasses temperature comparable to that shown in Fig. 4.3 was achieved using the new setup. At the time of writing this work it was unnecessary to cool further as this temperature provides a sufficient starting point to study interference fringes. The major improvement over the old results was stability in both the achievable temperature and the central position of the cloud. Both of these are attributed to the beam balance during the molasses phase which was poor in the previous design but stable to less than 2% using free-space optics.

Rabi

Using the compact Raman laser system described in Sec. 7.1 and a cold cloud of $\sim 10^7$ atoms a test of Rabi oscillation was performed for comparison against Fig. 4.15 with a similar experimental sequence. The new results showed a factor of 2 lower in contrast suggesting a loss of atoms as the transferred atoms in

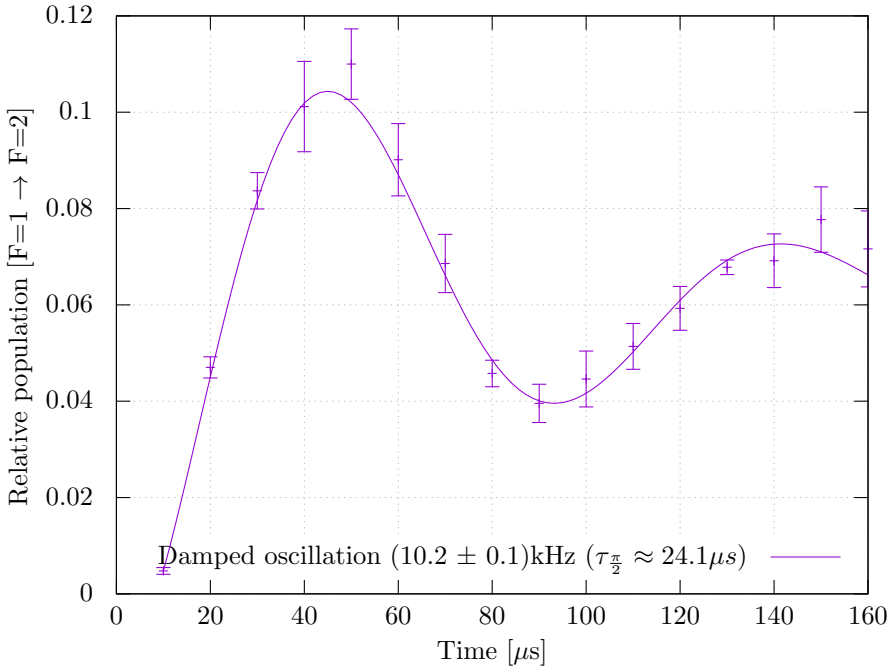

Figure 7.7: Rabi oscillation for intensity 98 mW/cm^2 and detuning 1.3 GHz. The data shows the number of atoms transferred to the $|F = 2\rangle$ state as a function of the duration of the Raman pulse.

both data sets were normalised to MOT fluorescence. However, the new data showed an increased coherence illustrated by considerably smaller error bounds at longer times. This increase in coherence is explained by the enhanced stability of the optics which afford lower intensity drifts and preservation of beam balance.

A comment on the different timescales between the two figures. In Fig. 4.15 there was a considerable amount of Raman power available allowing for high intensity and short pulse durations. With the new, compact Raman laser system there is a limit on total optical power of $\sim$ 400 mW meaning the pulses and hence Rabi oscillation is proportionally longer.

Ramsey

With the promising results of state transfer in the previous section it was decided to retest Ramsey interference to assess the viability of the instrument for making interference measurements - ultimately for gravity.

Fig. 7.8 shows the most recent data-set recorded for interference fringes using similar parameters to those presented in Fig. 4.11 but with much less intensity as mentioned in the previous section. A key difference for this measurement was the inclusion of a bias field in the vertical direction around the 3D MOT chamber. Providing a quantisation axis for the circularly polarised Raman light showed a significant improvement in the quality of the interference fringes. One can see a much greater contrast in the new data with resolvable

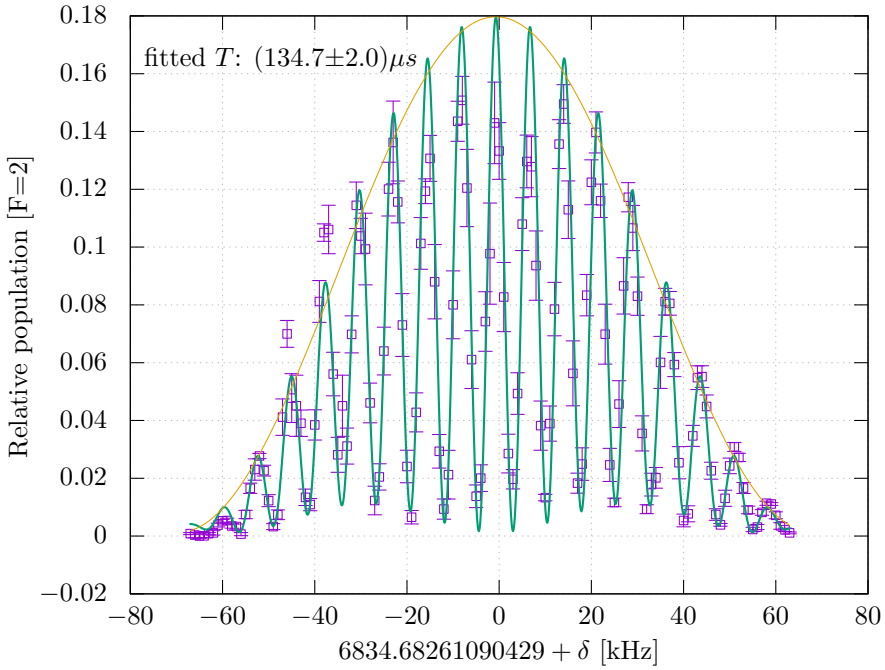

Figure 7.8: Population of $|F = 2\rangle$ state measured for 1 kHz detuning steps with $\tau_{\frac{\pi}{2}} = 13.9$ μs. Time (T) between the rising edge of the Raman pulses was measured to be 133.9 μs.

oscillations that better fit the theoretical model.

The data in Fig. 7.8 shows good agreement between theory and experiment for a pulse separation of 133.9 μs with fitted separation of 134.7±2 μs respectively. The population of atoms recorded is normalised to the MOT fluorescence before molasses cooling. In this instance the atoms are prepared in the $|F = 1\rangle$ state following molasses cooling and one may assume that these atoms are equally spread among the three m_F states. If this is the case then there are only 33% of the atoms satisfying the resonance criteria of the Raman pulses due to Zeeman splitting and a peak population measurement of $\sim$ 16% implies that this interference contrast would be around 50% after state selection. This is promising for future gravity measurements after further optimisation of the trapping and cooling has been realised.

Referring back to Sec. 3.1, the current atom number of $\sim 4.5 \times 10^8$ would limit the sensitivity to changes in g at the $6.13 \times 10^{-10}\text{ms}^{-2}/\sqrt{\text{Hz}}$. Whilst this may appear to be a good sensitivity when compared to similar portable systems like those reported in [9] which achieve $\sim 1 \times 10^{-8}\text{ms}^{-2}/\sqrt{\text{Hz}}$ for 4×10^8 atoms and $2T = 120$ ms, it must be stated that our estimation is noise floor and real experimental performance will be hindered by additional effects.

As an illustration of systematic effects, [62] achieves a similar short term sensitivity to the above at

$9.6 \times 10^{-8}\mathrm{ms}^{-2}/\sqrt{\mathrm{Hz}}$ but with an enhanced atom number of 10^9 and free-evolution time of 260 ms. The dominant noise source in their experiment is that from the curvature of the Raman wavefront at the $\sim 2 \times 10^{-8}\mathrm{ms}^{-2}$ level. Whilst atom number will ultimately limit the sensitivity of this apparatus with the current low number of atoms, it will likely not be the dominant noise source for a long time. For that reason it is expected that the experiment will soon progress to recording gravity.

CHAPTER 8

OUTLOOK AND CONCLUSIONS

This final chapter will present a summary of the project as a whole. The author's thoughts on the progress made to the project will be outlined which will motivate a discussion on future goals. The report will end with a few closing remarks from the author.

8.1 Progress and Measurements

8.1.1 Summary

The project started as an investigation into building a robust and portable gravity gradiometer based on ultracold rubidium atoms. As part of this work risks were taken to try novel techniques for enhancing portability. It was ultimately found that these risks were a liability and limited the achievable performance of the device. In particular, the fully-integrated fibre system designed to deliver light to the experiment was found to underperform substantially. Modifications to the light delivery through use of less compact free-space optics showed considerable improvement in the performance of the device to the point where it is almost ready to perform as a gravity sensor as demonstrated by the ability to observe clear Ramsey interference fringes. The work of this PhD can be summarised as the initial design and construction of an atom interferometer with some preliminary characterisation. It is now the responsibility of new students to optimise the experiment and achieve gravity measurements.

8.1.2 Key Results

It has been found that individually most fibre-optic components are sufficient in their ability to maintain polarisation for a transportable gradiometer, at the 20 dB level for polarisation extinction ratio. In connecting many of these components in series it was shown that fibre-splicing is a reliable method for maintaining polarisation and intensity between components. However, the worst component in the system would limit the polarisation stability of the whole system and in this experiment the fibre-AOMs were the limiting factor. It is expected that with more effort and higher quality manufactured components such a system could be recreated with much greater performance.

Replacing the fibre components with a free-space alternative showed much greater experimental stability at the cost of compactness, reducing intensity fluctuations from $\sim 10\%$ to $\sim 1\%$. With the enhanced stability high contrast interference fringes were achieved which suggest a 50% fringe contrast following state selection and are a promising motivator for future gravity measurements.

The interference fringes mentioned above were recorded with a compacted Raman laser which fits comfortably in a 1U 19" rack box, fulfilling part of the criteria towards a compact and portable system. Research has been commenced on the technique of serrodyne modulation of such a telecom laser system with the intention of replacing the current system of cooling, repumping and Raman lasers with a single, agile laser. So far frequency shifts using this method have shown lower efficiency than those recorded by other groups

and this must be rectified before it becomes useful. The potential application of such a laser would benefit more a single-beam pyramidal atom trap where absolute portability is the main concern.

8.2 Long Term Goals

8.2.1 Measurement of Gravity Gradients in the Lab

As the experiment currently stands there is everything necessary to perform gravity measurements. Some modifications will need to be performed in the form of a retroreflection mirror mounted in the Raman beam path and inclusion of a microwave source for state selection but this presents only a small technical challenge.

The most obvious limitation for gravity sensitivity is currently the cloud temperature. Without fully optimising the molasses cooling stage the cloud is currently at a few tens of μK. Assuming an arbitrarily large detection setup such that all atoms can be recorded, at such temperatures the cloud would expand outside the 20 mm spatial extent of the Raman beam in around 300 ms, limiting the available flight time of the atomic launch.

For gravity gradients, the limitation imposed on the flight time has two consequences for the instrument sensitivity. Firstly to get two clouds into free-flight with a limited time requires that the atom cloud is loaded for less time or a complicated juggling scheme is used to get two clouds with decent atom number. In addition to this, the maximum achievable separation between the clouds will be limited by the flight time providing a weaker probe of the gravity gradient. Secondly, the sensitivity to gravitational phase shift scales quadratically with the time between interferometer pulses. Having a shorter flight time necessarily means a shorter time between pulses and lower sensitivity.

8.2.2 Measurement of Gravity Gradients in Known Locations

Once precision measurements of gravity gradients are established, the ultimate goal of the experiment is to make field measurements. For this there will be some effort in robustifying the light delivery system to minimise misalignment during transport. Currently all optics fit on a single transportable breadboard and all electronics fit in a 19" rack making transportation of the system relatively simple.

For field tests there are currently several candidates which have been mapped using a classical gravimeter by colleagues in the Civil Engineering department. These would allow for direct comparison between a commercial gravity surveying device and a cold atom system that will hopefully be commercial in the future. One such example is illustrated in Fig. 8.1.

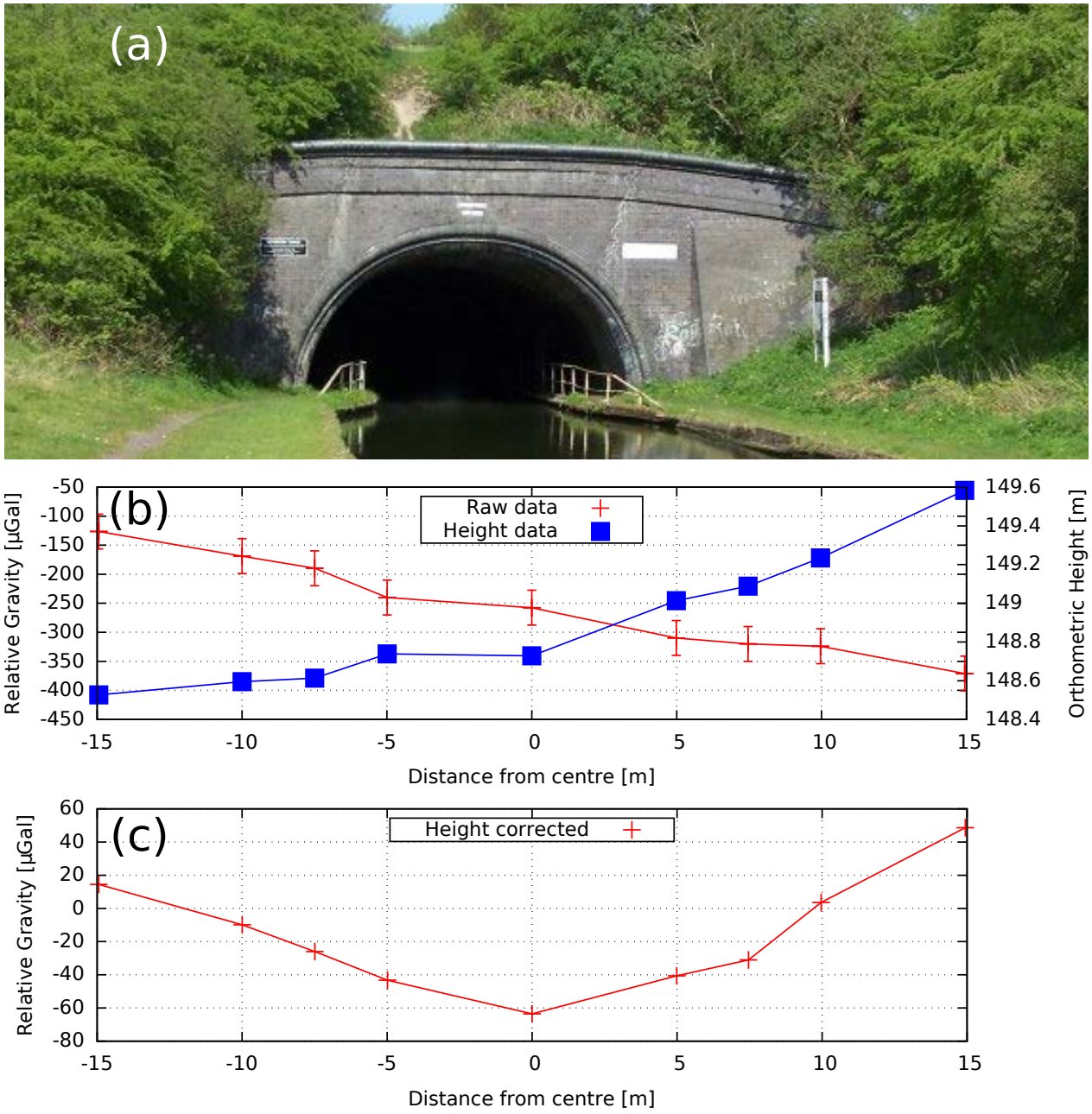

Figure 8.1: **(a)** Photograph of entrance to tunnel where gravity survey was conducted. Measurements were taken across the top of the tunnel spanning several metres either side of the width. **(b)** raw gravity signal (red, no squares) and height data measured by GPS (blue, squares). **(c)** height corrected gravity signal showing a clear dip in gravity strength over the void of the tunnel. *(Kindly provided by Dr. D. Boddice, University of Birmingham)*

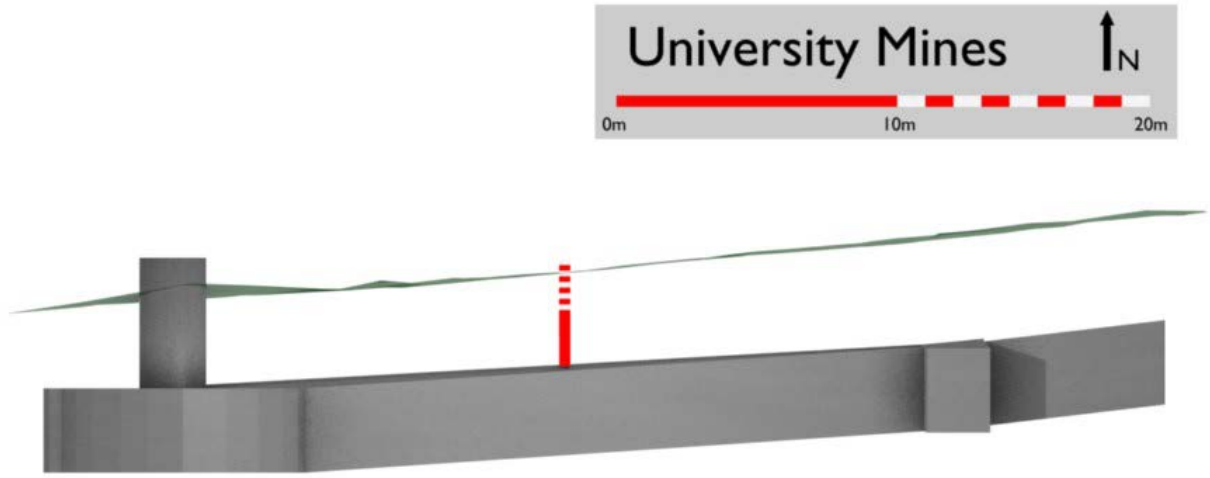

Figure 8.2: 2D render of mine shaft located on university campus. The tunnels are approximately 1.5 m in diameter and at a similar depth. *(Kindly provided by Dr. P. Murgatroyd, University of Birmingham)*

More locally there are a set of mines on University Campus (Fig. 8.2) that are buried approximately 1.5 m deep and have a similar diameter. If a 1 Eötvös gradiometer is capable of resolving a 10 cm void at a depth of 1 m then this experiment should be able to map such a tunnel after characterisation of noise sources.

Finally on the southern coast of England at Herstmonceux exists an observatory operating a falling corner-cube interferometer. It is planned to transport this experiment there to calibrate the absolute sensitivity against a ready calibrated device.

APPENDIX A

RUBIDIUM INFORMATION

Presented here are the most relevant properties of ^{87}Rb from [75]. The interested will find much more detail in the aforementioned source.

A.1 Energy Levels

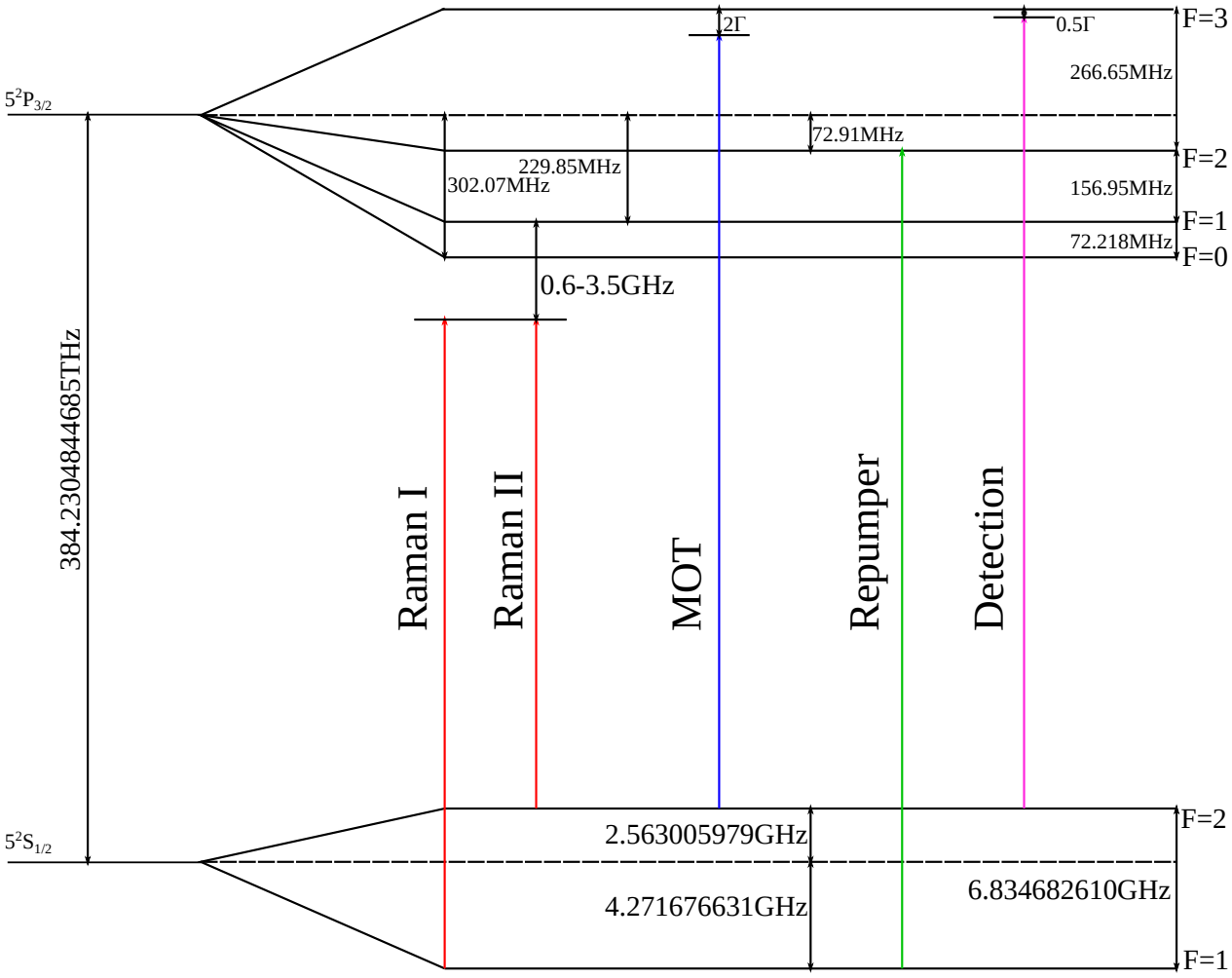

Figure A.1: Hyperfine splitting of ^{87}Rb ground state and first excited state.

Light Beam	**Frequency/THz**
Raman I	384.2315263
Raman II	384.2246916
MOT	384.2280390
Repumper	384.2304845
Detection	384.2090550

Table A.1: Frequencies required for the various laser beams in our experiment.

A.2 Transition Probablities

	$m_F = -2$	$m_F = -1$	$m_F = 0$	$m_F = 1$	$m_F = 2$
$F' = 3$	$\sqrt{1/30}$	$\sqrt{1/10}$	$\sqrt{1/5}$	$\sqrt{1/3}$	$\sqrt{1/2}$
$F' = 2$	$\sqrt{1/12}$	$\sqrt{1/8}$	$\sqrt{1/8}$	$\sqrt{1/12}$	
$F' = 1$	$\sqrt{1/20}$	$\sqrt{1/40}$	$\sqrt{1/120}$		

Table A.2: ^{87}Rb D_2 ($5^2S_{1/2} \rightarrow 5^2P_{3/2}$) Hyperfine Dipole Matrix Elements for σ^+ transitions ($F = 2, m_F \rightarrow F', m'_F = m_F + 1$), expressed as multiples of $\langle J = 1/2| \, er \, |J' = 3/2\rangle$.

	$m_F = -2$	$m_F = -1$	$m_F = 0$	$m_F = 1$	$m_F = 2$
$F' = 3$	$-\sqrt{1/6}$	$-\sqrt{4/15}$	$-\sqrt{3/10}$	$-\sqrt{4/15}$	$-\sqrt{1/6}$
$F' = 2$	$-\sqrt{1/6}$	$-\sqrt{1/24}$	0	$\sqrt{1/24}$	$\sqrt{1/6}$
$F' = 1$		$\sqrt{1/40}$	$\sqrt{1/30}$	$\sqrt{1/40}$	

Table A.3: ^{87}Rb D_2 ($5^2S_{1/2} \rightarrow 5^2P_{3/2}$) Hyperfine Dipole Matrix Elements for π transitions ($F = 2, m_F \rightarrow F', m'_F = m_F$), expressed as multiples of $\langle J = 1/2| \, er \, |J' = 3/2\rangle$.

	$m_F = -2$	$m_F = -1$	$m_F = 0$	$m_F = 1$	$m_F = 2$
$F' = 3$	$\sqrt{1/2}$	$\sqrt{1/3}$	$\sqrt{1/5}$	$\sqrt{1/10}$	$\sqrt{1/30}$
$F' = 2$		$-\sqrt{1/12}$	$-\sqrt{1/8}$	$-\sqrt{1/8}$	$-\sqrt{1/12}$
$F' = 1$			$\sqrt{1/120}$	$\sqrt{1/40}$	$\sqrt{1/20}$

Table A.4: ^{87}Rb D_2 ($5^2S_{1/2} \rightarrow 5^2P_{3/2}$) Hyperfine Dipole Matrix Elements for σ^- transitions ($F = 2, m_F \rightarrow F', m'_F = m_F - 1$), expressed as multiples of $\langle J = 1/2| \, er \, |J' = 3/2\rangle$.

	$m_F = -1$	$m_F = 0$	$m_F = 1$
$F' = 2$	$\sqrt{1/24}$	$\sqrt{1/8}$	$\sqrt{1/4}$
$F' = 1$	$\sqrt{5/24}$	$\sqrt{5/24}$	
$F' = 0$	$\sqrt{1/6}$		

Table A.5: ^{87}Rb D_2 ($5^2S_{1/2} \rightarrow 5^2P_{3/2}$) Hyperfine Dipole Matrix Elements for σ^+ transitions ($F = 1, m_F \rightarrow F', m'_F = m_F + 1$), expressed as multiples of $\langle J = 1/2| \, er \, |J' = 3/2\rangle$.

	$m_F = -1$	$m_F = 0$	$m_F = 1$
$F' = 2$	$-\sqrt{1/8}$	$-\sqrt{1/6}$	$-\sqrt{1/8}$
$F' = 1$	$-\sqrt{5/24}$	0	$\sqrt{5/24}$
$F' = 0$		$\sqrt{1/6}$	

Table A.6: ^{87}Rb D_2 ($5^2S_{1/2} \rightarrow 5^2P_{3/2}$) Hyperfine Dipole Matrix Elements for π transitions ($F = 1, m_F \rightarrow F', m'_F = m_F$), expressed as multiples of $\langle J = 1/2 | \, er \, | J' = 3/2 \rangle$.

	$m_F = -1$	$m_F = 0$	$m_F = 1$
$F' = 2$	$\sqrt{1/4}$	$\sqrt{1/8}$	$\sqrt{1/24}$
$F' = 1$		$-\sqrt{5/24}$	$-\sqrt{5/24}$
$F' = 0$			$\sqrt{1/6}$

Table A.7: ^{87}Rb D_2 ($5^2S_{1/2} \rightarrow 5^2P_{3/2}$) Hyperfine Dipole Matrix Elements for σ^- transitions ($F = 1, m_F \rightarrow F', m'_F = m_F - 1$), expressed as multiples of $\langle J = 1/2 | \, er \, | J' = 3/2 \rangle$.

A.3 Rabi Frequency

For a two level system in an electromagnetic field, the coupling between the two atomic states can be measured by the Rabi frequency:

$$\Omega = -\frac{\langle e | \, \hat{\mu} \cdot \epsilon E_0 \, | g \rangle}{\hbar} \tag{A.1}$$

where $\hat{\mu} = e\hat{\mathbf{r}}$ is the dipole operator for the atom. Experimentally one measures the intensity of a light field, not the electric field amplitude, so it is practical to make the substitution $I = \frac{1}{2}\epsilon_0 c E_0^2$:

$$\Omega = \frac{eE_0}{\hbar} \langle e | \, \hat{\mathbf{r}} \cdot \epsilon \, | g \rangle \tag{A.2a}$$

$$= \sqrt{\frac{e^2 2I}{\epsilon_0 \hbar^2 c}} \langle e | \, \hat{\mathbf{r}} \cdot \epsilon \, | g \rangle \tag{A.2b}$$

The BraKet term contains the matrix elements for the transitions allowed by selection rules between a ground and excited state. The exact solution is found from the Wigner-Eckart theorem ([103] gives a good explanation) but it is sufficient here to state that it results in a constant multiplied by the transition

probability given by Clebsch-Gordan coefficients [75]:

$$\Omega_n = \sqrt{\frac{e^2 2I}{\epsilon_0 \hbar^2 c}} D\rho_n \tag{A.3}$$

where D = reduced dipole element = 3.58424×10^{-29} C· m and ρ_n are the transition probability matrix elements. We're interested in a pseudo two level system being driven by a two photon transition so there are two separate Rabi frequencies between hyperfine ground states and intermediate state:

$$\Omega_1 = \sqrt{\frac{e^2 2I_1}{\epsilon_0 \hbar^2 c}} D\rho_1 \quad \& \quad \Omega_2 = \sqrt{\frac{e^2 2I_2}{\epsilon_0 \hbar^2 c}} D\rho_2 \tag{A.4}$$

Under the assumption that the detuning from resonance, Δ_R, is much larger than the hyperfine splitting of the excited state, the selection rules enforce that laser 1 couples the ground state hyperfine level $|F = 1\rangle$ to intermediate states $|F' = 0, 1, 2\rangle$ whilst laser 2 couples state $|F = 2\rangle$ to intermediate states $|F' = 1, 2, 3\rangle$. Of these intermediate states only $|F' = 1, 2\rangle$ are common to both lasers and valid for a Raman transition. The effective Rabi frequency is then goverened by the relative transition probability which is the sum over all possible transitions.

$$\Omega_{\text{eff}} = \sum_{\rho} \frac{\Omega^*_{1;|F=1,m_F \to F',m_{F'}\rangle} \Omega_{2;|F=2,m_F \to F',m_{F'}\rangle}}{2\Delta_R} \tag{A.5}$$

Used in this experiment for Secs. 4.3 and 4.5 are two photon transitions with co-propagating $\sigma^+\sigma^+$ polarised light and $\Delta m_F = 0$. The transition probabilities were previously presented in Sec. A.2 from which one can calculate the effective Rabi frequency in combination with known laser parameters.

The presence of a small detuning from the two-photon resonance, δ_R, and AC Stark shift, δ^{AC}, can be included as a quadratic sum. The off-resonance Rabi frequency is then:

$$\Omega'_{\text{eff}} = \sqrt{(\delta^{\text{AC}} - \delta_R)^2 + \Omega^2_{\text{eff}}} \tag{A.6}$$

where the AC Stark term can be calculated from [1]:

$$\delta^{\text{AC}} = \sum_{\rho} \frac{\Omega^*_1 \Omega_1}{2\Delta_R} - \sum_{\rho} \frac{\Omega^*_2 \Omega_2}{2\Delta_R} \tag{A.7}$$

A.4 Useful Numbers

Frequency	ω_0	2π·384.2304844685(62) THz
Transition Energy	$\hbar\omega_0$	1.589049439(58) eV
Wavelength (Vacuum)	λ	780.241209686(13) nm
Lifetime	τ	26.24(4) ns
Natural linewidth	Γ	2π·6.065(9) MHz
Recoil temperature	T_r	361.96 nK
Doppler temperature	T_D	146 μK
Saturation intensity	$I_{sat(F=2,m_F=\pm2\rightarrow F'=3,m_F=\pm3)}$	1.669(2) mW/cm^2
Scattering cross section	$\sigma_{0(F=2,m_F=\pm2\rightarrow F'=3,m_F=\pm3)}$	2.907×10^{-9} cm^2
D_2 transition dipole matrix element	$\langle J=1/2\vert\vert er\vert\vert J'=3/2\rangle$	3.584(4)×10^{-29} C·m
Dipole moment (π polarisation)	d_{det,D_2}	2.069(2)×10^{-29} C·m

Table A.8: Useful rubidium numbers.

APPENDIX B

TOOLS FOR MOTS AND ATOM CLOUDS

This section contains a collection of theory that was used in part for the analysis of MOT parameters in chapters 3 & 4. It is by no means exhaustive but provides a suitable picture of how the experiment should work and how one can measure the cloud.

B.1 Capture Velocity

To calculate the critical velocity of atoms that can be captured from the 2D MOT one must consider the Zeeman splitting of the energy levels involved and the detuning of the trapping beams. The capture radius is the point at which the detuning and Zeeman shift have a similar effect on the transition frequency such that:

$$r_c = \frac{\hbar\delta}{\mu_B g \nabla B} \tag{B.1}$$

where δ is the detuning, $g = 2.002$ is the Landé g-factor [75] and ∇B is the magnetic field gradient.
The time taken to cool an atom to zero velocity scales as

$$\tau = \frac{2mv}{\hbar k \Gamma} \tag{B.2}$$

and the fastest atoms will need to traverse the entire trapping region to slow down i.e. the distance they travel is $2r_c$. The transit time for these atoms will be $\tau = 2r_c/v_c$. Equating the previous relations for $v = v_c$ gives:

$$v_c = \sqrt{\frac{\hbar\delta}{\mu_B g \nabla B}\frac{\hbar k\Gamma}{m}} \tag{B.3}$$

B.2 Atomic Flux

To calculate the expected atomic flux from the 2D MOT to the 3D MOT one must first understand the loading rate of the 2D MOT then translate this to a flux. The 2D MOT can be thought of as a cylinder of atoms that are trapped radially but not axially. Atoms captured in a capture volume defined by a cylinder of radius r_c have a radial velocity below the critical capture velocity $v_r < v_c$. The loading rate of such a system is defined by the number of atoms passing through the surface of the capture volume such that:

$$R(n, v_z) = 2\pi r_c n \int_0^{v_c(v_z)} 2\pi v_r^2 (\pi v_{max}^2)^{-3/2} e^{-(v_r^2+v_z^2)/v_{max}^2} \mathrm{d}v_r \tag{B.4}$$

$$= \frac{4\sqrt{\pi} r_c n}{v_{max}^3} e^{-v_z^2/v_{max}^2} \int_0^{v_c(v_z)} \mathrm{d}v_r v_r^2 e^{-v_r^2/v_{max}^2} \tag{B.5}$$

For a particular velocity, the total flux of atoms is related to the loading rate by [67]

$$\Phi(n, v_z) = \frac{\int_0^L R(n, v_z) e^{-\Gamma_{\text{collision}} z/v_z} \mathrm{d}z}{1 + \Gamma_{\text{trap}}(n_{\text{total}})/\Gamma_{\text{out}}} \tag{B.6}$$

The terms of interest here are as follows: Γ_{trap} refers to the loss rate of atoms from the trap due to collisions with background atoms, Γ_{out} is the rate of atoms flowing out of the trap in the desired direction and $\Gamma_{\text{collision}} = n_{\text{total}} \bar{v} \sigma_{\text{eff}}$ is the loss of atoms from Γ_{out} due to light assisted collisions. n is the density of ^{87}Rb and n_{total} is the total density of Rb (i.e. $n = 0.28 n_{\text{total}}$).

For a mean $z = L/2$ where L is the length of the trap, combining the previous two equations yields:

$$\Phi(n, v_z) = \frac{4\sqrt{2\pi} r_c n}{v_{max}^3} \frac{v_z}{\Gamma_{\text{collision}}(1 + \Gamma_{\text{trap}}/\Gamma_{\text{out}})} e^{v_z^2/v_{max}^2} \left(1 - e^{-\Gamma_{\text{collision}} L/v_z}\right) \int_0^{v_c} \mathrm{d}v_r v_r^2 e^{-v_r^2/v_{max}^2} \tag{B.7}$$

Finally, for the total flux one integrates over all velocities:

$$\Phi_{\text{total}} = \int_0^\infty \Phi(n, v_z) \mathrm{d}v_z \tag{B.8}$$

Based on [67], $\sigma_{\text{eff}} \approx 3 \times 10^{-12}$ cm^2 and $\bar{v} \approx 270$ ms^{-1} which leads to $\Gamma_{\text{collision}} \approx 10^2$ s^{-1}. $\Gamma_{\text{out}} \approx 10^3$ s^{-1} and $\Gamma_{\text{trap}} \approx 10$ s^{-1} at pressures of 10^{-7} mbar.

For our 2D MOT, the capture velocity from $v_c \approx \sqrt{r_c \hbar k \Gamma / m} = 52.8$ ms^{-1}. However, above a critical longitudinal velocity, $v_{z,crit}$, the longitudinal transit time for the atoms becomes less than the radial transit time needed to confine the atoms. This places a limit on the capture velocity.

For atoms with $v_z > v_{z,crit}$, v_c depends on v_z and so there is a longitudinal position dependence of the capture velocity.

$$v_c(z) = \begin{cases} \sqrt{r_c \frac{\hbar k \Gamma}{2m}} = v_{c0} & \text{for } v_z < v_{z,crit} \\ \frac{\hbar k \Gamma}{2m} \frac{z}{v_z} = \frac{v_{z,crit} v_{c0}}{v_z} & \text{for } v_z > v_{z,crit} \end{cases}$$

As a function of v_z:

$$v_c(v_z) = \frac{v_{c0}}{1 + v_z/v_{z,crit}} \tag{B.9}$$

Eq. B.7 is an integral over this changeable capture velocity which leads to a mathematically challenging integral in Eq. B.8.

B.3 Loading Rates and Atom Number

The total number of atoms loaded into a trap as a function of time follows the relation [67]:

$$N(t) = \frac{R}{\Gamma_{\text{collision}}} \left(1 - e^{-\Gamma_{\text{collision}} t}\right) \tag{B.10}$$

where the loading rate, R, is:

$$R = \frac{1}{2} n V^{2/3} \frac{v_c^4}{v_{max}^3} \tag{B.11}$$

and the collision rate, $\Gamma_{\text{collision}} = n_{\text{total}} \bar{v} \sigma$ where $\bar{v}$ is the mean velocity from the Maxwell-Boltzmann distribution ($\bar{v} = \sqrt{8 k_B T / \pi m}$).

v_c can be estimated from the number of photon absorptions it takes to slow an atom to zero within a capture radius r_c.

$$v_c = \sqrt{r_c \frac{\hbar k \Gamma}{m}} \tag{B.12}$$

Finally, $v_{max} = \sqrt{2 k_B T / m}$ is the most probable velocity. At low times the number of atoms trapped scales roughly linearly with the loading rate. At longer times there is an exponential fall-off due to collision related losses. The number of atoms trapped reaches a steady state at long times where the loading rate balances the collisional losses.

B.4 Fluorescence Imaging

Fluorescence emitted from an illuminated atomic cloud can be used to estimate the number of atoms. The power radiated by a MOT of atoms is:

$$P_{MOT} = \Gamma_{SC} N E \tag{B.13}$$

where $E = hc/\lambda$ is the energy per photon, N is the number of atoms and

$$\Gamma_{SC} = \frac{\Gamma}{2} \frac{I/I_s}{1 + I/I_s + 4\Delta^2/\Gamma^2} \tag{B.14}$$

The power measured by the photodiode depends on the solid angle and any gain electronics

$$P_{PD} = \frac{V}{\kappa g_n G S T_r} \tag{B.15}$$

where V is voltage, κ is the fractional solid angle, g_n is the photodiode gain, G is the photodiode impedance, S is the spectral response of the photodiode material and T_r is the transmission (attenuation).

Solving Eqs. B.13 and B.15 for N yields [104]:

$$N = \frac{V}{\kappa g_n G S T_r \Gamma_{SC} E} \tag{B.16}$$

B.5 Absorption Imaging

The number of atoms in an atomic cloud can be calculated from the shadow cast by the cloud when illuminating a camera with a resonant probe beam. Using a 2D atomic density:

$$n_{2D} = \int n(u,x,y)du = \ln\left(\frac{I_{in}(x,y)}{I_{out}(x,y)}\right)\frac{1}{\sigma_L} \tag{B.17}$$

where x and y are the horizontal and vertical axis of the 2D-projection. I_{in} and I_{out} refer to light field cross-sections with and without the cloud. σ_L is the cross-section for light absorption:

$$\sigma_L = h\nu\frac{\Gamma}{2}\frac{I/I_s}{1+I/I_s+4\Delta^2/\Gamma^2} = \frac{A}{1+I/I_s+4\Delta^2/\Gamma^2} \tag{B.18}$$

The total number of atoms is then found by integrating the 2D atomic density over the horizontal and vertical space:

$$N = \int_{x,y} n_{2D}\mathrm{d}x\mathrm{d}y = \int_{x,y} \ln\left(\frac{I_{in}(x,y)}{I_{out}(x,y)}\right)\frac{1}{\sigma_L}\mathrm{d}x\mathrm{d}y \tag{B.19}$$

Here the log term represents the optical density of the cloud at each point. When one considers the imaging device is a camera with discrete pixels, the integration can be replaced by a sum of optical densities over all pixels of the camera which leads to:

$$N = \frac{OD_{sum}}{\sigma_L} \tag{B.20}$$

LIST OF REFERENCES

[1] M. A. Kasevich and S. Chu. Measurement of the gravitational acceleration of an atom with a light-pulse atom interferometer. *Applied Physics B Photophysics and Laser Chemistry*, 54(5):321–332, may 1992.

[2] A. Peters, et al. High-precision gravity measurements using atom interferometry. *Metrologia*, 38(1):25–61, feb 2001.

[3] S. M. Dickerson, et al. Multiaxis Inertial Sensing with Long-Time Point Source Atom Interferometry. *Physical Review Letters*, 111(8):083001, aug 2013.

[4] F. Sorrentino, et al. Sensitivity limits of a Raman atom interferometer as a gravity gradiometer. *Physical Review A*, 89(2):023607, feb 2014.

[5] J. Le Gouët, et al. Limits to the sensitivity of a low noise compact atomic gravimeter. *Applied Physics B*, 92(2):133–144, aug 2008.

[6] Q. Bodart, et al. A cold atom pyramidal gravimeter with a single laser beam. *Applied Physics Letters*, 96(13):3–5, apr 2010.

[7] Y. Bidel, et al. Compact cold atom gravimeter for field applications. *Applied Physics Letters*, 102(14):2–5, feb 2013.

[8] M. Hauth, et al. First gravity measurements using the mobile atom interferometer GAIN. *Applied Physics B*, 113(1):49–55, oct 2013.

[9] B. Wu, et al. The investigation of a μGal-level cold atom gravimeter for field applications. *Metrologia*, 51(5):452–458, oct 2014.

[10] T. Schuldt, et al. Design of a dual species atom interferometer for space. *Experimental Astronomy*, 39(2):167–206, jun 2015.

[11] V. Schkolnik, et al. A compact and robust diode laser system for atom interferometry on a sounding rocket. 2016.

[12] R. von Eötvös. Mathematische und naturwissenschaftliche berichte aus ungarn. The presentation held at the Hungarian Academy of Sciences, 1890.

[13] Scintrex. CG-5 Autograv Gravity Meter.

[14] H. Virtanen. *Studies of Earth Dynamics with the Superconducting Gravimeter*. PhD thesis, 2006.

[15] Micro-g LaCoste. FG-5 gravity meter.

[16] C. Stummer. *Analyse der Gradiometergleichungen der GOCE Satellitenmission zur Schwerefeldbestimmung*. PhD thesis, 2006.

[17] A. Sugarbaker. *Atom Interferometry in a 10 m Fountain*. PhD thesis, 2014.

[18] J. Williams, et al. Quantum Test of the Equivalence Principle and Space-Time aboard the International Space Station. pages 1–34, oct 2015.

[19] J. M. Lumley, et al. A Superconducting Gravity Gradiometer Tool for Exploration. 2010.

[20] X. Wu. *Gravity Gradient Survey With A Mobile Atom Interferometer*. PhD thesis, 2009.

[21] S. Fray and M. Weitz. Atom-Based Test of the Equivalence Principle. *Space Science Reviews*, 148(1-4):225–232, dec 2009.

[22] A. Bonnin, et al. Simultaneous dual-species matter-wave accelerometer. *Phys. Rev. A*, 88:043615, Oct 2013.

[23] D. Schlippert, et al. Ground Tests of Einstein's Equivalence Principle: From Lab-based to 10-m Atomic Fountains. jul 2015.

[24] N. V. Gorban, et al. Leray-Hopf and Continuity Properties for All Weak Solutions for the 3D˜Navier-Stokes Equations. 94305, jan 2015.

[25] S. Chiow, et al. Laser-ranging long-baseline differential atom interferometers for space. *Physical Review A*, 92(6):063613, dec 2015.

[26] R. Geiger, et al. Matter-wave laser Interferometric Gravitation Antenna (MIGA): New perspectives for fundamental physics and geosciences. may 2015.

[27] B. Canuel, et al. MIGA: Combining laser and matter wave interferometry for mass distribution monitoring and advanced geodesy. pages 15–21, 2016.

[28] B. P. Abbott, et al. Observation of gravitational waves from a binary black hole merger. *Physical Review Letters*, 116(6):1–16, 2016.

[29] G. Rosi, et al. Precision measurement of the Newtonian gravitational constant using cold atoms. *Nature*, 510(7506):518–21, 2014.

[30] Rym Bouchendira, et al. New Determination of the Fine Structure Constant and Test of the Quantum Electrodynamics. *Physical Review Letters*, 106(8):080801, feb 2011.

[31] A. Gauguet, et al. Characterization and limits of a cold-atom Sagnac interferometer. *Physical Review A - Atomic, Molecular, and Optical Physics*, 80(6):1–12, 2009.

[32] A. Sugarbaker, et al. Enhanced Atom Interferometer Readout through the Application of Phase Shear. *Physical Review Letters*, 111(11):113002, sep 2013.

[33] W. D. Phillips. Laser cooling and trapping of neutral atoms. 70(3):721–741, 1998.

[34] J. Dalibard and C. Cohen-Tannoudji. Laser cooling below the Doppler limit by polarization gradients: simple theoretical models. *Journal of the Optical Society of America B*, 6(11):2023, nov 1989.

[35] K. P. Zetie, et al. How does a Mach-Zehnder interferometer work? *Physics Education*, 35(1):46–48, jan 2000.

[36] L. Allen and J. H. Eberly. *Optical Resonance and Two-Level Atoms*. Dover Publications Inc., 2003.

[37] H. J. Metcalf and P. van der Straten. *Laser Cooling and Trapping*. Springer, 2013.

[38] G. Lamporesi. *Determination of the Gravitational Constant by Atom Interferometry*. PhD thesis, Università Degli Studi Di Firenze, 2006.

[39] B. T. Draine and P. J. Flatau. Discrete-Dipole Approximation For Scattering Calculations. *Journal of the Optical Society of America A*, 11(4):1491, apr 1994.

[40] P. Meystre and M. Sargent. *Elements of Quantum Optics*. Springer, 2007.

[41] C.J. Foot. *Atomic Physics*. OUP Oxford, 2004.

[42] M. A. Kasevich. *Atom Interferometry in an Atomic Fountain*. PhD thesis, Stanford, 1992.

[43] M. Schmidt. *A mobile high-precision gravimeter based on atom interferometry*. PhD thesis, 2011.

[44] R. Wynands and S. Weyers. Atomic fountain clocks. *Metrologia*, 42(3):S64–S79, jun 2005.

[45] K. Moler, et al. Theoretical analysis of velocity-selective Raman transitions. *Physical Review A*, 45(1):342–348, 1992.

[46] M. A. Kasevich and S. Chu. Atomic Interferometry Using Stimulated Raman Transitions. *Physical Review Letters*, 67(2):181–184, 1991.

[47] D. S. Weiss, et al. Precision measurement of ?/m Cs based on photon recoil using laser-cooled atoms and atomic interferometry. *Applied Physics B Lasers and Optics*, 59(3):217–256, sep 1994.

[48] N. F. Ramsey. A Molecular Beam Resonance Method with Separated Oscillating Fields. *Physical Review*, 78(6):695–699, jun 1950.

[49] A. Clairon, et al. Ramsey Resonance in a Zacharias Fountain. *Europhysics Letters (EPL)*, 16(2):165–170, sep 1991.

[50] A. Wicht, et al. A Preliminary Measurement of the Fine Structure Constant Based on Atom Interferometry. *Physica Scripta*, T102(1):82, 2002.

[51] P. Storey and C. Cohen-Tannoudji. The Feynman path integral approach to atomic interferometry. *J. Phys. II France*, 4:1999–2027, 1994.

[52] P. Cheinet, et al. Measurement of the Sensitivity Function in a Time-Domain Atomic Interferometer. *IEEE Transactions on Instrumentation and Measurement*, 57(6):1141–1148, jun 2008.

[53] V. Schkolnik, et al. The effect of wavefront aberrations in atom interferometry. *Applied Physics B*, 120(2):311–316, aug 2015.

[54] R. G. Lane and M. Tallon. Wave-front reconstruction using a ShackHartmann sensor. *Applied Optics*, 31(32):6902, nov 1992.

[55] C. Cohen-Tannoudji. Interférométrie atomique. Leçons du Collège de France, 1992.

[56] M. Hauth, et al. *Atom Interferometry for Absolute Measurements of Local Gravity.* 2014.

[57] C. Champenois, et al. Matter neutrality test using a mach-zehnder interferometer. In SavelyG. Karshenboim, et al., editors, *The Hydrogen Atom*, volume 570 of *Lecture Notes in Physics*, pages 554–563. Springer Berlin Heidelberg, 2001.

[58] S. Dickerson, et al. A high-performance magnetic shield with large length-to-diameter ratio. *The Review of scientific instruments*, 83(6):065108, jun 2012.

[59] S. Malkowski, et al. Technique for high axial shielding factor performance of large-scale, thin, open-ended, cylindrical Metglas magnetic shields. *Review of Scientific Instruments*, 82(7):075104, jul 2011.

[60] W. M. Itano, et al. Quantum projection noise: Population fluctuations in two-level systems. *Physical Review A*, 47(5):3554–3570, may 1993.

[61] J. M. McGuirk, et al. Sensitive absolute-gravity gradiometry using atom interferometry. *Physical Review A*, 65(3):033608, feb 2002.

[62] C. Freier, et al. Mobile quantum gravity sensor with unprecedented stability. dec 2015.

[63] G. C. Bjorklund, et al. Frequency modulation (FM) spectroscopy - Theory of lineshapes and signal-to-noise analysis. *Applied Physics B Photophysics and Laser Chemistry*, 32:145–152, 1983.

[64] J. Schoser, et al. Intense source of cold Rb atoms from a pure two-dimensional magneto-optical trap. *Physical Review A*, 66(2):023410, aug 2002.

[65] J. R. Kellogg, et al. A compact high-efficiency cold atom beam source. *Applied Physics B*, 109(1):61–64, oct 2012.

[66] Jaime Ramirez-Serrano, et al. Multistage two-dimensional magneto-optical trap as a compact cold atom beam source. *Optics letters*, 31(6):682–4, mar 2006.

[67] T. Petelski. *Atom Interferometers for Precision Gravity Measurements*. PhD thesis, 2005.

[68] A. Dunning, et al. Composite pulses for interferometry in a thermal cold atom cloud. pages 1–10, jun 2014.

[69] K. Bongs, et al. isense: A technology platform for cold atom based quantum technologies. In *Research in Optical Sciences*, page QTu3B.1. Optical Society of America, 2014.

[70] G. W. Biedermann, et al. Low-noise simultaneous fluorescence detection of two atomic states. *Optics letters*, 34(3):347–9, feb 2009.

[71] J. M. McGuirk, et al. Low-noise detection of ultracold atoms. *Optics letters*, 26(6):364–6, mar 2001.

[72] M. Baumert. *Dipole traps and optical lattices for quantum simulations*. PhD thesis, 2013.

[73] A. Lukindo. LabVIEW Queued State Machine Architecture. Web Article - https://decibel.ni.com/content/docs/DOC-32964, 2007.

[74] D.-S. Lü, et al. Improvement on Temperature Measurement of Cold Atoms in a Rubidium Fountain. *Chinese Physics Letters*, 28(6):063201, jun 2011.

[75] D. A. Steck. Rubidium 87 D Line Data. pages 1–29, 2003.

[76] J. Dalibard and C. Cohen-Tannoudji. Laser cooling below the Doppler limit by polarization gradients: simple theoretical models. *Journal of the Optical Society of America B*, 6(11):2023, nov 1989.

[77] Z. Ji, et al. Optimization and analysis of experimental parameters for polarization gradient cooling in optical molasses. page 10, apr 2013.

[78] C. G. Townsend, et al. High-density trapping of cesium atoms in a dark magneto-optical trap. *Physical Review A*, 53(3):1702–1714, mar 1996.

[79] L.-S. Yang, et al. Loading and Compression of a Large Number of Rubidium Atoms Using a\rSemi-Dark Type Magneto-Optical Trap. *Chinese Journal of Physics*, 45(November):606–615, 2007.

[80] T. Farah, et al. Effective velocity distribution in an atom gravimeter: effect of the convolution with the response of the detection. jun 2014.

[81] P. Berthoud, et al. Bright, slow, and continuous beam of laser-cooled cesium atoms. *Physical Review A*, 60(6):R4241–R4244, dec 1999.

[82] M. S. Dresselhaus, et al. Raman spectroscopy on isolated single wall carbon nanotubes. *Carbon*, 40(12):2043–2061, 2002.

[83] O. Sezerman and G. Best. Accurate alignment preserves polarization. *Laser Focus World*, (December):1–3, 1997.

[84] J. Kushibiki, et al. Accurate measurements of the acoustical physical constants of LiNbO (3) and LiTaO(3) single crystals. *IEEE transactions on ultrasonics, ferroelectrics, and frequency control*, 46(5):1315–23, 1999.

[85] D. Akamatsu, et al. A compact light source at 461 nm using a periodically poled linbo3 waveguide for strontium magneto-optical trapping. *Opt. Express*, 19(3):2046–2051, Jan 2011.

[86] S. S. Sané, et al. 11 W narrow linewidth laser source at 780 nm for laser cooling and manipulation of Rubidium. *Optics express*, 20(8):8915–9, apr 2012.

[87] S. Chiow, et al. Generation of 43 W of quasi-continuous 780 nm laser light via high-efficiency, single-pass frequency doubling in periodically poled lithium niobate crystals. *Optics letters*, 37(18):3861–3, sep 2012.

[88] E. D. Black. An introduction to PoundDreverHall laser frequency stabilization. *American Journal of Physics*, 69(January 2000):79, 2001.

[89] D. F. Eaton. Nonlinear Optical Materials. *Science*, 253:281–287, 1991.

[90] D. S. Hum and M. M. Fejer. Quasi-phasematching. *Comptes Rendus Physique*, 8(2):180–198, mar 2007.

[91] S. Ozharar, et al. Ultra-high spur-free dynamic range RF synthesis using optical homodyne serrodyne technique. 43(5):5–6, 2007.

[92] R. Kohlhaas, et al. Robust laser frequency stabilization by serrodyne modulation. *Optics Letters*, 37(6):1005, mar 2012.

[93] D. M. S. Johnson, et al. Broadband Optical Serrodyne Frequency Shifting. pages 1–3, sep 2009.

[94] R. Houtz, et al. Wideband, efficient optical serrodyne frequency shifting with a phase modulator and a nonlinear transmission Line. *Optics Express*, 17(21):19235, oct 2009.

[95] M. Case. *Nonlinear Transmission Lines for Picosecond Pulse, Impulse and Millimeter-Wave Harmonic Generation*. PhD thesis, University of California, 1993.

[96] O. Carraz, et al. Compact and robust laser system for onboard atom interferometry. *Applied Physics B*, 97(2):405–411, oct 2009.

[97] D. Jedrzejczyk, et al. Efficient high-power frequency doubling of distributed Bragg reflector tapered laser radiation in a periodically poled MgO-doped lithium niobate planar waveguide. *Optics Letters*, 36(3):367, feb 2011.

[98] J. Sun and C. Xu. 466 mW green light generation using annealed proton-exchanged periodically poled MgO: LiNbO_3 ridge waveguides. *Optics Letters*, 37(11):2028, jun 2012.

[99] N. Chiodo, et al. CW frequency doubling of 1029nm radiation using single pass bulk and waveguide PPLN crystals. *Optics Communications*, 311:239–244, jan 2013.

[100] S. Peil, et al. High-efficiency frequency doubling for the production of 780 nm light. In *IEEE International Frequency Control Symposium and PDA Exhibition Jointly with the 17th European Frequency and Time Forum*, pages 159–161, 2003.

[101] D. J. McCarron, et al. Modulation transfer spectroscopy in atomic rubidium. *Measurement Science and Technology*, 19(10):105601, oct 2008.

[102] A. Niggebaum. *Towards mobile quantum sensors for gravity surveys.* PhD thesis, University of Birmingham, 2015.

[103] B. E. King. Angular Momentum Coupling and Rabi Frequencies for Simple Atomic Transitions. *arXiv*, apr 2008.

[104] M. J. Pritchard. *Manipulation of ultracold atoms using magnetic and optical fields Manipulation of ultracold atoms using magnetic and optical fields*. PhD thesis, 2006.